

Characterization of liquid spray impact onto walls and films

Vom Fachbereich Maschinenbau
An der Technischen Universität Darmstadt
Zur
Erlangung des Grades eines Doktor-Ingenieurs (Dr.-Ing.)
genehmigte

Dissertation

Vorgelegt von

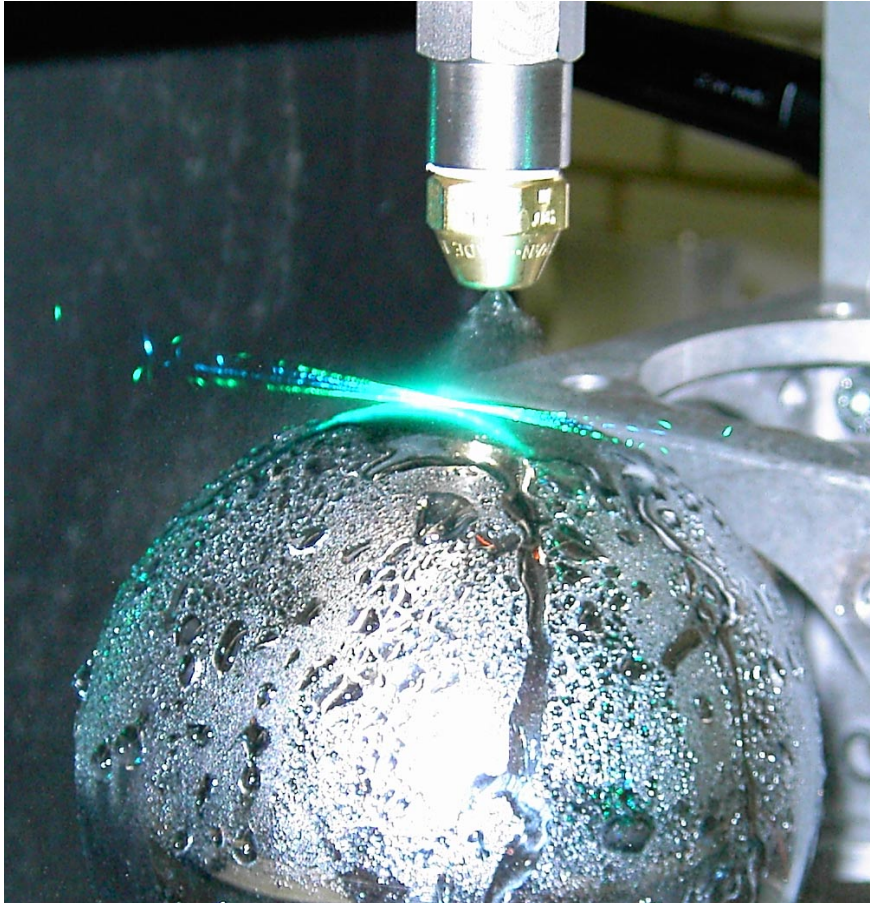
Dipl.-Ing. Davood Kalantari (M.Sc.)

Aus Ardebil, Iran

Berichterstatter:	Prof. Dr.-Ing. C. Tropea
Mitberichterstatter:	Prof. Dr.-Ing. M. Marengo Dr.-Ing.-habil. I.V. Roisman
Tag der Einreichung:	01.08.2006
Tag der mündlichen Prüfung:	21.11.2006

Darmstadt 2006
D 17

II



Liquid spray impact onto a solid sphere

Publications resulting from this dissertation

Chapter 2

D. Kalantari, C. Tropea, (2006). Considerations in Phase Doppler measurements of spray-wall interaction. 13th Int. Symp. Applications of Laser techniques to Fluid Mechanics. Jun. 26-29, Lisbon, Portugal. Accepted for publication in Exp. In Fluids.

Chapter 3

D. Kalantari, C. Tropea, (2006). Spray impact onto rigid walls: Empirical characterization and modelling. I.J. Multiphase Flow, In press.

Chapter 4

D. Kalantari, C. Tropea, (2006). Spray impact onto rigid walls: Formation of the liquid film. ICLASS06, Aug.27-Sep.01, 2006, Kyoto, Japan.

Chapter 5

D. Kalantari, C. Tropea, (2006). Comparison splash of a droplet in isolation and in a spray. Workshop spray2006, Mai. 29-30, Lampoldshausen, Germany.

Chapter 6

D. Kalantari, C. Tropea, (2006). Oblique spray impingement onto rigid walls: Description of secondary spray. 14th Int. Mech. Eng. Conference, May.16-18, Isfahan, Iran.

Chapter 7

D. Kalantari, I.V. Roisman and C. Tropea, (2006). Spray impact onto deep liquid layers: deformation of air-liquid film interface, secondary spray and air bubble entrainment. ICLASS06, Aug.27-Sep.01, 2006, Kyoto, Japan.

Further publications (during my study in FG-SLA: TU-Darmstadt)

1-Journal Papers:

- 1- **D. Kalantari**, C. Tropea, (2005). Considerations for high resolution Laser Doppler measurements in very small circular tubes. *J. Meas. Sci. and Tech.* Vol.16, No. 24, 2344-2350.
- 2- **D. Kalantari**, C. Tropea, (2006). Phase Doppler measurements of spray/wall interaction. *Exp. In Fluids*, Submitted.
- 3- **D. Kalantari**, A. Fedorchenko, P.-F. Sung, A.-B. Wang, and C. Tropea, (2006). Dynamics of high viscous liquid droplet spreading on rigid-flat surfaces, *Euro Phys. Lett.*, submitted.
- 4- **D. Kalantari**, C. Tropea, (2006). Liquid droplet impact onto flat and rigid surfaces: Initial lamella ejecting velocity, *Euro Phys. Lett.*, submitted.

2-Conference Papers:

- 5- **D. Kalantari**, C. Tropea, (2005). Experimental study of spray impact onto rigid walls. 20th ILASS Conference. 5-7Sep.Orleans, France.
- 6- N. Damaschke, **D. Kalantari**, I.V. Roisman and C. Tropea, (2005). Characterization of spray transport and spray/wall interactions using the IPI technique. 20th ILASS Conference. 5-7Sep.Orleans,France.
- 7- **D. Kalantari**, C. Tropea, (2005). Considerations for high resolution laser Doppler measurements in very small nozzles. 8th Int. Conf. Optical Methods of Flow Investigation. 28 June-1July 2005, Moscow, 88-91.
- 8- N. Damaschke, **D. Kalantari**, I.V. Roisman and C. Tropea, (2005). Charactrization of spatial drop distribution in a spray using the IPI technique. 8th Int.Con. Optical Methods of Flow Investigation. 28 June-1July 2005, Moscow, 8-11.

Acknowledgements

First of all, I would like to thank the Prof. Dr.-Ing. Habil. Cameron Tropea, Chair of the Fluid Mechanics and Aerodynamics (FG- SLA) for his supervision of my research work during my Ph.D. study in Technical University of Darmstadt. Clearly without his extensive helps and guides during my research period, I couldn't reach the goals of the present work.

I would like to thank all of my colloquies and friends in our institute, especially Dr.-Ing. N. Damaschke, Prof. Dr.-Ing. K.G. Roesner, Dr.-Ing. K. Heukelbach, Dr. G. Castanet, Dr. I.V. Roisman, Dip.-Ing. H.-J. Schroeder, Dip.-Ing. O. Kyriopoulos, Dip.-Ing. M. Gnirß and M. Kron for their helps and useful discussions during my research work in FG-SLA.

I also would like to thank Mrs. S. Lath, Mr. D. Sachs and Mrs. S. Walner, secretary of our institute for their extensive helps during my stay in Germany.

I would like to thank Ministry of Science, Research and Technology of Iran and University of Mazandaran (UMZ) for financial support during my stay in Germany through the scholarship Nr. 780274.

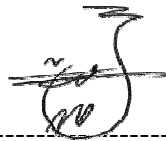
My best thank goes to my wife, Mrs. Masoumeh Chahartaghi-Abnieh for her consistent support during the last years and also my father for his suggestions and financial support during my last education in Iran.

Erklärung

Hiermit erkläre ich, dass ich die vorliegende Arbeit, abgesehen von den in ihr ausdrücklich genannten Hilfen, selbständig verfasst habe.

01.08.06

Datum

A handwritten signature in black ink, consisting of a stylized, cursive script. The signature is written over a horizontal dashed line.

Unterschrift

Characterization of liquid spray impact onto walls and films

Abstract

The present work is concerned with the characterization of liquid spray impact onto walls and films. Empirical studies on spray impact rely almost solely on the phase Doppler instrument for obtaining quantitative data about drop size and velocity distributions. The thesis begins therefore with a careful examination of applying the phase Doppler instrument to new-wall measurements beneath a spray. This includes consideration of the influence of the measurement volume height above the rigid wall, the input laser power and the spatial location of the detection volume on the measured characteristics of the impinging and secondary spray. This knowledge is then used for all subsequent measurements made within the framework of this investigation. After a qualitative and quantitative characterization of the resulting secondary spray and the accumulated wall film, a set of empirical models is presented for prediction of the characteristics of the secondary spray generated due to a liquid spray impact onto a rigid wall. In the models, characterization of the secondary spray has been formulated in terms of correlations for the velocity and trajectory of secondary droplets and the mass and number ratio of the secondary spray. The novel aspect of the model is that the correlations are based on the mean statistics over many events in the spray and not on the outcome of single drop impact experiments. Another interesting feature of the experiments is the rather large range of oblique impact angles captured, due to the different drop trajectories exiting from the spray. A phase Doppler instrument has been used to measure drop size and two components of velocity directly above the target. A high-speed CCD camera has been used to measure the average film thickness formed due to spray impact.

In a second step, a theoretical model to predict the average film thickness formed due to a liquid spray impinging onto a flat and rigid wall is presented. This model takes into account the characteristics of the impinging spray, e.g. flux density of impacting droplets,

hydrodynamic pressure of the impinging spray and viscosity of the impacting liquid droplets. It considers the mass and momentum balance of the film, including viscosity effect and neglecting the Laplace pressure. A second simplified model for predicting the average film thickness as a function of mean Reynolds number and flux density of the impacting droplets and the average drop diameter is presented based on dimensional analysis. Both theoretical derivations for the average film thickness show good agreement with most of the measurements.

This thesis also provides an experimental comparison of the splashing phenomenon for single drops and for drops in a spray, followed by a derived theoretical model. Such a comparison can be very valuable for future modelling of spray impact.

The last section of this thesis presents an experimental study for different aspects of liquid spray impact onto a deep liquid layer under well controlled experimental conditions; deformation of the air-liquid film interface due to the hydrodynamic pressure exerted by the impacting drops, the generation of a secondary spray, and the air bubble entrainment into the liquid film. A high-speed CCD camera has been used to measure the deformation of the air-liquid film interface and the distribution of the air bubbles inside the deep liquid film. Two different configurations of a phase Doppler instrument have been used to measure drop size and two components of velocity directly above the film as well as the size and two components of velocity of the air bubbles inside the deep pool.

Charakterisierung der flüssigen Sprayauswirkung auf unterschiedliche Wände und Filme

Zusammenfassung

Die vorliegende Arbeit befasst sich mit der Charakterisierung des Aufpralls eines flüssigen Sprays auf unterschiedliche Wände und Filme. Nachdem zunächst eine qualitative und quantitative Charakterisierung des Sekundärsprays und entstehenden Wandfilme vorgestellt wurde, wird anschließend ein Satz empirischer Modelle zur Vorhersage der Eigenschaften des Sekundärsprays, erzeugt durch einen Sprayaufprall auf eine starre Wand, dargestellt. In diesem Modell ist die Charakterisierung des Sekundärsprays als Wechselbeziehung von Geschwindigkeit und Flugbahn der Sekundärtröpfchen, sowie deren Massen- und Zahlenverhältnis ausgedrückt. Der neuartige Aspekt des Modells liegt darin, dass die Korrelationen auf durchschnittlichen statistischen Größen über mehrere Ereignisse im Spray gemittelt, und nicht auf dem Resultat Einzeltropfenaufprallexperimente basieren. Eine andere interessante Eigenschaft der Experimente ist der große Bereich der Aufprallwinkel, die berücksichtigt werden konnten. Zur Messung der Tropfengröße und zweier Geschwindigkeitskomponenten wurde ein Phasen-Doppler Gerät benutzt. Um die durch Sprayaufprall entstandenen durchschnittlichen Filmdicken zu messen, kam eine Hochgeschwindigkeitkamera zum Einsatz.

In einem zweiten Schritt wird ein theoretisches Modell zur Vorhersage der durchschnittlichen Filmdicken vorgestellt. Das Modell basiert auf der Hydrodynamik eines sich ausbreitendem dünnen Flüssigkeitsfilms auf einer starren Wand. Dabei nimmt das Modell die Eigenschaften des Spray-Aufpralls in Betracht, wie beispielsweise Flussdichte und Viskosität der aufprallenden Tröpfchen und den dynamischen Druck des Sprays. Ein weiteres vereinfachtes Modell zur Vorhersage der durchschnittlichen Filmdicken als Funktion der mittleren Reynolds-Zahl, der Flussdichte der aufprallenden Tröpfchen und des durchschnittlichen Tropfendurchmessers wird basierend auf der Dimensionsanalyse

dargestellt. Beide theoretischen Ableitungen für die durchschnittliche Filmdicke zeigen eine gute Übereinstimmung mit den Messungen.

Weiterhin schafft diese Arbeit einen grundlegenden Vergleich zwischen dem Aufprall für einzelne Tropfen und dem Aufprall für Tropfen in einem Spray, gefolgt von einem abgeleiteten theoretischen Modell. Ein solcher Vergleich kann für das zukünftige Modellieren des Sprayaufpralls sehr wertvoll sein.

Ein weiterer Teil dieser Arbeit stellt eine experimentelle Untersuchung des Sprayaufpralls auf eine tiefe Flüssigkeit dar, in dem Deformation der Luft-Flüssigkeit-Grenzfläche aufgrund des dynamischen Drucks durch aufprallende Tropfen, die Erzeugung eines Sekundärsprays und die Entstehung von Blasen durch den Einschluss von Luft in der Flüssigkeit behandelt wird. Um die Deformation der Luft-Flüssigkeit-Grenzfläche und die Verteilung der Luftblasen innerhalb der Flüssigkeit zu messen, wurde eine Hochgeschwindigkeits-CCD Kamera benutzt. Zwei unterschiedliche Konfigurationen eines Phasen-Doppler-Gerätes wurden verwendet, um einerseits Tropfendurchmesser und zwei Geschwindigkeitskomponenten direkt über dem Film sowie andererseits Durchmesser und zwei Geschwindigkeitskomponenten der Luftblasen innerhalb der Flüssigkeit zu messen. Abschließend werden einige Überlegungen für die Phasen-Doppler-Messungen des Sprayaufpralls auf eine starre Wand im Detail präsentiert. Dieser Teil der Arbeit liefert experimentellen Ergebnisse, die den Einfluss der Messvolumenhöhe über der Wand, und den Einfluss der eingehenden Laser-Leistung auf die Messergebnisse der Eigenschaften des Sekundärsprays beschreiben, als auch Überlegungen zur Positionen des aufprallenden Sprays und des Sekundärsprays.

Contents

1. Introduction	1
1.1. Goals and contribution of the present approach	3
1.2. Thesis Outline.....	4
2. Phase Doppler Measurements of Spray/Wall Interaction	7
2.1. Introduction	7
2.2. Computation of statistical quantities	9
2.2.1. Determination of efficient detection volume size.....	9
2.2.2. Computation of statistical quantities in spray.....	14
2.3. Summary of computed procedure	17
2.4. Experimental set-up.....	17
2.5. Results and discussion.....	19
2.6. Conclusion.....	25
3. Spray impact onto flat and rigid walls: Empirical characterization and modeling	27
3.1. Introduction	27
3.2. Experimental Set-up	37
3.2.1. Number of required samples at each grid point for a statistically reliable measurement.....	40
3.2.2. Effect of target position	41
3.3. Results and discussion.....	42
3.3.1. Distribution of droplet size	44
3.3.2. Distribution of velocity.....	46
3.3.3. Trajectory of secondary droplets (ejection angle of secondary droplets).....	48
3.3.4. Distribution of the ejection Weber number	50
3.3.5. Distribution of secondary to incident mass and number ratios	52

3.3.6. Average film thickness	60
3.4. Conclusions	63
4. Spray impact onto flat and rigid walls: Formation of the liquid film	67
4.1. Introduction	67
4.2. Experimental set-up	69
4.3. Formation of the wall liquid film	70
4.3.1. Hydrodynamic pressure source in the wall liquid film	72
4.3.2. Influence of the gravity in the wall liquid film.....	75
4.3.3. Mass source term of the wall liquid film (Γ_m)	76
4.4. Asymptotic solution for the wall film thickness.....	77
4.4.1. Film flow in low-Reynolds regime.....	77
4.4.2. Scaling for the film thickness in the high-Reynolds regime	80
4.5. Results and discussion	83
4.6. Discussion.....	88
5. Comparison between splash of a droplet in isolation and in a spray	91
5.1. Introduction	91
5.2. Experimental set-up	93
5.3. Results and discussion	93
5.3.1. Splashing droplet in isolation	94
5.3.2. Splashing droplet in a spray.....	101
5.4. Conclusion.....	104
6. Oblique spray impingement onto rigid walls: Description of secondary spray	105
6.1. Introduction	105
6.2. Experimental Set-up	107
6.3. Result and discussion	109
6.3.1. Distribution of droplet size.....	109
6.3.2. Distribution of velocity.....	110
6.3.3. Trajectory of the secondary droplets (ejection angle of the secondary droplets).....	112
6.3.4. Distribution of after impact Weber number	113

6.3.5. Distribution of secondary to incident mass and number ratios	114
6.4. Conclusions	116
7. Spray impact onto deep liquid layers: deformation of air-liquid interface, secondary spray and air bubble entrainment	117
7.1. Introduction	117
7.2. Experimental set-up	118
7.3. Results and discussion	120
7.3.1. Deformation of air-liquid film interface under spray impact	120
7.3.2. Formation of the secondary spray due to spray impact onto deep liquid layers	124
7.3.3. Air bubble entrainments due to spray impact onto deep liquid layers .	125
7.4. Conclusions	135
8. Conclusion and Outlooks	137
8.1. Conclusion and main achievements	137
8.2. Outlook and useful suggestions for future works	138
I. Summary of previous models for single drop and spray impact	141
I.1. Velocity of the ejected (secondary) droplets	141
I.2. Ejection angle of the secondary splashing droplets	143
I.3. Total splashing-to-incident mass and number ratio ($\lambda_m = m_a/m_b$, $\lambda_N = N_a/N_b$)	144

Figure Captions:

Fig. 2-1: Linear assumption for distribution of the laser light on small particles in compare to the measurement volume size.....	10
Fig. 2-2: a) Sketch for statistically distribution of the burst lengths inside the detection volume and droplet trajectory, and b) mathematical element (dz) of detection volume to be integrated yielding the mean burst length.	12
Fig. 2-3: Effective measurement volume diameter for number count >50 ,	13
Fig. 2-4: Effective measurement cross sectional area in two directions.	15
Fig. 2-5: Photograph of experimental set-up used in this study.	18
Fig. 2-6: Sketch for: a) positioning the measurement volume precisely at the target centreline, and b) zero-position of the measurement volume height.....	19
Fig. 2-7: Mean velocity a) before the impact and b) after the impact, as a function of measurement volume height above the rigid wall. The different lines represent different laser power.....	20
Fig. 2-8: Average droplet size before impact a) as a function of measurement volume height above the rigid wall (the different lines represent different laser power), and b) as a function of input laser power.	22
Fig. 2-9: Average droplet size after impact as a function of measurement volume height above the rigid wall (the different lines represent different laser power).	22
Fig. 2-10: Maximum non-dimensional crown height as a function of Weber number before the impact in spray and in isolation.	22
Fig. 2-11: Total secondary-to-incident a) mass and b) number ratios in spray impact onto a rigid wall. The different lines represent different laser power.	23
Fig. 2-12: Sketch for impinging and ejecting droplets passing through the detection volume.	24
Fig. 2-13: Influence of correction for spatial position of the a) impinging droplet and b) secondary droplet.....	25
Fig. 3-1: Morphological comparison between splashes created by: a) an isolated single drop at various impact conditions, and b) by drops in a spray.	29
Fig. 3-2: Sketch of a non-symmetric splashing droplet in spray due to neighbourhood droplet(s) impact.....	30
Fig. 3-3: Image sequence of a splashing droplet in a spray recorded with 16 kfps; $We_{nb} = 534$ and $\bar{h}/d_b = 0.57$	31
Fig. 3-4: Instantaneous variation of: a) crown radius and b) crown height with dimensionless time ($t^* = t \cdot u_b / d_b$); $We_{nb} = 534$ and $\bar{h}/d_b = 0.57$	32
Fig. 3-5: Different sources for generation of secondary droplets and formation of liquid film on the wall, secondary droplet ejected from: (a) splashing droplet; (b) ejected wall film; (c) rebounded droplet.	33
Fig. 3-6: Exemplary sequence of a rebound in a spray impact phenomenon; $d_b \cong d_a = 172\mu\text{m}$, $We_{nb} = 10$, time interval between frames is 0.55 ms.	34

Fig. 3-7: Photograph of the experimental set-up for spray impact studies (Showing the CCD camera and the phase Doppler measurement system).	38
Fig. 3-8: Coordinate system and nomenclature for impinging and ejecting droplets.....	38
Fig. 3-9: a) Mean roughness (R_a or $\bar{\varepsilon}$), and b) mean peak-to-valley roughness (R_z) of the target surface.....	40
Fig. 3-10: Two exemplary single-point measurements of primary droplet count with and without target at 20mm under nozzle exit: (a) on the spray axis: $z=0$, and (b) off-axis: $z=15$ mm, measured 1 mm above the target.....	42
Fig. 3-11: Number density distribution of primary and secondary droplet sizes for four measurement points, measured 1 mm above the wall ($x = -1$); solid line: before impact, dashed line: after impact.....	44
Fig. 3-12: a) Correlation between mean drop size before and after impact, and b) correlation for drop size ratio normal impact Weber number.....	46
Fig. 3-13: Comparison of droplet velocity before and after impact for various positions of the measurement volume above the $D=15$ mm target: (a) normal component, and (b) tangential component; average film thickness $\bar{h} \approx 20$ μm	47
Fig. 3-14: Mean velocity ratio of ejected to impinging droplets as a function of impact Weber number: a) normal component, b) tangential component, and c) tangential component of after against before impact velocity.	48
Fig. 3-15: a) Correlation between mean ejection angle and impingement angle of droplets, collected over all experiments; b) Impingement (θ_b) and ejection (θ_a) angle of droplets at a single measurement point and as a function of droplet diameter.	49
Fig. 3-16: Coefficient of ejection angle of secondary droplets.	49
Fig. 3-17: Weber number of ejected droplets against impact Weber number.....	50
Fig. 3-18: Distribution of: a) impact, and b) ejection Weber numbers at a single measurement point above a spherical target.....	51
Fig. 3-19: Exemplary variation of the droplet velocity and droplet size for before impact ($u>0$) and after impact ($u<0$).	51
Fig. 3-20: Variation of number and Weber number ratio across the target: a) number ratio (λ_N) and Weber number based on the normal velocity component before impact (We_{nb}), and b) number ratio (λ_N) and Weber number ratio $\lambda_{We_b} = We_{ib}/We_{nb}$	54
Fig. 3-21: Distribution of secondary-to-incident mass ratio (λ_m) for: (a) normal impact condition $\lambda_{We_b} < 0.1$, and (b) oblique impact condition $\lambda_{We_b} \geq 0.1$	55
Fig. 3-22: Correlation of secondary-to-incident: a) mass ratio λ_m , and b) number ratio λ_N with impact Weber number based on the normal component of velocity We_{nb} for normal impact conditions $\lambda_{We_b} < 0.1$	56
Fig. 3-23: a) Correlation of secondary-to-incident: mass ratio λ_m and number ratio λ_N , and b) with impact Weber number based on the normal component of velocity We_{nb} for oblique impact condition $\lambda_{We_b} > 0.1$	58
Fig. 3-24: Sketch for the normal impact region (a, and b), and oblique impact region (c). .	59

Fig. 3-25: Thin liquid film formed under spray impact: a) original image of CCD camera with interface contour added, and b) synthesized image to be integrated yielding the average film thickness.	60
Fig. 3-26: Sketch for the accumulated wall liquid film to be integrated yielding the average film thickness.....	60
Fig. 3-27: An exemplary variation of the standard deviation σ (h) as a function of the measured average film thickness.....	61
Fig. 3-28: Variation of the average film thickness: a) with the nozzle pressure at different nozzle height, and b) with the Reynolds number, for a stainless steel target with diameter of 5mm ($D = 5mm$).	62
Fig. 3-29: Variation of the impact Weber number (We_{nb}), average film thickness (\bar{h}), mass ratio (λ_m) and flux density (\dot{q}) with the nozzle height (x) for two exemplary nozzle pressures: (a) 3 bar, and (b) 6 bar; for a stainless steel target with diameter of 5mm ($D = 5mm$).	63
Fig. 4-1: Impingement and outer region of thin liquid film formed under spray impact.	70
Fig. 4-2: Sample images of the liquid film interface formed under spray impact: a) relatively sparse spray, b) relatively dense spray.	72
Fig. 4-3: Total secondary-to-incident number ratio as a function of impact Weber number based on the normal velocity component.	75
Fig. 4-4: Total secondary-to-incident mass ratio as a function of impact Weber number based on the normal velocity component.	76
Fig. 4-5: a) Curvature of the liquid film-air interface, and b) Control volume (C.V.) for a spreading wall liquid film.....	79
Fig. 4-6: Variation of the dynamic pressure due to the impinging droplets in a spray.	80
Fig. 4-7: Formation of the average film thickness under a relatively sparse spray.....	81
Fig. 4-8: Frequency of the impinging droplets in a spray.	81
Fig. 4-9: Average dimensionless film thickness accumulated on the flat-rigid wall as a function of Reynolds number before the impact.	84
Fig. 4-10: Variation of the non-dimensional thickness of the spreading lamella as a function of impact Reynolds number at the instant of d_0/u_0 , Ref: Roisman et al., (2006).....	85
Fig. 4-11: Prediction of the dimensional analysis for the average film thickness.....	85
Fig. 4-12: Total secondary-to-incident: a) mass ratio (λ_m), and b) number ratio (λ_N).	86
Fig. 4-13: Influence of the average film thickness on the total secondary-to-incident mass ratio for different constant impact Weber numbers.....	88
Fig. 5-1: Sketch for structure of a splashing liquid droplet.....	94
Fig. 5-2: Sketch for structure of a splashing liquid droplet.....	97
Fig. 5-3: Determination of the instantaneous crown thickness at the instant of crown evaluation, Ref: Fedorchenko and Wang (2004a).....	98
Fig. 5-4: Crown thickness at the instant of the maximum crown height as a function of impact Weber number for various wall film thicknesses.	99
Fig. 5-5: Variation the non-dimensional radius of the crown rim as a function of non-dimensional crown upper radius, Ref. Range and Feuillebois (1998).....	99

Fig. 5-6: Maximum non-dimensional crown height as a function of impact velocity for two different non-dimensional film thicknesses, $d_0=3 \text{ mm}$.	100
Fig. 5-7: Influence of non-dimensional film thickness on the maximum non-dimensional crown height.	100
Fig. 5-8: Prediction of the maximum non-dimensional crown height as a function of the experimental measurements obtained by Cossali et al. (1997).	101
Fig. 5-9: Maximum non-dimensional crown height as a function of impact Weber number before the impact in spray.	103
Fig. 5-10: Maximum non-dimensional crown height estimated from Eq. (4.8) as a function of the experimental results.	103
Fig. 5-11: Exemplary experimental result of crown base radius and height for a splashing droplet in a spray.	104
Fig. 6-1: Exemplary different source of interactions in spray between: a) two droplets, b) two splashing droplets, c) an uprising jet with a droplet and d) a splashing droplet and other droplet.	107
Fig. 6-2: Sketch for: a) an oblique spray and b) a normal spray impinging onto a flat-rigid surface.	108
Fig. 6-3: Photograph of the experimental set-up for oblique spray impingement.	108
Fig. 6-4a: Coordinate and dimensions for oblique spray impingement used in this study.	109
Fig. 6-5: average secondary to impact droplet size ratio ($\lambda_{d10} = d_{10a} / d_{10b}$) as a function of injection angle (θ_i).	110
Fig. 6-6: average secondary to impact droplet size ratio ($\lambda_{d10} = d_{10a} / d_{10b}$) as a function of impact Weber number based on the normal component of impact velocity (We_{nb}).	110
Fig. 6-7: The ratio of normal component of velocity (u_a / u_b) as a function of measurement position above the target.	112
Fig. 6-8: The ratio of normal component of velocity (u_a / u_b) as a function of injection angle (θ_i).	112
Fig. 6-9: Tangential ejection velocity of secondary droplets (v_a) as a function of impact tangential velocity (v_b) for different injection angles.	112
Fig. 6-10: The ratio of tangential component of velocity (v_a / v_b) as a function of injection angle (θ_i).	112
Fig. 6-11: Ejection angle of secondary droplets (θ_a) as a function of impingement angle (θ_b).	113
Fig. 6-12: Ejection angle of secondary droplets (θ_a) as a function of injection angle (θ_i).	113
Fig. 6-13: Variation of impact Weber number with injection angle (θ_i).	114
Fig. 6-14: The ratio of ejection to impact Weber number (We_a / We_b) as a function of injection angle (θ_i).	114
Fig. 6-15: Total secondary to incident mass ratio ($\lambda_m = m_a / m_b$) as a function of injection angle (θ_i).	115

Fig. 6-16: Total secondary to incident mass ratio ($\lambda_m = m_a/m_b$) as a function of impact We number for different injection angles (θ_i).	115
Fig. 7-1: Photograph of experimental set-up used in this study.	119
Fig. 7-2: Coordinate system for the spray and deep pool.	120
Fig. 7-3: a) Exemplary deformation of the air-liquid film interface due to spray impact, and b) film interface for different nozzle pressure.	122
Fig. 7-4: Maximum depth of the air-liquid film interface deformation under spray impact.	123
Fig. 7-5: Maximum air-liquid film interface deformation as a function of hydrodynamic pressure exerted from impacting spray.	124
Fig. 7-6: Comparison of droplet velocity before and after impact, a) normal component, b) tangential component.	125
Fig. 7-7: Spray impact onto deep liquid film, a) illuminated by normal light, and b) illuminated by laser light.	125
Fig. 7-8: Close-up view of the variation the number of bubbles inside the deep liquid layer under spray impact for different nozzle pressure a) 3 bar, b) 4 bar, c) 5 bar, and d) 6 bar.	126
Fig. 7-9: Probability density of air bubbles diameter for different impact condition; $X_{nozzle} = -40$ mm, $x = 20$ mm, a) $We = 36.7$, b) $We = 44.5$, c) $We = 52.8$, and d) $We = 60$.	127
Fig. 7-10: Frequency of bubble count as a function of impact Weber number for different depth of fluid.	129
Fig. 7-11: Region of regular single bubble entrainment in the $We-Fr$ diagram, Ref: Pumphery and Elmore (1990).	130
Fig. 7-12: Variation the bubble count as a function of the film depth at 10 mm off-axis from the nozzle exit centerline.	131
Fig. 7-13: Variation the average bubble size with film depth for different impact Weber numbers.	131
Fig. 7-14: Variation the average ejecting (bubbles moving downward) and rising bubbles (moving upward) size with film depth.	132
Fig. 7-15: Variation the average a) ejecting bubble velocity, and b) rising bubble velocity, with film depth for different impact Weber numbers.	134
Fig. 7-16: Variation the average ejecting and rising bubble velocity with film depth for two different impact Weber numbers.	135
Fig. 7-17: Shear lift force acting on an air bubble moving inside continues liquid film under spray impact.	136
Fig. I-1: Nomenclature for impinging and ejecting droplets from wall.	141
Fig. I-2: Mass fraction of secondary droplets versus non-dimensional impact velocity (Stanton and Rutland 1996).	146
Fig. I-3: Deposition rate of spray impact onto thin liquid film (Schmehl et al. 1999).	147
Fig. I-4: Deposition/Splashing border for single droplet impacting onto a cold-dry wall (Schmehl et al. 1999).	147

List of Tables:

Table 3-1: Classification of film thickness formed on the wall due to spray impact based on experimental data from Wang and Chen, (2002).	36
Table 3-2: Asymptotic values for characterization of cavity and uprising central jet.....	37
Table 3-3: Summary of the average measured quantities at a single measurement point, and the minimum number of required samples computed by (3.3) at the level of 5% and 1%. .	41
Table 3-4: Summary of the measured range of quantities.....	43
Table 3-5: Excerpt from the Table of Snedcore and Cockran (1989) for correlation factor test (r-test).....	45
Table 3-6: Summary of the empirical model for a water spray impact onto small flat and rigid walls.	66
Table 7-1: Air bubble rise velocity as a function of bubble size in a stationary water pool.	133

Nomenclature:

Latin characters

Latin character	definition	scale	description
A		-	Area, coefficient
a		-	Coefficient
C		-	Coefficient
d		m	Drop diameter
D		m	Target diameter, diameter of cavity in splash
Eo	$(\rho_l - \rho_g)gd_b^2/\sigma$	-	Eötvös number
f		1/s	Frequency
F		N	Force acting on a drop or bubble
Fr		-	Froude number
g		m/s ²	Acceleration of gravity
h		m	Film thickness, height of central jet
K		-	Non- dimensional splashing threshold
L		m	Length scale
l^*	$[2\sigma/(\rho g)]^{1/2}/d_b$	m	Dimensionless capillary length
La	$\rho\sigma d_b/\mu^2$	-	Laplace number = $1/Oh^2$
m		kg	Mass
Mo	$(1 - \rho_g/\rho_l)g\mu_l^4/\sigma^3$	-	Morton number
N		-	Number of droplets or bubbles
Oh	$\sqrt{We/Re}$	-	Ohnesorge number
P		N/m ²	Pressure
q			Flux of impinging or ejecting droplets
Re	$\rho u d_b/\mu$	-	Reynolds number
s		m	Thickness of the crown rim in splash
t		s	Time
T		s	Transient time
u		m/s	Velocity normal to the wall
v		m/s	Velocity parallel to the wall
V	$\pi d^3/6$	m ³	Volume of a spherical bubble
We	$\rho u^2 d_b/\sigma$	-	Weber number
X		m	Spatial coordinate perpendicular to wall
Z		m	Spatial coordinate parallel to wall

Greek characters

Greek character	scale	Description
α	-	Coefficient
β	-	Non-dimensional maximum droplet spreading diameter
Γ	-	Source term
δ	m	Film thickness, thickness of the boundary layer
ε	m	Surface roughness
η	-	Constant value
θ	°	Trajectory angle
λ	-	Void fractions
μ	Kg/ms	Dynamic viscosity
ξ	-	Maximum dimensionless diameter
ρ	Kg/m ³	Density
σ	N/m	Surface tension
τ	N/m ²	Shear stress
Ω	m ³	Volume of boundary layer of the spreading droplet

Subscripts

Subscript	Description
<i>0</i>	Before the impact, initial value
<i>10</i>	Mean diameter
<i>30</i>	Sauter mean diameter
<i>a</i>	After impact
<i>adv</i>	Advancing
<i>b</i>	Before impact
<i>B</i>	Crown base
<i>C</i>	Crown
<i>D</i>	Drag
<i>dep</i>	Deposition
<i>diss</i>	Dissipation
<i>g</i>	Gas phase
<i>H</i>	Crown height
<i>l</i>	Liquid phase
<i>max</i>	Maximum
<i>MV</i>	Measurement volume
<i>n</i>	Normal component
<i>sp</i>	Spreading
<i>t</i>	Tangential component

Symbols

Symbol	Description
*	Dimensionless
-	Average, mean
'	Fluctuation of the mean value
Σ	Sum
Δ	Second order of gradient operator

Abbreviations

Abbreviations	Description
CV	Control volume
PDA	Phase Doppler measurement technique
CCD	Charge Coupled Device
CMOS	Complementary Metal Oxide Semiconductor

Chapter 1

1. Introduction

Spray impingement onto rigid walls occurs in many industrial and technical applications, such as direct injection in Diesel engines, gas turbines, agricultural sprays, spray cooling, spray painting and spray coating. Physically two important interacting hydrodynamic phenomena must be correctly captured in describing spray impact: the generation of secondary droplets and the liquid film accumulating on the wall, Kalantari and Tropea (2006d, and e). The origins of secondary droplets are: from a splash with disintegrating crowns, liquid jetting from the liquid film, or from rebounding droplets. The overall structure of the accumulated wall film consists of deposited droplets and partial deposition of splashing droplets.

Often the deposited film on the wall should be avoided as far as possible, e.g. during the start up of Diesel engines, whereas in some other cases a maximum deposition is required, e.g. in spray coating, spray cooling and spray painting or agricultural sprayers. On the other hand, the induced fluctuations in the liquid layer formed on the rigid wall may decrease the quality of coated or painted surfaces. We can therefore not expect universal design guidelines for spray impact systems but rather a predictive capability for parameters such as deposited mass, secondary spray characteristics or film dynamics are desirable. These goals have often been the underlying motivation for many past studies, even if they have not always been explicitly stated.

Much of the previous literature on the topic of spray impact has been restricted to the **normal** impact of a single drop onto a solid, dry or wetted wall, or sometimes onto a thin liquid film, where generally the impact conditions can be carefully controlled; see e.g. Bai and Gosman (1995), Stanton and Rutland (1996), Mundo et al. (1998), and Marengo and Tropea (1999). In many cases the results of single droplet normal impact are extrapolated to the case of spray/wall interaction by simple superposition of many

individual droplets. Such an approach however cannot capture many essential physical effects influencing the behaviour of deposited film or secondary spray: the tangential momentum of oblique impacting droplets that exist in the case of real spray; effect of film fluctuations on the outcome of impacting droplets; effect of multiple droplet interactions, the creation of the central jets and droplets due to break-up of the liquid film under impacting drops, and also interaction between uprising jets or crowns with in-going drops or other splashing droplets. Indeed it has become apparent in recent years that the liquid film formed on the surface plays an important role in determining the velocity and size of ejected droplets as well as the deposited mass fraction, see e.g. Kalantari and Tropea (2006d).

Formation of the wall film is often neglected in spray impact models. However, prediction of average film thickness and average film velocity is very important for many industrial applications, especially involving spray cooling systems or for fuel injection sprays onto heated walls, because these parameters significantly affect the efficiency of heat transfer through the sprayed surfaces. Furthermore, the average film thickness can affect the properties of secondary spray, splashing threshold, ejected mass and number of secondary droplets, Cossali et al. (1997), Wang and Chen (2002), Kalantari and Tropea (2006b). It has been shown by Cossali et al. (1997) that in the case of a single drop impact onto a stationary liquid film, the number of secondary droplets decreases as the depth of liquid layer is increased. For indicating the influence of the average liquid film thickness on the splash limiting criterion, several expressions have been introduced, e.g. $K_{Cr} = 2100 + 5880 \cdot \bar{h}^*$ ($\bar{h}^* = \bar{h}/d_b$, where \bar{h} is the average film thickness and d_b is the drop diameter before the impact) by Cossali et al. (1997). In this criterion, splashing occurs if: $K = We \cdot Oh^{-0.4} > K_{Cr}$, where Oh is Ohnesorge number defined as: $Oh = \sqrt{We}/Re$, and the Weber and Reynolds numbers are defined as: $We = \rho u^2 d_b / \sigma$ and $Re = \rho u d_b / \mu$ respectively.

This brief survey of literature and phenomenological characterization of spray impact leads us to two fundamental conclusions: Modelling spray impact must consider also the presence and influence of the accumulated wall film; Models based solely on the impact of single droplets will miss many essential elements of spray impact. These conclusions are motivation to formulate models derived from spray impact data

obtained under controlled boundary conditions; hence also the motivation to perform such experiments.

1.1. Goals and contribution of the present approach

The main goal of the present study is to broaden the present understanding of the spray/wall interaction phenomena. First of all, a complete and extensive literature review regarding the single drop impact and spray impact is performed to understand the problems and to be familiar with previous work. A phenomenological study of spray impact onto a flat and rigid wall is conducted with the help of a high speed camera to better understand the structure of an impacting spray, especially focused on the behaviour of splashing droplets in spray impingement and ejection of the wall liquid jets. In the next step, some important considerations for phase Doppler measurements of a spray impact onto a rigid wall are performed and a new empirical model for predicting the characteristics of the secondary spray is derived, based on the many individual experiments with a phase Doppler instrument. After that, the study focuses on the accumulated wall film formed due to a liquid spray impact. In this part, the experimental results are complemented by theoretical expressions regarding the hydrodynamics of liquid films under sprays and preliminary models for the average wall film thickness and secondary spray are formulated.

The most important contributions to understanding the spray/wall interaction in this thesis are listed below:

- Important and key considerations in Phase Doppler measurements of spray impact onto a rigid wall.
- Characterization of the secondary spray formed by an inertial (i.e., $We/\sqrt{Re} \gg 1$) liquid spray impinging onto a rigid wall. The secondary spray is characterized in terms of correlations for the velocity and trajectory of secondary droplets and the mass and number ratio of the secondary spray.
- Experimental characterization and empirical modelling of the accumulated wall film formed by an inertial liquid spray impinging onto a rigid wall.
- Fundamental comparison of the splashing phenomena for single drops and for drops in a spray.
- Characterization of oblique and normal impingement of inertial sprays.

- Experimental study for different aspects of liquid spray impact onto a deep liquid layer.

1.2. Thesis Outline

In this thesis, the literature review of previous investigations is distributed throughout different chapters based on the subject and goal of each chapter. Each chapter covers one aspect of the spray/wall interaction phenomena.

In chapter 2, some considerations for phase Doppler measurements of a spray impact onto a rigid wall are presented in more detail. This part of the work provides experimental results indicating the influence of the measurement volume height above the rigid wall, the influence of the input laser power and the spatial location of the detection volume on the measured characteristics of the impinging and secondary spray.

In chapter 3, qualitative and quantitative characterization of spray impact onto flat and rigid walls together with characterization of the accumulated wall film is presented. These characterizations have been obtained by means of the phase Doppler technique, a high speed CCD camera for measuring the average film thickness accumulated on the wall and a second high-speed CMOS camera with 32 kfps for capturing the deposited, rebounded or splashed droplets. Results obtained in this chapter address the limitations, difficulties and complexities of modeling and capturing the spray impact phenomena. This work also indicates the limitations and disadvantages of importing the results from isolated single drop or a train of drop impacts onto a rigid wall or liquid films to a spray impact. In this chapter, average characteristics of the secondary spray (e.g. mean drop diameter, velocity, and trajectory, mass and number ratio) have been presented and empirical models have been formulated on the basis of average quantities before the impact.

In chapter 4, formation and spreading of the thin liquid film formed on the rigid wall due to a liquid spray impact is experimentally characterized. Then a theoretical model for predicting the average film thickness formed on the rigid wall is derived based on the hydrodynamics of a spreading thin liquid film on the rigid wall. Results of this model are compared with many individual experimental results. Also in this chapter the influence of the average film thickness on the secondary spray is presented.

In chapter 5, a fundamental comparison of the splashing phenomenon for single drops and for drops in a spray is discussed, followed by a derived theoretical model. Such comparisons can be very valuable for future modelling of spray impact. The theoretical prediction is then compared with available measurement results for single drop impact and spray impact conditions. For characterization of the splashing droplets, a high-speed camera with 32 kfps has been used.

In chapter 6, an experimental study for oblique spray impingement onto a flat and rigid surface is presented and compared with the results obtained for the normal spray impingement condition. In this chapter, some general conclusions are drawn about the mean statistics of ejected drop properties in dependence of impinging drop properties for the oblique impingement conditions.

In chapter 7, an experimental study is presented for different aspects of liquid spray impact onto a deep liquid layer. In this chapter especially the air bubble entrainment into the liquid film is discussed in more details.

Finally, in chapter 8, the main achievements of this study are summarized, and some useful suggestions for future works are given.

Chapter 2

2. Phase Doppler Measurements of Spray/Wall Interaction

After an introduction to computation of the flux and concentration by the phase Doppler system, an experimental study of spray impact onto a horizontal flat and rigid surface is presented to empirically specify a suitable measurement volume height above the surface in which the phase Doppler measurements are valid. Furthermore the influence of the input laser power on the characteristics of the impinging and secondary spray is studied in detail. The phase Doppler technique has then been used to characterise both the impacting and the secondary spray in terms of number flux, size distribution and velocities of the droplets above a target. A high-speed CCD camera has been used to characterize the splashing or rebounding droplets and to measure the average film thickness formed due to spray impact.

2.1. Introduction

Sprays are typically characterized by statistical quantities obtained from size and velocity measurements over many individual droplets. The most widely used quantities are size and velocity probability density distributions as well as fluxes, e.g., number, mass, momentum etc. Through a given plane, some instruments infer such statistical quantities from individual measurements, e.g., number density from light extinction, but very few instruments are capable of making direct size and velocity measurements of individual droplets in a spray. A good overview of available instruments is given in Webb and Jones (2003).

Of these measurements, the phase Doppler instrument is the most widely used for sprays in which the drop diameter is in the range of $1 \mu\text{m} < d < 1 \text{ mm}$. An important prerequisite for using the phase Doppler instrument is that the droplets are spherical, which due to surface tension, is generally fulfilled for almost droplets and for droplets experiencing lower aerodynamic deformation forces. However, there are several additional pitfalls when using the phase Doppler instrument in a spray impinging on a wall, which must be considered in the optical setup and the data processing to avoid serious bias errors. These procedures are introduced and verified in the present chapter. The phase Doppler technique is a counting technique which measures the velocity and size of each individual droplet from the Doppler frequency and phase shift of the scattered light respectively. The output of the signal processor of a Phase Doppler instrument consists of the arrival time (the time that a particle arrives in the measurement volume), transit time (duration the particle resides in the measurement volume), two (or three) components of velocity, particle size and also the phase difference between detectors for each detected droplet. From these primary measurement quantities, it is possible to compute various statistic quantities to characterize the impinging and secondary sprays; for example size and velocity distributions, fluxes (number, mass, etc.) or concentration. However, to non-biased statistics of these quantities, it is necessary to take into account the exact optical specifications of the system: well-known effects to be considered include the slit effect, Gaussian beam effect, and presence of multiple droplets in the measurement volume simultaneously or the drop size-dependent detection volume. These effects are well documented in the literature, see e.g., Xu and Tropea (1994), Albrecht et al. (2003), and Sommerfeld and Qiu (1995), and most commercial systems provide means either eliminate the major errors or to chose an adequate estimator.

In the following discussion, the estimators used for most of the experimental investigations will be briefly reviewed. Nevertheless, there arise some special considerations for measurements near the wall under an impacting spray, and these will be considered in section 2.5.

2.2. Computation of statistical quantities

Regardless which statistical quantity is to be estimated from the primary measurement quantities, it is necessary to insure that statistics are collected over a constant reference area or volume. This is not automatically fulfilled with the phase Doppler instrument because the detection volume is size dependent, an effect arising from the fact that scattered light intensity is proportional to the square of the droplet diameter. Therefore any statistic must include a correction factor accounting for this size dependent detection volume. In the following sub-sections an expression will be given for estimating the size-dependent detection volume diameter.

2.2.1. Determination of efficient detection volume size

Due to the Gaussian profile of the laser beams or measurement volume, small particles passing through the edge of the measurement volume scatter not enough light and therefore detectors are not be able to detect them. For taking this into account, one must consider smaller detection volume diameter for smaller droplets, called droplet size dependent detection volume diameter $d_e(d_{pi})$. In the following section, a theoretical expression for particle size dependent detection volume diameter will be presented.

Based on geometrical optics ($d_p \gg \lambda$), intensity of the scattered light is proportional to the droplet diameter squared, see e.g. Albrecht et al. (2003).

$$I_s \propto d_p^2 \quad (2.1)$$

Intensity of the scattered light by this particle at the position of the receiving detector is

$$I_s = G \cdot \bar{I}_i \cdot d_p^2 \quad (2.2)$$

where \bar{I}_i is the average incident light intensity on the particle, I_s is the scattered light intensity at the position of the receiver, and G is a parameter related to the optical characteristics of the particle and also the medium.

For droplets much smaller than the measurement volume size, i.e., $d_p \ll d_e$, variation of the laser light intensity on the droplet is assumed to be linear over its diameter; therefore the average intensity can be expressed by (see Fig. 2-1)

$$\bar{I}_i = \frac{1}{A_p} \int_{(d_c-d_p)/2}^{(d_c+d_p)/2} 2I_i \cdot y dx = I_i \left(\frac{d_c}{2} \right) \quad (2.3)$$

where A_p being surface area of the particle.

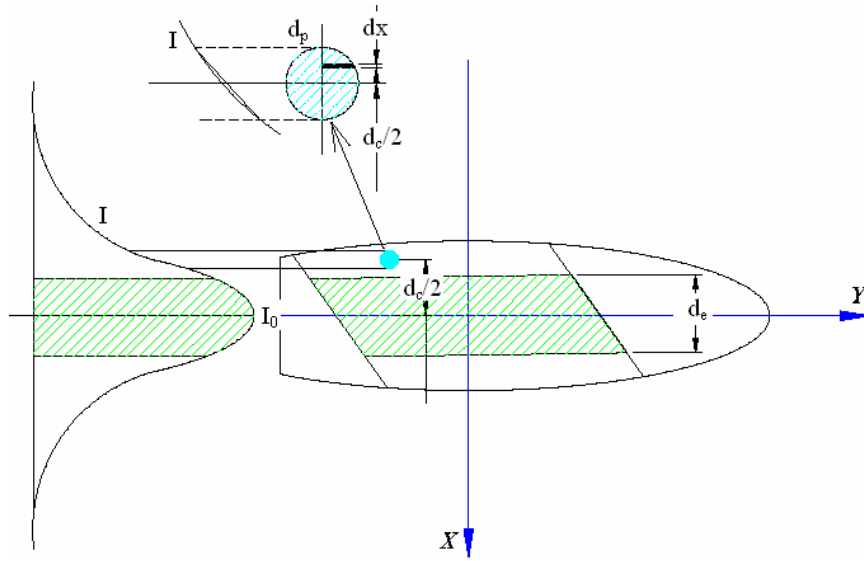


Fig. 2-1: Linear assumption for distribution of the laser light on small particles in compare to the measurement volume size.

On the other hand, intensity of the laser light at the position of the particle inside the measurement volume is related to its distance from the center of the measurement volume in the form of

$$\bar{I}_i \left(\frac{d_c}{2} \right) = I_0 \cdot \exp \left[-2 \left(\frac{d_c}{d_0} \right)^2 \right] \quad (2.4)$$

where d_c is the diameter corresponding to the position of the particle. Nominal diameter of the laser beam (d_0) in Eq. (2.4) is a constant value depending on the beam waist diameter of the focused laser beams and beam intersectional angle and defines where the intensity of the laser light decreases to e^{-2} of its value at the centre of the laser beam.

Particles with diameter of d_p only can be detected inside a certain region defined by d_e , where intensity of the scattered light in this region is larger than a certain minimum value ($I_{s.min}$). Therefore maximum detectable region for particle with diameter of d_p is defined by $d_c = d_e$, see Fig. 2-1.

By considering expressions 2.2, 2.3 and 2.4 with $d_c = d_e$, effective diameter of the measurement volume can be expressed as

$$\left(\frac{d_e}{d_0}\right) = \text{Ln}(d_p) - \frac{1}{2} \left[\text{Ln}\left(\frac{I_0}{I_{s.min}}\right) - \text{Ln}(G) \right] \quad (2.5)$$

Or

$$d_e = d_0 \sqrt{\text{Ln}(d_p) - \frac{1}{2} \text{Ln}\left(\frac{I_{s.min}}{G \cdot I_0}\right)} = d_0 \sqrt{\text{Ln}(d_p) - C_1} \quad (2.6)$$

where $C_1 = \text{Ln}\left(\frac{I_{s.min}}{G \cdot I_0}\right)^{1/2}$ is a complex optical parameter coupling the optical characteristics of the particle and the medium, power of the laser beam (I_0) and minimum intensity required to detect the particle ($I_{s.min}$). The value $I_{s.min}$ depends on the characteristics of the detectors, gain of the system, photomultiplier high voltage and scattering angle of the detectors (ϕ); therefore a direct measurement of the coefficient C_1 is impossible. Consequently (2.6) has two unknown values d_e and C_1 , indicating that another expression for d_e is necessary. For this effort consider a measurement volume with diameter of $(d_e)_k$ for a given size class k. Mean burst length for this size class is defined by

$$\bar{L}_k = \frac{\sum_{i=1}^{N_k} L_i}{N_k} \quad (2.7)$$

where L_i is burst length of the particle passing through the measurement volume computed by

$$L_i = (t_{trans})_i \cdot \sqrt{u_i^2 + v_i^2} \quad (2.8)$$

If the detector counts enough number of droplets for a given size class (droplets inside a given size class have statistically the same diameter) and also measure their Burst lengths, then the mean burst length can be mathematically estimated by, see Fig. 2-2.

$$\bar{L} = \frac{1}{d_e} \int_{-d_e/2}^{d_e/2} 2\sqrt{(d_e/2)^2 - z^2} dz = \frac{1}{d_e} \cdot A(d_e) \quad (2.9)$$

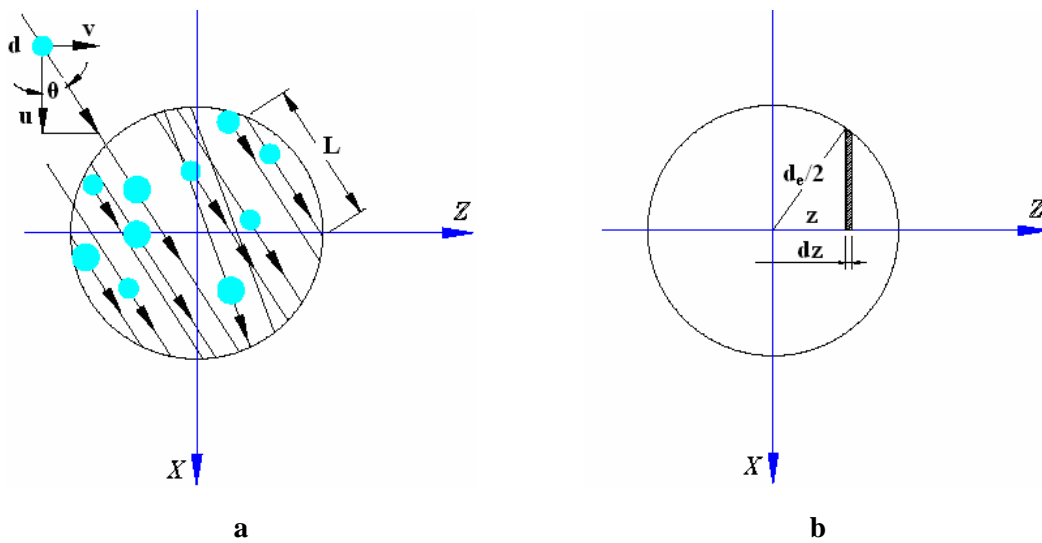


Fig. 2-2: a) Sketch for statistically distribution of the burst lengths inside the detection volume and droplet trajectory, and b) mathematical element (dz) of detection volume to be integrated yielding the mean burst length.

With considering effective measurement area $A(d_e) = \pi d_e^2 / 4$, the obtained expression (2.9) is simplified to

$$d_e = \frac{4}{\pi} \bar{L} \quad (2.10)$$

It is worthy to mention here the other available expressions for estimating the effective measurement volume diameter given by Dantec dynamic Co. (2002) in Eq. (2.11), and by Roisman and Tropea (2001) in Eq. (2.12).

$$d_e = \sqrt{\frac{3}{2}L^2} \quad (2.11)$$

$$d_e = \frac{4}{\pi} \frac{I_s \sum_{i=1}^{N_{pd}} L_i}{N_{pd} I_s - \left| \cos \varphi \right| \left| \sum_{i=1}^{N_{pd}} L_i \theta_i \right|} \quad (2.12)$$

where N_{pd} represents the total detected particles.

Obtained value for d_e either by Eq.2.10, or 2.11 or 2.12 is the effective measurement volume diameter that outside of it will not be detected any droplet with diameter smaller than d_p . In practice d_e is usually smaller than d_0 but can be sometimes larger than d_0 if particles with a good optical transmitting properties are detected in the region $(I_c/I_0) \leq e^{-2}$. With increasing droplet diameter, effective measurement volume diameter (d_e) also increases for small particles, then after a certain value of droplet size d_e does not change significantly and therefore no strong variation of d_e for relative large particles is predicted, see Fig. 2-3. It is even more interesting that the effective measurement volume diameter decreases after a certain value of drop size, e.g. 58 μ m in this figure.

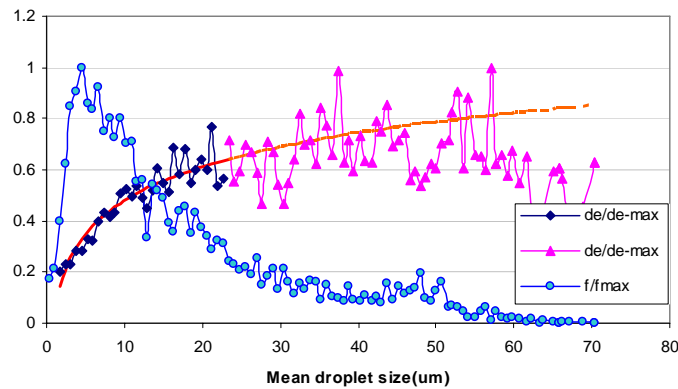


Fig. 2-3: Effective measurement volume diameter for number count >50, (normalized by the maximum values).

Considering Eqns. 2.6 and 2.10 together gives another expression for relationship between the mean burst length and the particle size for a given size class, in which the unknown parameter C_1 can be extracted from it.

$$(\bar{L})^2 = \left(\frac{\pi d_0}{4} \right)^2 (\text{Ln}(d_p) - C_1) \quad (2.13)$$

Or,

$$\bar{L} = \frac{\pi d_0}{4} \cdot (\text{Ln}(d_p) - C_1)^{1/2} \quad (2.14)$$

The coefficient C_1 in (2.14) can be obtained from correlation between the mean burst length and particle diameter for size classes with statistically enough number of samples inside it, e.g. $N_k > 50$.

2.2.2. Computation of statistical quantities in spray

In the Phase Doppler measurement technique, obtaining the fluxes and concentration necessitates capturing all droplets passing the measurement volume, which is impossible in the practical condition. In this section, suitable estimators for taking these criteria into account for measurements based on two velocity components are presented.

The volume flux in each direction inside a Cartesian coordinate system can be expressed as (Dantec Dynamics Co. 2002):

$$F_{\text{Vol.X}} = \frac{1}{T_{\text{acq}}} \cdot \left\{ \sum_{i=1}^{N_d} \frac{(\pi d_{pi}^3 / 6)}{\eta_{\text{val}} \cdot A_X(d_{pi})} \cdot \cos \theta_i \right\} \quad (2.15)$$

$$F_{\text{Vol.Z}} = \frac{1}{T_{\text{acq}}} \cdot \left\{ \sum_{i=1}^{N_d} \frac{(\pi d_{pi}^3 / 6)}{\eta_{\text{val}} \cdot A_Z(d_{pi})} \cdot \sin \theta_i \right\} \quad (2.16)$$

And number concentration as a scalar quantity can be estimated by

$$C(d_p) = \frac{1}{T_{\text{acq}}} \cdot \sum_{i=1}^{N_d} \frac{1}{\eta_{\text{val}} \cdot A_i(d_p, \theta) \cdot \sqrt{u_i^2 + v_i^2}} \quad (2.17)$$

where η_{val} is the validation coefficient representing the validated samples or signals defines as

$$\eta_{\text{val}} = \left(\frac{N_{\text{val}}}{N_{\text{atmp}}} \right) \quad (2.18)$$

Here N_{atmp} and N_{val} are number of the attempted and validated samples or signals respectively.

In Eq. (2.17), $A_i(d_p, \theta)$ is the reference cross-sectional area normal to the trajectory of droplet and is droplet size and trajectory dependent, which can be expressed in the form of

$$A_i(d_p, \theta) = A_{X_i}(d_p) \cdot \cos \theta_i + A_{Z_i}(d_p) \cdot \sin \theta_i \quad (2.19)$$

where θ represents the trajectory of each particle, defined by (Fig. 2-2)

$$\theta_i = \tan^{-1} \left(\left| \frac{v_i}{u_i} \right| \right) \quad (2.20)$$

$A_X(d_p)$ and $A_Z(d_p)$ are effective cross-sectional areas or size dependent detection areas in x and z direction respectively.

$$A_X(d_{pi}) = \frac{d_e(d_{pi}) \cdot L_s}{\sin \varphi} \quad (2.21)$$

$$A_Z(d_{pi}) = \frac{d_e(d_{pi}) \cdot L_s + (\pi \cdot d_e^2(d_{pi}) / 4) \cdot \cos \varphi}{\sin \varphi} \quad (2.22)$$

where $d_e(d_{pi})$ is the effective detection volume diameter given by Eq. (2.6) and φ is the scattering angle.

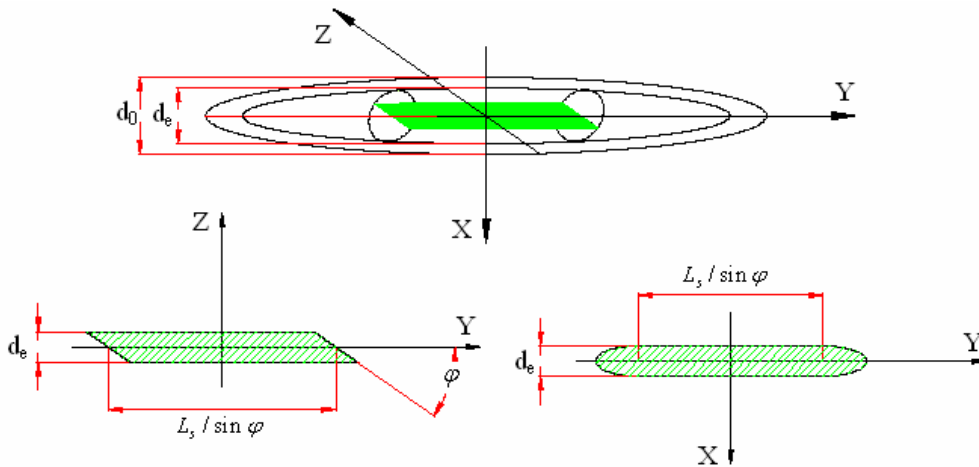


Fig. 2-4: Effective measurement cross sectional area in two directions.

The number counts or probability density distribution for each size class (*pdf*) must be also corrected, since the reference area for counting the droplets is not the same for all of the size classes. On the other hand, the validation ratio (η_{val}) may also change for different size classes. Therefore the corrected value of number counts for each size class can be introduced in the form of

$$(f_k)_{corr.} = f_k \cdot \frac{A_{max}}{\eta_{val} \cdot A_X(d_p)_k} \quad (2.23)$$

where f_k and $(f_k)_{corr.}$ are the measured and corrected number counts for each size class respectively. A_{max} is the measurement reference area for the largest measured size class, which in a simple way can be approximated by the nominal measurement area (A_0) defined by

$$A_0 = \frac{d_0 \cdot L_s}{\sin \varphi} \quad (2.24)$$

The derived expressions in this section for improving the measured quantities of a free atomizing spray, i.e., spray transport without wall impact, can be easily introduced into the algorithms used in computation of the fluxes or concentration. But however, exact estimation of the flux or concentration in spray impact phenomena is much more complicated in compare to a free atomizing spray. Except the mentioned limitations in the introduction of this chapter (such as droplet size dependence of the measurement volume, trajectory effect and slit effect) separation of the multiple presences of droplets inside the measurement volume or missing droplets is very complicated between the impacting and ejecting droplets. To slightly overcome this limitation, the ratio of after-to-before impact values will be used for estimating the mass flux or number flux ratio in this study. With using the after-to-before impact ratio, the measurement uncertainty can be modified for both impacting and ejecting droplets. In other words, missing the droplets passing through the measurement volume due to simultaneously presence of multiple droplets inside the measurement volume or due to the slit effect or trajectory effect can be modified by dividing these two quantities. For example, missing the 10% of ejecting droplets will be modified with missing the same order of magnitude of impacting droplets; therefore this ratio is automatically modified.

Second, the detected impinging or secondary droplets do not necessarily originate from the same spatial location of the measurement volume of the instrument. Especially the last effect makes computation of the mass or number flux of the secondary droplets very complicated, since the secondary droplets have wider distribution of the trajectory from the target surface. This effect will be discussed in this chapter.

2.3. Summary of computed procedure

The derived procedure for computing the fluxes and concentration of the spray can be summarized as follows:

- 1- Sort the raw data (obtained from output of the Phase Doppler signal processor) for each measurement point based on the particle diameter.
- 2- Make enough size classes such that at least 20 of them contain 50 or more samples.
- 3- Calculate the mean burst length (\bar{L}) and effective measurement volume diameter (d_e) for each size classes based on the given expressions; Eqns. 2.7, 2.8, and 2.10.
- 4- Plot the computed $\left(\frac{d_e}{d_0}\right)^2$ as a function of particle diameter (d_p) for size classes containing the 50 or more samples. Then obtain the coefficients α_1 and β_1 for $\left(\frac{d_e}{d_0}\right)^2 = \alpha_1 \cdot \ln(d_p) - \beta_1$ via best curve fit, as shown for an exemplary case in Fig. 2-3.
- 5- Compute the d_e for each particle based on the obtained correlation (given in point 4) and use the (Eqns. 2.19, 2.21, and 2.22) for calculating the effective cross sectional area.
- 6- Compute each component of the flux and the concentration based on the given equations in this chapter; Eqns. 2.15, 2.16, and 2.17.

2.4. Experimental set-up

The experimental set-up used in this work is pictured in Fig. 2-5. The spray was created using different full-cone nozzles from Spraying System Co., operated at pressures between 2 and 7 bar and flow rate between 27 and 40 lit/hr. Both flow rate and pressure during the experiments were variable and measured. A stainless steel target

with diameter of 5mm has been used to obtain the results presented in this chapter, using the end face of the cylinder.

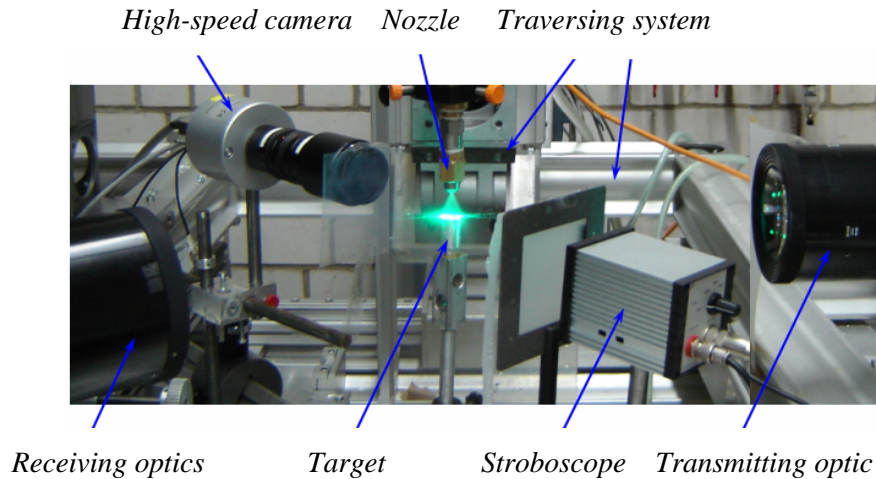


Fig. 2-5: Photograph of experimental set-up used in this study.

The nozzles were placed at different positions above the target surface from 20 to 50 mm with interval of 10 mm, e.g. ($x_{nozzle} = -20$ mm). To characterise the spray, a dual-mode phase Doppler instrument from Dantec Dynamics was used, comprising a transmitting optics with a 310mm focal length, a receiving optics with a 310mm focal length, and an “A” type mask at a 36° scattering angle. By using a dual-mode configuration both normal and tangential velocity components of each individual droplet and its diameter were measured by placing the measurement volume 0.25mm to 2.5mm above the target surface (e.g., $x = -1$ mm). The in-going and out-going droplets are distinguished using the sign of the velocity component normal to the target, i.e. positive u denotes an impacting droplet and a negative u denotes a secondary droplet. The overall size distributions were corrected for the size dependent detection volume cross-section using the standard system software.

For precisely definition of the measurement volume height above the wall, first the blue laser beams in the horizontal plane were blocked and the measurement volume created by the green laser beams was placed precisely at the centre of the target by horizontally or vertically movement of the target, Fig. 2-6.

The measurement volume is positioned precisely at the target centreline when the target edges touch simultaneously the green laser beams, i.e., points “a” and “b” in Fig. 2-6a touches the laser beams at the same time. In the next step, the green laser beams in the vertical plane were blocked and the blue laser beams in the horizontal plane were used to find the zero-position of the measurement volume height. In this step, the target moved only vertically to touch the laser beams. The touched position of the target was defined as $x_{MV}=0$, see Fig. 2-6b.

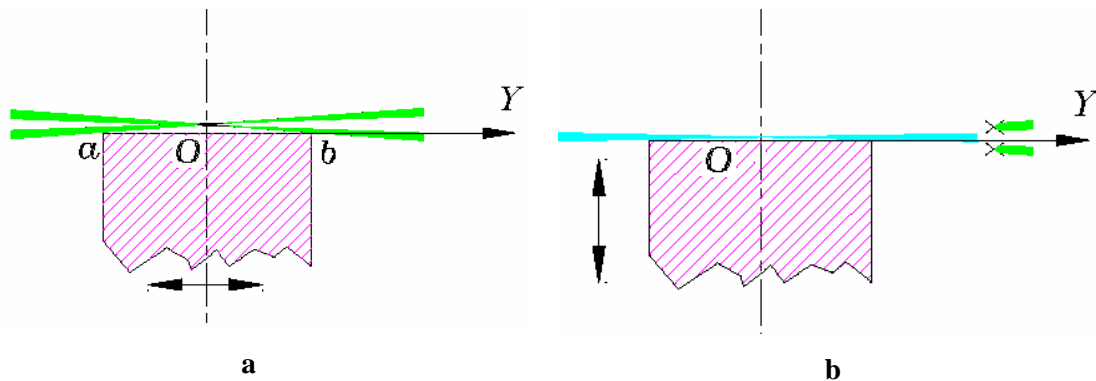


Fig. 2-6: Sketch for: a) positioning the measurement volume precisely at the target centreline, and b) zero-position of the measurement volume height.

Experimentally the accumulated wall film has been characterised using a high-speed CCD camera. The average wall film thickness (\bar{h}) is obtained by averaging over several instantaneous images after first removing the reference wall image.

2.5. Results and discussion

The most obvious difficulty is to specify the measurement volume height above the surface at which the phase Doppler data is valid. In Fig. 2-7a and b, the dependence of velocity before the impact and velocity after the impact are illustrated as a function of measurement height above the wall and the laser output power. This data has been taken in a reasonably sparse spray impacting onto a flat target with a relatively thin film. It illustrates that both the in-coming spray and the secondary spray can exhibit strong gradients of velocity in the wall normal direction. Although numerical simulations of the spray and the gas flow can capture such gradients, the synchronisation between

experiment and simulations, either for model calibration or for verification of predictions, must take these gradients into account.

Results presented in Fig. 2-7a indicate that the mean velocity before the impact increases significantly with the measurement volume height above the wall. Also these results indicate that the mean impact velocity decreases with the input laser power. The influence of the laser power on the mean drop impact velocity is stronger (larger) at lower laser powers, as illustrated in Fig. 2-7a.

Other results presented in Fig. 2-7b indicate that the average velocity after the impact increases with the measurement volume height up to 2 mm, after which it doesn't change significantly. The influence of the laser power on the average velocity after the impact is not significant, as presented in Fig. 2-7b.

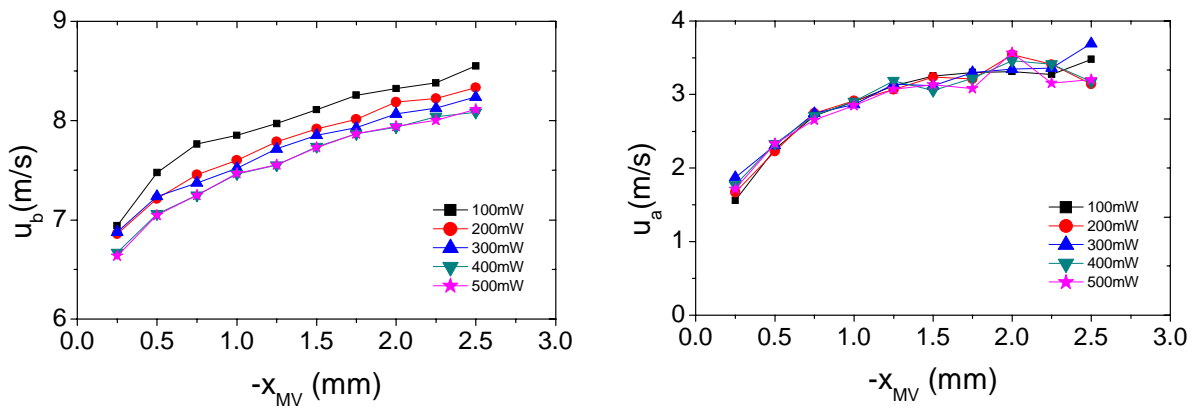


Fig. 2-7: Mean velocity a) before the impact and b) after the impact, as a function of measurement volume height above the rigid wall. The different lines represent different laser power.

The influence of the measurement volume height above the rigid wall and the laser output power on the measured average drop size before and after impact

$$(d_{10b} = \frac{1}{N_b} \sum_{i=1}^{N_b} d_{bi} \text{ and } d_{10a} = \frac{1}{N_a} \sum_{j=1}^{N_a} d_{aj} \text{ respectively}) \text{ are presented in Figs. 2-8 and 2-9.}$$

Results presented in Fig. 2-8 indicate that the average drop size before the impact decreases with measurement volume height above the target up to 1 mm, but doesn't change significantly after $x=1$ mm. Large differences in the average drop size before impact at a laser power =100 mW compare to other values can be observed in Fig. 2-8a.

This result can be important when measuring dense or ultra-dense sprays, in which the laser power at the both sides of the spray is not uniform. In other words, the laser intensity at the center of measurement volume can decrease significantly due to increasing the absorption and scattering the laser light by moving particles at the opposite side of the laser beams entering the liquid spray, i.e., opposite side of the transmitting optic. Therefore a calibration for Phase Doppler measurements is required at both sides of the dense sprays to obtain a reliable result. The influence of the laser power on the average drop size before the impact is significant in which d_{10b} decreases with increasing the laser power (Fig. 2-8b).

The influence of the measurement volume height on the average drop size after the impact is more complicated. The value of d_{10a} decreases at first with a measurement volume height up to 1.5 mm, then increases with the measurement volume height above the target. Based on the results presented in Fig. 2-9, the larger average secondary drop size very close to the wall can be due to the absence of the very small droplets generated from splashing droplets, since secondary droplets generated by splash cannot be captured very close to the wall. Increasing the average secondary drop size after a certain height above the wall, e.g. after $x_{MV}=1.5$ mm in this figure, can be due to interaction of the secondary droplets with other droplets and deposition of the generated secondary droplets due to larger trajectory angles and smaller velocity components normal to the wall. The influence of the laser power on the average after impact drop size is not significant, indicating that generation of the secondary droplets is a random phenomenon in contrast with the impacting droplets, see Fig. 2-9.

To capture all the generated secondary droplets, the measurement volume must be placed above all the splashing droplets in a spray. In other words, the measurement volume must be placed above the maximum height of all possible crowns generated by splashing droplets. In Fig. 2-10 the maximum non-dimensional crown height is presented as a function of Weber number before the impact for spray impact conditions and also for single drop impacts. Results presented in this figure indicate that the non-dimensional crown height increases linearly with Weber number before the impact. A linear correlation for non-dimensional maximum crown height in the case of spray impact condition can be given as

$$H_C^* = 3.9 \times 10^{-3} We_{nb} - 3.54 \times 10^{-2} \quad (2.25)$$

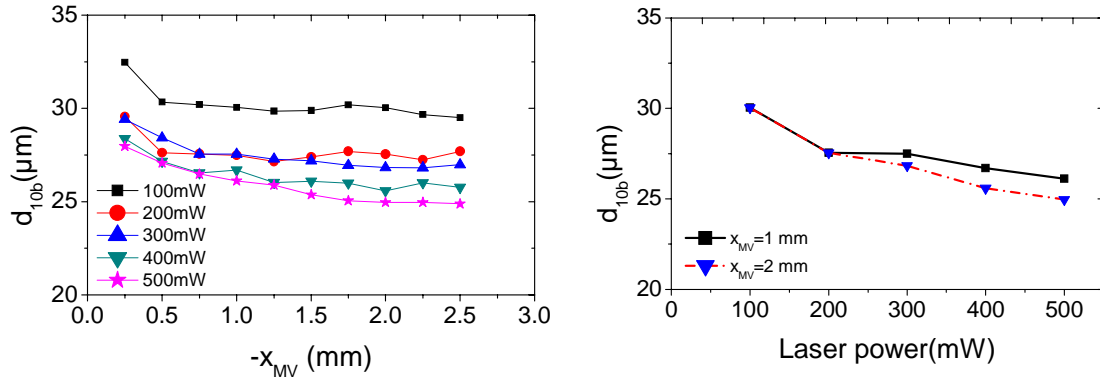


Fig. 2-8: Average droplet size before impact a) as a function of measurement volume height above the rigid wall (the different lines represent different laser power), and b) as a function of input laser power.

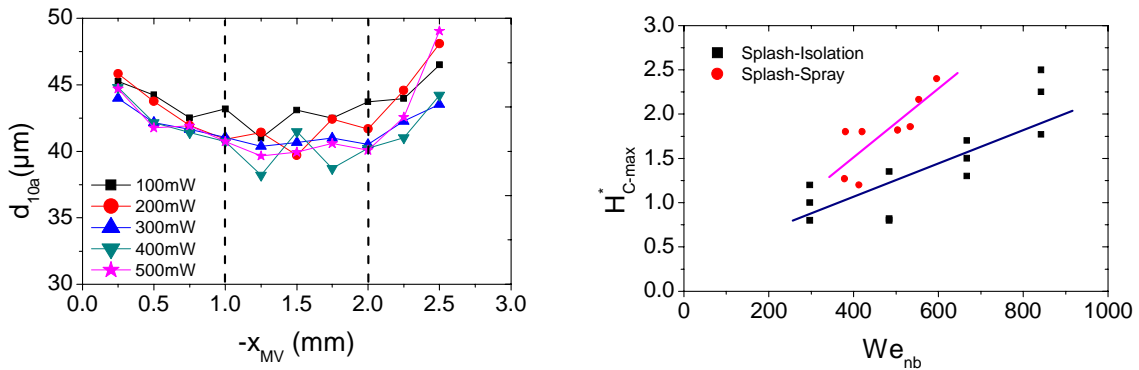


Fig. 2-9: Average droplet size after impact as a function of measurement volume height above the rigid wall (the different lines represent different laser power).

Fig. 2-10: Maximum non-dimensional crown height as a function of Weber number before the impact in spray and in isolation.

The difference in measuring the maximum crown height between spray impact conditions and isolation, i.e. single drop impact onto a stationary liquid film, indicates clearly that the splash created by a drop in a spray differs significantly from that of an isolated single drop impact or from the impact of a train of drops on a stationary liquid film. The source of such differences can be: tangential component of kinetic energy before the impact that exists under spray impact conditions, velocity field in the

accumulated wall film, velocity fluctuations in wall film, and fluid exerted into the crown body by neighbour impacting droplets. More details for estimating the maximum crown height and maximum height of single jets ejected from crown rim and comparison for splashing droplets in spray and isolation is given in chapter 5.

The total secondary-to-incident mass and number ratios show even stronger dependencies on measurement volume height above the target; hence this information is an important specification when employing such data as input data or verification data for numerical simulations. Furthermore, these dependencies can also depend on the wall film boundary conditions, i.e. on the liquid film thickness, Kalantari and Tropea (2006a, and d).

Two exemplary results are illustrated in Fig. 2-11 a and b, indicating the dependence of the total secondary-to-incident mass and number ratios on measurement volume height above the rigid wall. These results clearly indicate that total secondary-to-incident mass and number ratios decrease strongly with measurement volume height above the wall, but the influence of the laser power is not significant in most cases for both total secondary-to-incident mass and number ratios.

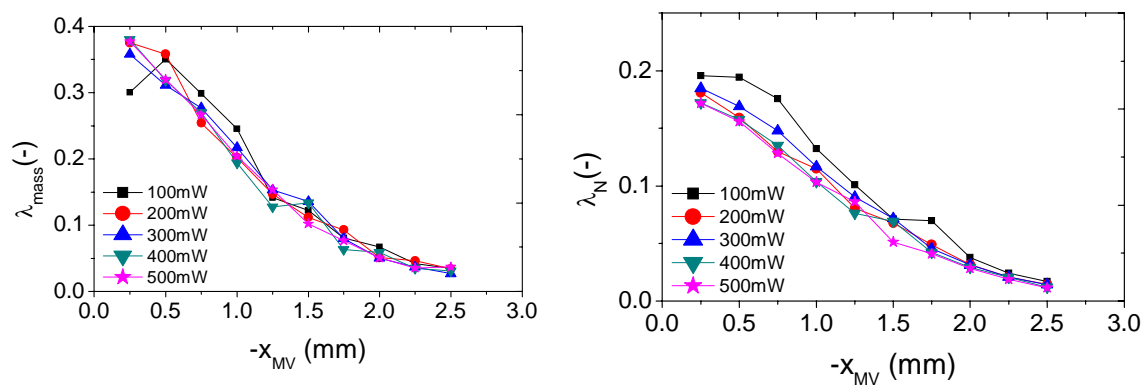


Fig. 2-11: Total secondary-to-incident a) mass and b) number ratios in spray impact onto a rigid wall. The different lines represent different laser power.

A second consideration is illustrated in Fig. 2-12 in which the positioning of a phase Doppler detection volume above an impact surface is pictured. Although highly simplified in the sense that all droplets are shown with the same velocity direction, this figure illustrates that the detected secondary droplets do not necessarily originate from

the same spatial location as the detected impinging droplets. This can be of importance when high spatial gradients of the impinging spray or of the liquid film on the wall exist, which is not unusual if the target surface is not flat. Furthermore, the drop trajectory must be accounted for when estimating the detection area size for the flux measurements, as discussed in previous publications by Roisman and Tropea (2001), and Albrecht et al. (2003).

Spatial location of the detected impinging (z_b) and secondary (z_a) spray can be expressed in the form, see also Fig. 2-12.

$$z_b = z_0 + |x_{MV} \cdot \tan \theta_b| \quad ; \text{ for before impact} \quad (2.26)$$

$$z_a = z_0 - |x_{MV} \cdot \tan \theta_a| \quad ; \text{ for after impact} \quad (2.27)$$

where x_{MV} is measurement volume height above the target and θ_b and θ_a are average trajectory angle of impinging and secondary droplets, respectively.

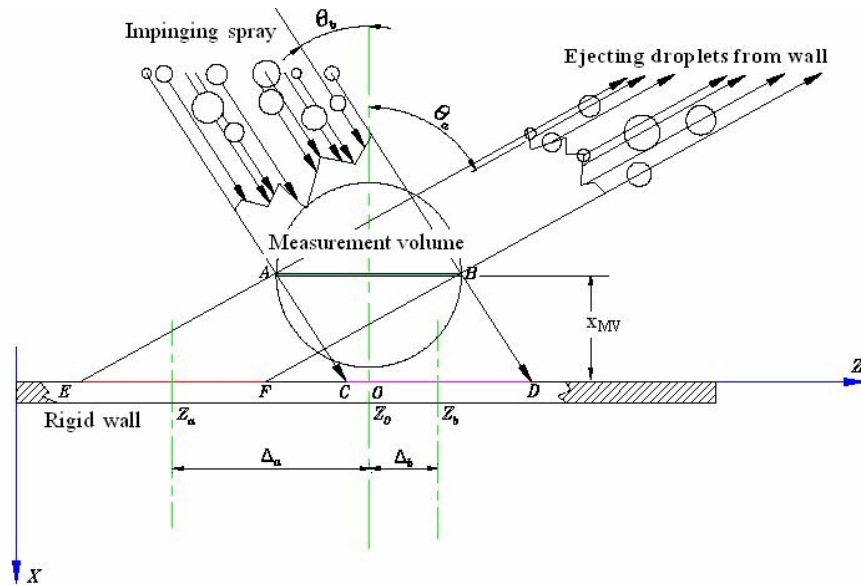


Fig. 2-12: Sketch for impinging and ejecting droplets passing through the detection volume.

Influence of such corrections discussed above (Eqns. 2.26 and 2.27) is presented in Fig. 2-13a for the normal velocity component before the impact and in Fig. 2-13b for

the normal velocity component after the impact. In these exemplary results, the measurement volume was placed 1 mm above a 15 mm rigid and flat target. As shown in this figure, the consideration is more significant for the secondary spray in comparison to the impacting spray, due to larger trajectory angles of the secondary droplets. The acquired measurements allow evaluating the rms of the impinging and ejecting angles; for data presented in Fig. 2-13a and b, the corresponding rms of the wall locations “ z_b ” and “ z_a ” fall in the range: $0.14 \leq \text{rms}|z_b - z_0| \leq 0.27$, and $0.38 \leq \text{rms}|z_a - z_0| \leq 0.65$.

The average film thickness in this study was in the range $20 \mu\text{m} < \bar{h} < 80 \mu\text{m}$, despite the fact the Weber number before the impact varied in the range $20 < We_{nb} < 150$.

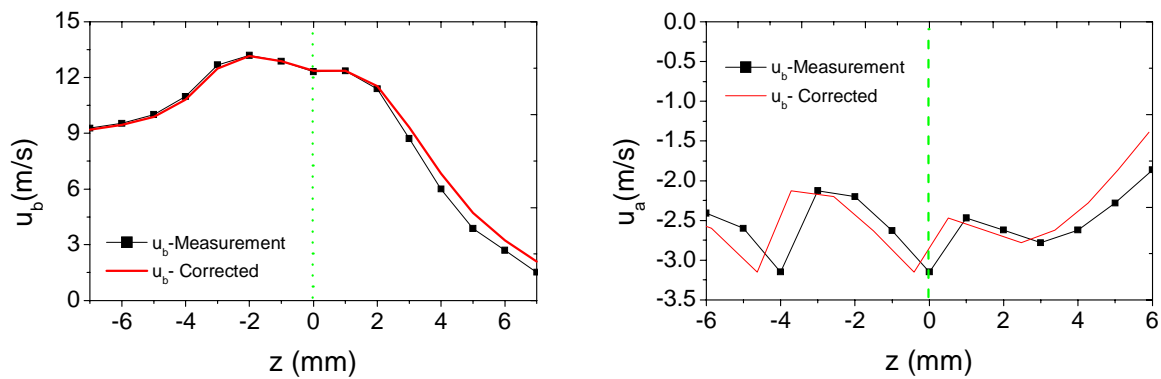


Fig. 2-13: Influence of correction for spatial position of the a) impinging droplet and b) secondary droplet.

2.6. Conclusion

An experimental study of spray impact onto a horizontal flat and rigid surface is performed to specify the measurement volume height above the surface at which the phase Doppler data is valid. Based on the conducted experiments in this study, the suitable measurement volume height above the rigid wall can be suggested in the range between 1 mm and 1.5mm for an inertial impact condition, independent of the film thickness and target size if thin liquid film condition exists. In this region, the average after impact velocity and drop size doesn't change significantly with measurement volume height and input laser power. However, total secondary-to-incident mass and

number ratios decrease significantly with measurement volume height in this region, but the influence of the laser power is not significant.

A measurement volume height less than 1 mm is not recommended based on the results obtained in this study, since the characteristics of the secondary spray, e.g. average drop size and velocity, change significantly in this region. This fact is mainly due to missing the generated droplets by splashing droplets or single jets ejected from accumulated wall film which will be discussed in more details in chapter 5.

The laser power has its strongest influence on the average drop size before the impact.

Chapter 3

3. Spray impact onto flat and rigid walls: Empirical characterization and modeling

In this chapter, an experimental study of spray impact onto horizontal flat and rigid surfaces is presented and used as input data for a new empirical model. To describe this phenomenon, the phase Doppler technique has been used to measure drop size and two components of velocity directly above the target. A high-speed CCD camera recorded the instantaneous film thickness formed due to spray impact. The spray-wall interaction has been characterized in the model in terms of correlations for the velocity and trajectory of secondary droplets and the mass and number ratio of the secondary spray. The novel aspect of the model is that the correlations are based on the mean statistics over many events in the spray and not on the outcome of single drop impact experiments. Another interesting feature of the experiments is the rather large range of oblique impact angles captured, due to the different drop trajectories exiting from the spray.

3.1. Introduction

Spray impingement onto walls occurs in many industrial and technical applications, such as direct injection in Diesel engines, gas turbines, agricultural sprays, spray cooling, spray painting and spray coating. Physically two important interacting

hydrodynamic phenomena must be correctly captured in describing spray impact: the generation of secondary droplets and the liquid film accumulating on the wall. The latter aspect often being neglected in spray impact models. However, prediction of average film thickness and average velocity is very important in the case of spray cooling systems or for fuel injection sprays onto heated walls because these parameters significantly affect the efficiency of heat transfer in the sprayed surfaces. Also the average film thickness can affect the properties of secondary spray, splashing threshold, ejected mass and number of secondary droplets.

In some applications, it is desirable to eliminate the deposited film on the wall as far as possible, e.g. in internal combustion engines, whereas in some cases the maximum deposition is required, e.g. in spray coating, spray painting or agricultural sprayers. On the other hand, the induced fluctuations in liquid layer formed on the rigid walls may decrease the quality of coated or painted surfaces.

Much of the previous literature on the topic of spray impact experimentally addresses deposition, usually being restricted to the normal impact of single droplets onto a solid dry or wetted wall or sometimes onto a thin liquid film, where generally the impact conditions can be carefully controlled, see e.g. (Bai and Gosman, 1995; Bai et al., 2002; Mundo et al., 1998; Stanton and Rutland, 1998), and such results serve as a basis for model formulations. Prevailing models extrapolate the results of single droplet impact to the case of a spray-wall interaction by simple superposition of many individual droplets. However such simplified models neglect to consider numerous effects regarding spray-wall interaction such as the influence of the deposited film on the secondary spray: the tangential momentum of oblique impacting droplets that exists in the case of real spray impact conditions; effect of film fluctuations on the outcome of impacting droplets; effect of multiple droplet interactions and also the creation of the central jets and droplets due to break-up of the liquid film under impacting drops or to the interaction between uprising jets or crowns with impacting drops or other splashing droplets.

Our observations and that of other investigations, e.g. Sivakumar and Tropea (2002) indicate clearly that the splash created by a drop in a spray differs significantly from that of an isolated single drop impact or from the impact of a train of drops on a stationary liquid film, examined by Cossali et al. (1997) and Yarin and Weiss (1995).

These differences can be easily seen in the high-speed photographs in Figs. 3-1a and b, indicating that splash of a droplet in spray impact is much more irregular and non-symmetric in comparison to the symmetric propagation of a crown in the case of an isolated single droplet impact onto an undisturbed liquid layer.

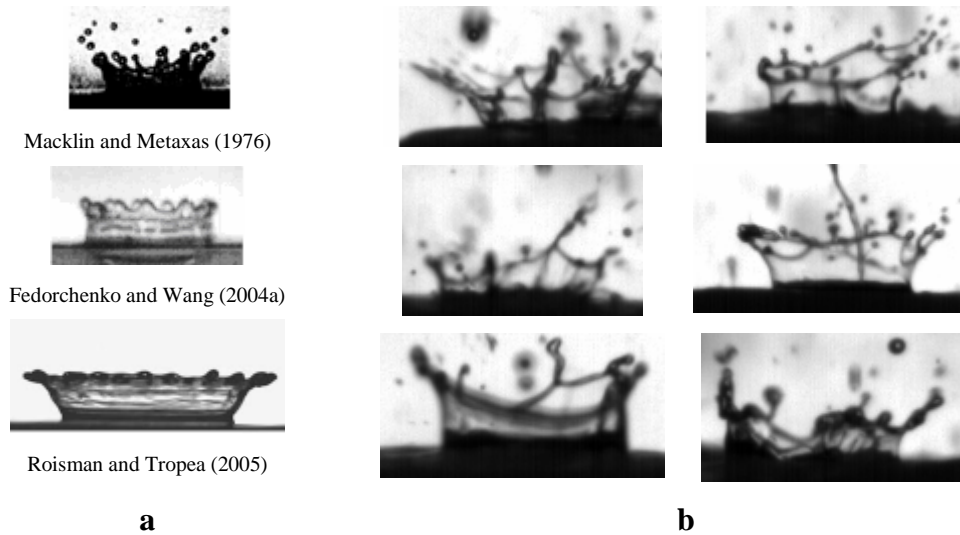


Fig. 3-1: Morphological comparison between splashes created by: a) an isolated single drop at various impact conditions, and b) by drops in a spray.

One exemplary sketch of a non-symmetric splash in a spray is illustrated in Fig. 3-2. As shown in this sketch, the main source for the non-symmetry of the splash is the impact of a neighbouring droplet during the splash. If during the splash of a given droplet in a spray, other droplets impact close to the splashing droplet, then the higher hydrodynamic pressure exerted in the film near the base of the crown will feed fluid into the crown body on one side, yielding a non-symmetric splash. The thickness of the crown body and the crown height on this side will be larger than on the other side, therefore secondary droplets ejected on this side will be larger due to the thicker rim bounding the crown. A similar behaviour can also be observed due to oblique impact of a droplet in spray. Such asymmetry splashing is also evident in Fig. 3-1b.

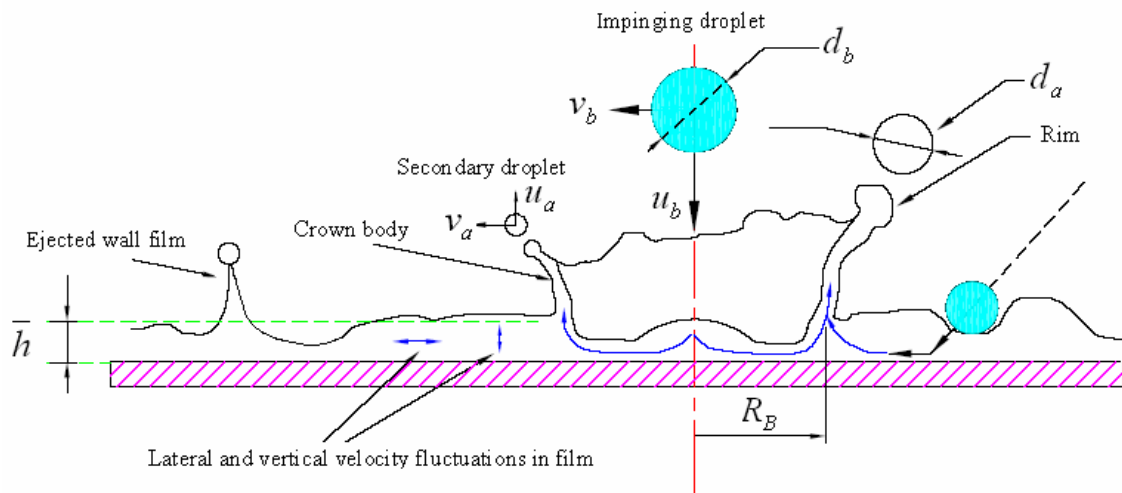


Fig. 3-2: Sketch of a non-symmetric splashing droplet in spray due to neighbourhood droplet(s) impact.

In the case of spray impact, the non-dimensional crown height and radius does not exhibit a systematic dependence on the impact Weber number, Sivakumar and Tropea, (2002). This is in contrast with the result of an isolated single droplet impact on a stationary liquid film examined by Cossali et al. (1999). Observations of Sivakumar and Tropea, (2002) indicate that in a spray impact the crown radius exhibits a growth rate proportional to $t^{0.2}$, significantly different than that of a single or train of single droplets impacting onto an undisturbed liquid layer, $\sim t^{0.5}$, as investigated theoretically by Yarin and Weiss (1995). In both cases the maximum crown heights are comparable, whereas the maximum crown radius is much smaller in the case of splashing in a spray. Also the crown retraction is more rapid in a spray.

An exemplary image sequence of a splashing droplet in a spray is presented in Fig. 3-3. These sequential images were recorded by means of a high-speed camera with 16 kfps. In this picture a liquid droplet with impact Weber number of 534 splashes on a rigid surface in a dimensionless accumulated film thickness of $\bar{h}/d_b=0.57$, where d_b is the drop diameter before impact.

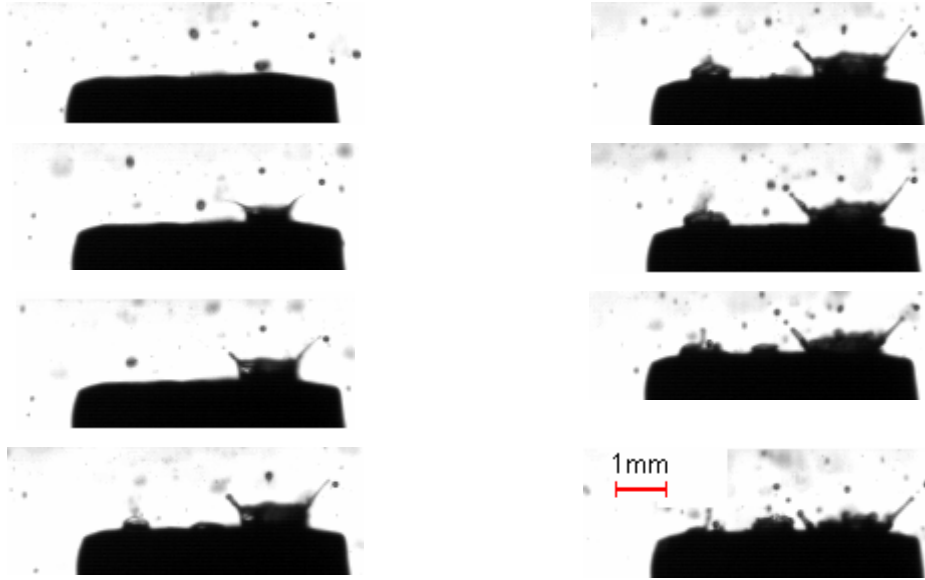


Fig. 3-3: Image sequence of a splashing droplet in a spray recorded with 16 kfps;
 $We_{nb} = 534$ and $\bar{h}/d_b = 0.57$.

In Figs.3.4a and b, the non-dimensional crown base radius ($R_B^* = R_B/d_b$) and height ($H_C^* = H_C/d_b$) are presented as a function of dimensionless time ($t^* = t \cdot u_b/d_b$) for the splashing droplet sequences illustrated in Fig. 3-3. In these pictures, non-dimensional crown base radius and height have a growth rate proportional to $(t^* - 0.1)^{0.3}$ and $(t^* - 0.5)^{0.28}$, respectively.

Based on the numerous measurements conducted in this study, the non-dimensional crown base radius and height of a splashing droplet in a spray as a function of dimensionless time can be expressed in the following forms

$$R_B^* \sim (t^* - \tau_R)^{n_R} \quad (3.1)$$

$$\text{where } 0.1 \leq \tau_R \leq 2.5 \quad \text{and} \quad 0.2 \leq n_R \leq 0.32$$

$$H_C^* \sim (t^* - \tau_H)^{n_H} \quad (3.2)$$

$$\text{where } 0.5 \leq \tau_H \leq 3.5 \quad \text{and} \quad 0.25 \leq n_H \leq 0.5$$

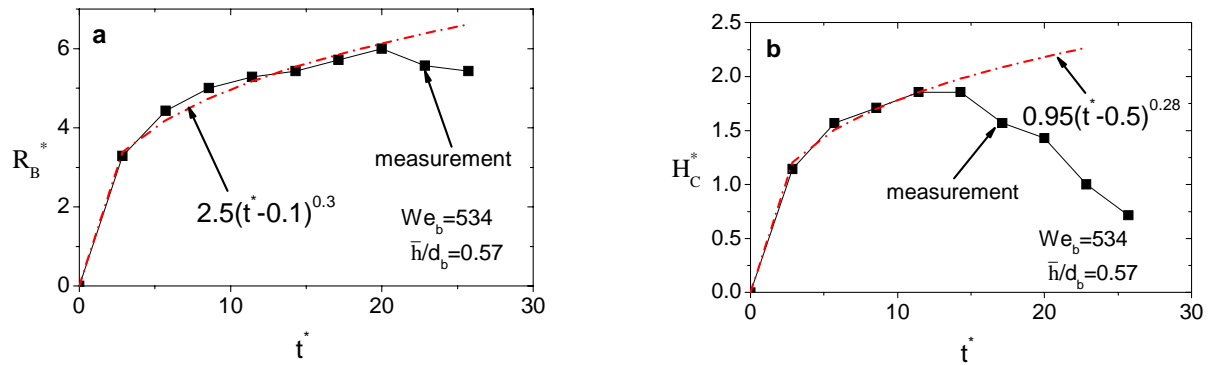


Fig. 3-4: Instantaneous variation of: a) crown radius and b) crown height with dimensionless time ($t^* = t \cdot u_b / d_b$); $We_{nb} = 534$ and $\bar{h}/d_b = 0.57$.

The difference of crown behaviour in a spray compared to single drop impacts has been examined by Roisman and Tropea (2004) in which the temporal spreading of the crown has been described using a model for short-wave fluctuations in the liquid film. Agreement with the experimental observations of Sivakumar and Tropea (2002) is very good. They have correlated their results for R_B^* with an exponent $n_R = 0.2$, which falls within the range given in expression 3.1.

Physically the influence of neighboring drop impacts on the crown development in a spray can be attributed to the wavy and non-steady liquid film interface; the curvature of the air-liquid film leading to local Laplace pressure and the high local pressure gradients due to the impacting drops.

While some of these effects have been previously investigated in isolation, see e.g. Roisman et al. (2002), the overall behaviour in a spray may involve a combination of effects. Therefore, data from impacting sprays and not just from single drop impacts are indispensable for formulating and verifying models. This is also the main purpose of the present work. The models in this study have been formulated on the basis of average quantities before and after impact (e.g. mean drop diameter, velocity and trajectory), i.e. results from single drop impacts are not used as a basis for the model formulation, as has been done in many previous modelling efforts.

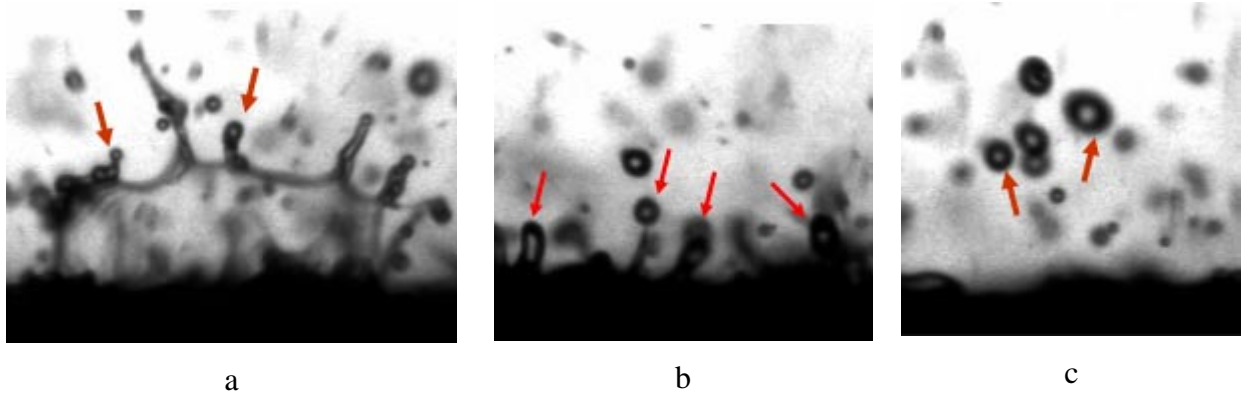


Fig. 3-5: Different sources for generation of secondary droplets and formation of liquid film on the wall, secondary droplet ejected from: (a) splashing droplet; (b) ejected wall film; (c) rebounded droplet.

Figure 3.5 illustrates the origins of secondary droplets: from a splash with disintegrating crowns, from liquid jetting from the liquid film, or from rebounding droplets. Especially for inertial dominated dense sprays, multiple finger-like jets ejected from the film are observed and first analyses have been presented by Roisman and Tropea (2005) to estimate their frequency and size.

Based on the previous studies, droplets can rebound for relatively low impact energy of the primary droplets. A necessary condition for a droplet rebounding from the wall is that the surface energy at the end of spreading must be larger than the dissipation during recoiling plus the kinetic and surface energy of the rebounded drop. Threshold criteria is given by Bai and Gossman (1995) for “Rebound-deposition” as $We_{nb} = 5$ ($We_{nb} = \rho u_b^2 d_b / \sigma$, where u_b is the normal velocity component before impact, and σ is the surface tension) based on the result of an isolated single drop impact, or $We_{nb} = 20$ for spray impact conditions based on the observation of Lee and Hanratty (1988) and Ching et al. (1984). Also the work of Wang and Watkins (1993) shows that rebound occurs only for $We_{nb} < 30$. Drop rebound is also observed for oblique impacts, whereby the threshold criterion is generally considered still valid if only the normal component of velocity is used in computed the impact Weber number, Sikalo et al. (2005). Especially the effect of impact obliqueness will be considered in the present study. Indeed, the Weber number ratio (We_{ib} / We_{nb}) will be shown to be a convenient parameter

in which to base a threshold for rebounding ($We_{tb} = \rho v_b^2 d_b / \sigma$, where v_b is the tangential velocity component before impact). An exemplary sequence of a rebound within a spray impact is illustrated in Fig. 3-6. In this picture, the impact Weber number based on the normal velocity component is 10; the impingement angle is 58° and the diameter of the impinging droplet does not change throughout the impact, i.e., $d_b \cong d_a$ (b- before, a- after impact).

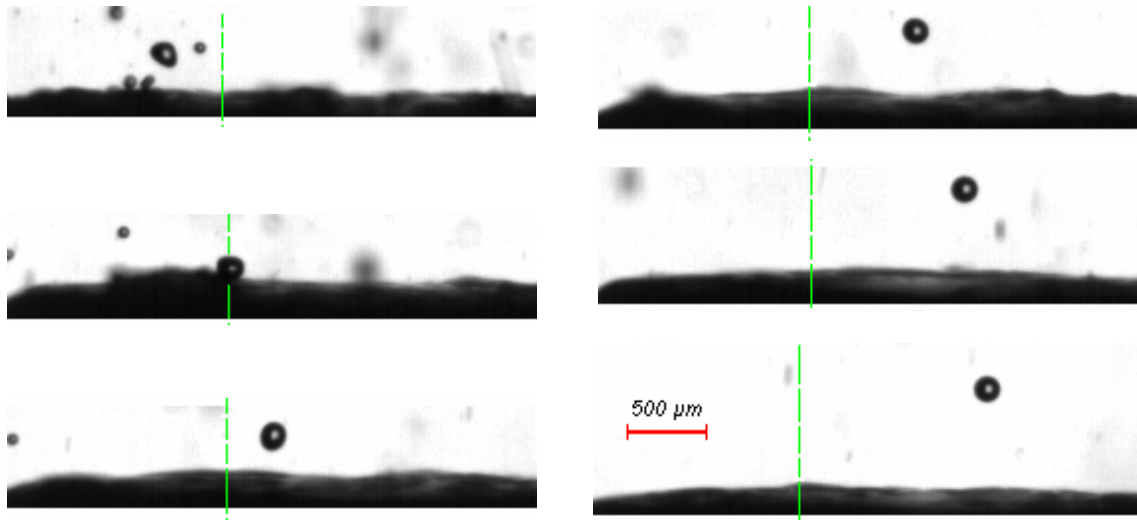


Fig. 3-6: Exemplary sequence of a rebound in a spray impact phenomenon; $d_b \cong d_a = 172 \mu\text{m}$, $We_{nb} = 10$, time interval between frames is 0.55 ms.

Splashing occurs at higher values of the normal impact Weber number, $We_{nb} > 80$ and it appears that the tangential velocity component does not play any important role in the onset of splashing. Observation of Coghe et al. (1999) shows that each splashing drop generates at least 10 tiny droplets.

The overall structure of the accumulated wall film consists of deposited droplets and partial deposition of splashing droplets. Droplets deposit on the wall when the impact energy (i.e., $We_{nb} < 2$) is extremely low. Partial deposition occurs also at higher impact Weber numbers, $30 < We_{nb} < 80$, when portions of the spreading droplet lose their kinetic energy due to dissipation. The upper limit of impact Weber number for deposition of a droplet without splashing also depends on the some additional parameters such as surface roughness and average depth of accumulated liquid film on the wall, e.g.

splashing takes place faster for rough surfaces as postulated by Mundo et al. (1998). Also it is shown by Cossali et al. (1997) that in the case of a single drop impact onto a stationary liquid film, the number of secondary droplets decreases as the depth of liquid layer is increased. Therefore, the ratio of average wall roughness to the average primary droplet size ($\bar{\varepsilon}^* = \bar{\varepsilon}/d_b$, where $\bar{\varepsilon}$ is the average of roughness of the target surface) should be considered if rough or structured surfaces are used. In the case of an accumulated wall film, the ratio of the average liquid film thickness accumulated on the wall to the average primary droplet size ($\bar{h}^* = \bar{h}/d_b$, where \bar{h} is the average film thickness) should be considered. For smooth surfaces, the upper limit for deposition-splashing is expressed using a K -factor ($K = We \cdot Oh^{-0.4}$). This limiting criterion can be also taken from an Oh - Re diagram, see e.g. Mundo et al. (1997). Other splashing parameters, $K = f(\bar{h}^*)$ have been introduced for thin liquid film conditions, e.g. $K_{Cr} = 2100 + 5880 \cdot \bar{h}^{*1.44}$, see Cossali et al. (1997). Furthermore it seems that the velocity fluctuations inside the accumulated wall film have an influence on the splashing phenomenon.

Rioboo et al. (2003) investigated the experimental threshold conditions for the crown formation due to a single drop impact onto a very thin liquid film in the range $0.004 \leq h_0^* \leq 0.189$. In their experiments Weber number, Reynolds number and the dimensionless film thickness were changed by using four different liquids and different impact and wall film conditions. Based on the results obtained by Rioboo et al. (2003), the threshold Weber or K - number is constant for $0.05 \leq h_0^* \leq 0.1$.

In Table 3-1, four different liquid film regimes are classified based on a threshold K -number (K_{th}) required for the onset of splashing. The value of K - number required for the onset of splashing is constant for the case of $\bar{h}^* \leq 0.1$ (wetted wall) as proposed by Schmehl et al. (1999) and Rioboo et al. (2003). The threshold Weber number then increases monotonically with an increase of the dimensionless film thickness up to $\bar{h}^* = 1$ (thin liquid film) and then decreases until $\bar{h}^* = 2$ (shallow liquid film) and finally takes an asymptotic value corresponding to a deep liquid layer (deep pool condition). The boundary value $\bar{h}^* = 2$ is already considered by Macklin and Metaxas (1976) for

shallow-deep liquid film condition. This classification has been postulated based on the measurement data obtained by Wang and Chen, (2002).

Table 3-1: Classification of film thickness formed on the wall due to spray impact based on experimental data from Wang and Chen, (2002).

Dimensionless film thickness (\bar{h}^*)	Wall film condition	Variation of K_{th}	K_{th} correlation (for 70% gly/water droplets)
$\bar{h}^* \leq 0.1$	wetted wall	constant	$\sim 1770-1840$
$0.1 < \bar{h}^* \leq 1$	thin liquid film	increasing	$5032\bar{h}^* + 1304$
$1 < \bar{h}^* \leq 2$	shallow liquid film	decreasing	$\sim 6100\bar{h}^{*-0.54}$
$\bar{h}^* > 2$	deep liquid layer	constant (asymptotic value)	~ 4050

For the deep film condition (i.e. $\bar{h}^* > 2$), the inertia dominated impacting droplet creates a crater in the liquid film leading to bubble entrainment inside the film and formation of an uprising central jet. This phenomenon is well known and described in the case of a single droplet impact onto a stationary deep liquid layer by Ogüz and Prosperetti (1990) or Fedorchenko and Wang (2004).

Fedorchenko and Wang (2004) have used the dimensionless capillary length ($l_c^* = [2\sigma/(\rho g)]^{1/2} / d_b$) to define two asymptotic conditions describing the central jet phenomenon, as summarized in Table 3-2. In this Table, R_{max}^* , h_{jet}^* , d_{jet}^* and u_{cj}^* denote respectively the dimensionless maximum cavity radius and height and the diameter and velocity of the uprising central jet created after the cavity recedes,. Each parameter is normalized using the drop size or velocity before impact (i.e., $h_{jet}^* = h_{jet}/d_b$ or $u_{cj}^* = u_{cj}/u_b$ or $u_{cj}^* = u_{cj}/u_0$). In the case of a normal single droplet with a relative small impact velocity,

the first condition ($l_c^* \ll 1$) applies, whereas the second condition ($l_c^* \gg 1$) is mostly important for spray impact phenomena. Results presented in Table 3-2 indicate that gravity does not play an important role in the formation and dynamics of uprising central jets in the case of $l_c^* \gg 1$. The coefficient C_l in Table 3-2 is given by Fedorchenko and Wang (2004) as 2.75. In the conducted experiments used in this study, l_c^* varies in the range $80 \leq l_c^* \leq 180$.

Table 3-2: Asymptotic values for characterization of cavity and uprising central jet.

Non-dimensional capillary length	$l_c^* \ll 1$	$l_c^* \gg 1$
R_{\max}^*	$(Fr/3)^{1/4}$	≈ 1
h_{jet}^*	$1.43Fr^{1/4}$	$\approx 3/8$
d_{jet}^*	$0.57Fr^{1/4}$	$\approx 8/3$
u_{cj}^*	$0.913c_1 \cdot Fr^{-3/8}$	$1.618c_1 \cdot We^{-1/2}$

The foregoing survey of literature and phenomenological characterization of spray impact leads us to two fundamental conclusions: Modelling spray impact must consider also the presence and influence of the accumulated wall film; Models based solely on the impact of single droplets will miss many essential elements of spray impact (a summary of previous models for single drop and spray impact is given in Appendix 1). These conclusions are motivation to formulate models derived from spray impact data obtained under a large selection of controlled boundary conditions; hence also the motivation to perform such experiments.

3.2. Experimental Set-up

The experimental arrangement used in this work is pictured in Fig. 3-7. The spray was created using two different hollow-cone (pressure swirl) nozzles from Delevan and two different full-cone nozzles from Spraying System Co., operated at pressures between 3 and 7 bars. The chosen hollow-cone nozzles produce a spray angle of about

70° at a flow rate of 1 or 1.5 l/h. Both flow rate and pressure were variable and measured. The targets were also varied, using the end face of a steel cylinder (D=5 and 15mm diameter) and a 94mm diameter steel sphere. This target boundary condition affects the accumulation of the liquid film on the target.

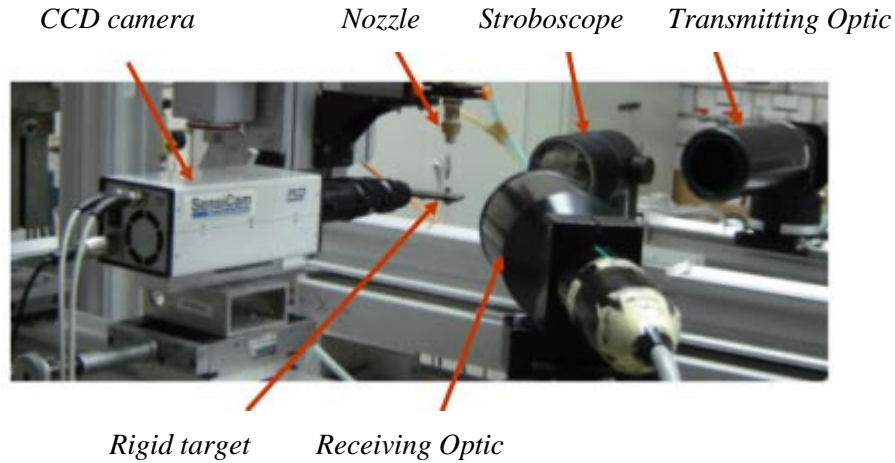


Fig. 3-7: Photograph of the experimental set-up for spray impact studies (Showing the CCD camera and the phase Doppler measurement system).

The nozzles were placed at ($x_{nozzle} = -15, -20, -30, -40$ and -50 mm) above the target and varied in displacement from the target central axis on the target diameter. The coordinate system used for the measurement grid is shown in Fig. 3-8.

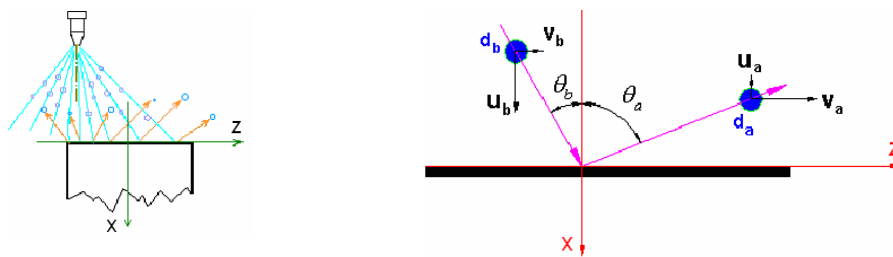


Fig. 3-8: Coordinate system and nomenclature for impinging and ejecting droplets.

To characterise the spray a dual-mode phase Doppler instrument from Dantec Dynamics was used, comprising a transmitting optics with a 400mm focal length, a receiving optics with a 310mm focal length, an “A” type mask and a 34° scattering angle.

By using a dual-mode configuration both normal and tangential velocity components of each individual droplet and its diameter were measured 1mm above each target (i.e., $x = -1\text{mm}$) based on the target diameter. The ingoing and outgoing droplets are distinguished using the sign of the velocity component normal to the target, i.e. positive u denotes an impacting droplet and a negative u denotes a secondary droplet. The overall size distributions were corrected for the size dependent detection volume cross-section using the standard system software. Further details of the optical system, alignment and calibration, and signal and data processing can be found in chapter 2.

The thickness of the liquid film created under spray impact has been estimated based on multiple images obtained by a Sensicam CCD camera (Fig. 3-7). Another high-speed CMOS camera with 32000 *fps* has been used to follow the deposited or ejected droplets from the wall, as already shown for two exemplary cases in Figs. 3-3 and 3-6.

Surface roughness of the rigid targets has been characterized by means of a mechanical profile meter from Hommelwerke Co., type TK300. Mean roughness (R_a or $\bar{\varepsilon}$) of the target surfaces used in this study ($R_a = \frac{1}{lr} \int_0^{lr} |x(z)| dz$, where lr is the measured length on the target surface) varied in the range $0.2 \mu\text{m} < R_a < 0.67 \mu\text{m}$, whereas mean peak-to-valley roughness (R_z) of the used targets varied in the range $1.3 \mu\text{m} < R_z < 6.6 \mu\text{m}$ ($R_z = \frac{1}{N} \sum_{i=1}^N x t_i$, where N is number of the measured points on the target surface), see Fig. 3-9a and b. In this study, the relative surface roughness in comparison to the mean measured drop size or average accumulated wall film thickness was negligible, see Table 3-5.

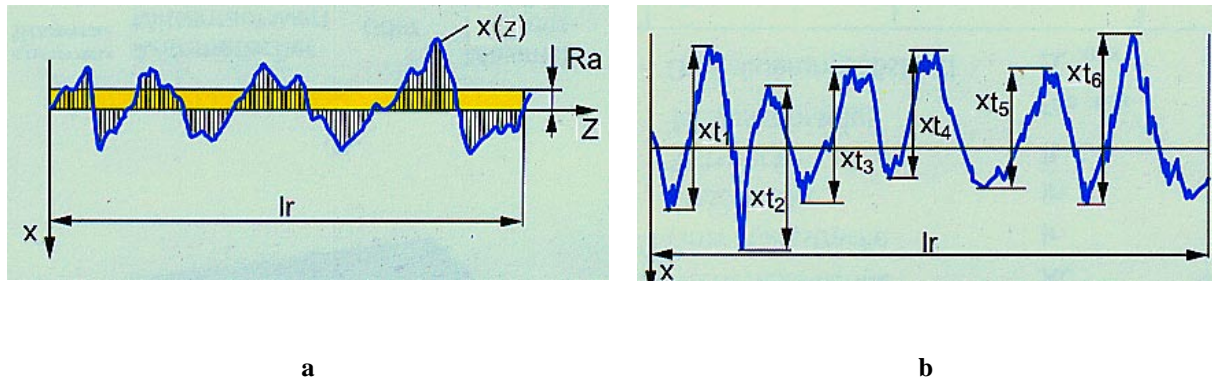


Fig. 3-9: a) Mean roughness (R_a or $\bar{\varepsilon}$), and b) mean peak-to-valley roughness (R_z) of the target surface.

3.2.1. Number of required samples at each grid point for a statistically reliable measurement

The number of measured drops at each measurement point was chosen to insure a specified statistical uncertainty of the computed mean quantities.

Assuming statistical independence of all drops, the variance in estimating the mean of a quantity φ is given by

$$\sigma_{\varphi}^2 = \frac{\sigma_{\varphi}^2}{N} \quad (3.3)$$

where σ_{φ}^2 is the variance of φ itself and N is the number of samples. In normalized form this yields

$$\varepsilon^2 = \frac{\sigma_{\varphi}^2}{\bar{\varphi}^2} = \frac{1}{N} \frac{\sigma_{\varphi}^2}{\bar{\varphi}^2} \quad (3.3b)$$

Specifying ε^2 , N was chosen using values of σ_{φ}^2 and $\bar{\varphi}$ obtained from preliminary measurements. Typical values for the quantities u_b , v_b , and d_b are shown in Table 3-3, as well as the resulting N values for $\varepsilon^2 = 5\%$ and 1% . For final measurements always the maximum value of N was used. In the example measurement position shown in Table 3-3, the variance of the mean tangential velocity was the highest.

For some case, the mean tangential velocity \bar{v} approaches zero, in which case the normalized uncertainty (Eq. 3.3b) is not suitable. In such case the maximum of the computed samples from u_b and d_b was used.

Table 3-3: Summary of the average measured quantities at a single measurement point, and the minimum number of required samples computed by (3.3) at the level of 5% and 1%.

Measured quantity	u_b (m/s)	v_b (m/s)	d_b (μm)
Mean ($\bar{\varphi}$)	8.92	-3.1	22.4
STD ($\sigma(\varphi)$)	4.23	2.34	15.84
Var. ($\sigma^2(\varphi)$)	17.92	5.49	250.9
N ($\varepsilon = 5\%$)	90	229	200
N ($\varepsilon = 1\%$)	2252	5713	5002

3.2.2. Effect of target position

Two exemplary single-point measurements of drop diameter count with and without the target at the centreline of the target are presented in Fig. 3-10, which illustrate the effect of target position on the probability density distribution of the measured primary droplet sizes. In the first case, a 5mm cylindrical target was placed at the centerline of the spray, 20mm under the nozzle exit (Fig. 3-10a). In the second case (Fig. 3-10b), the measurement position is moved 15 mm off-axis. These two measurements differ significantly, indicating clearly the influence of the carrier flow on the measured drop size number density distribution.

The implications at these observations are numerous. It implies for instance that any numerical simulation of the spray impact must also capture the carrier flow and the drop slip velocities correctly. Furthermore, it implies that verification between experiments and simulations must be carried out at the some position relative to the target, an issue which has been addressed in more detail in chapter 2.

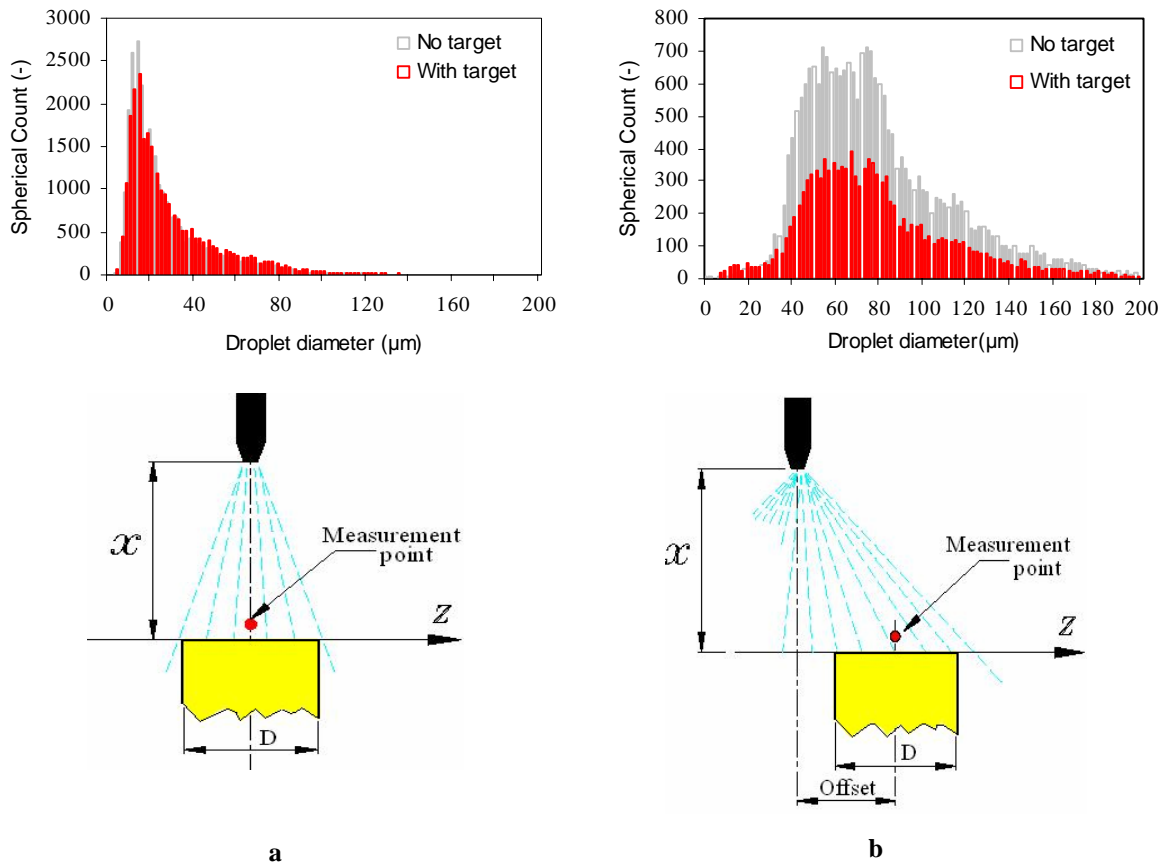


Fig. 3-10: Two exemplary single-point measurements of primary droplet count with and without target at 20mm under nozzle exit: (a) on the spray axis: $z=0$, and (b) off-axis: $z=15$ mm, measured 1 mm above the target.

3.3. Results and discussion

The goal of the present chapter is to formulate an empirical model of spray impact, taking into account the most influential governing factors, in particular the influence of the liquid film. Measurement data has been considered for a wide range of impact parameters and boundary conditions; while it is not feasible to present all of the measurement data, the correlations presented will be derived from the entire data set. Therefore in the following sections exemplary measurements of the different spray characterizing quantities will be presented in order to illustrate the origins of the model formulations.

Note that results presented in this study are completely independent of which spray nozzle is used. The data used to derive the correlations pictured in many of the diagrams, are all obtained from single positions above the surface.

Typically, single points in the presented diagrams in this chapter represent averages over 7000 to 20000 individual impacting and ejecting droplets on the target surface as discussed in section 3.2.1. Other points are taken at different positions on the target or for different spray operating conditions. For each measurement point, velocity, size and number of impacting and ejecting droplets during some given acquisition time are obtained. Therefore, the correlations are completely independent of the nozzle generating the spray.

Indirectly, if other spray nozzles are used, then other impacting size distributions or densities are obtained, but these factors have been included to some extent in the correlations (within the stated bounds) by examining different spray impact positions on the target or operating the spray nozzle at different conditions (pressure, distance to the target, etc.).

Summary of the measured range of quantities for before and after impact is given in Table 3-4.

Table 3-4: Summary of the measured range of quantities.

Measured quantity	Unit(SI)	Before impact	After impact
Droplet size (mean)	μm	21-47	24.5-50
u-velocity	m/s	0.5-15.5	0.5-3.1
v-velocity	m/s	0.05-4.8	0.2-4.15
Weber	-	2-167	6.5-13
Reynolds	-	10-560	12-180
Droplet angle(θ)	($^{\circ}$)	1-70	42-82
Average film thickness (\bar{h})	μm	-	8-107
Mean roughness (R_a)	μm	0.2-067	-
Mean peak-to-valley roughness (R_z)	μm	1.3-6.6	-

3.3.1. Distribution of droplet size

Some typical measurement results of drop size distributions are presented in Fig. 3-11, in which the probability density distributions for the primary and secondary droplet sizes are shown for four measurement points. These points differ significantly in the computed local ejected mass fraction, given as λ_m ($\lambda_m = \dot{m}_a / \dot{m}_b$, ejected mass to impinging mass). This particular comparison has been chosen to illustrate that the number density of ejected drops can be higher for a lower mean Weber number of the impacting droplets, but that the ratio $\lambda_{Web} = We_{tb} / We_{nb}$ is also very influential, Figs. 3-11a and b correspond to normal impact conditions ($\lambda_{Web} < 0.1$), whereas Figs. 3-11c and d illustrate results for oblique impact conditions ($\lambda_{Web} \geq 0.1$), as will be discussed in more detail in section 3.3.5.

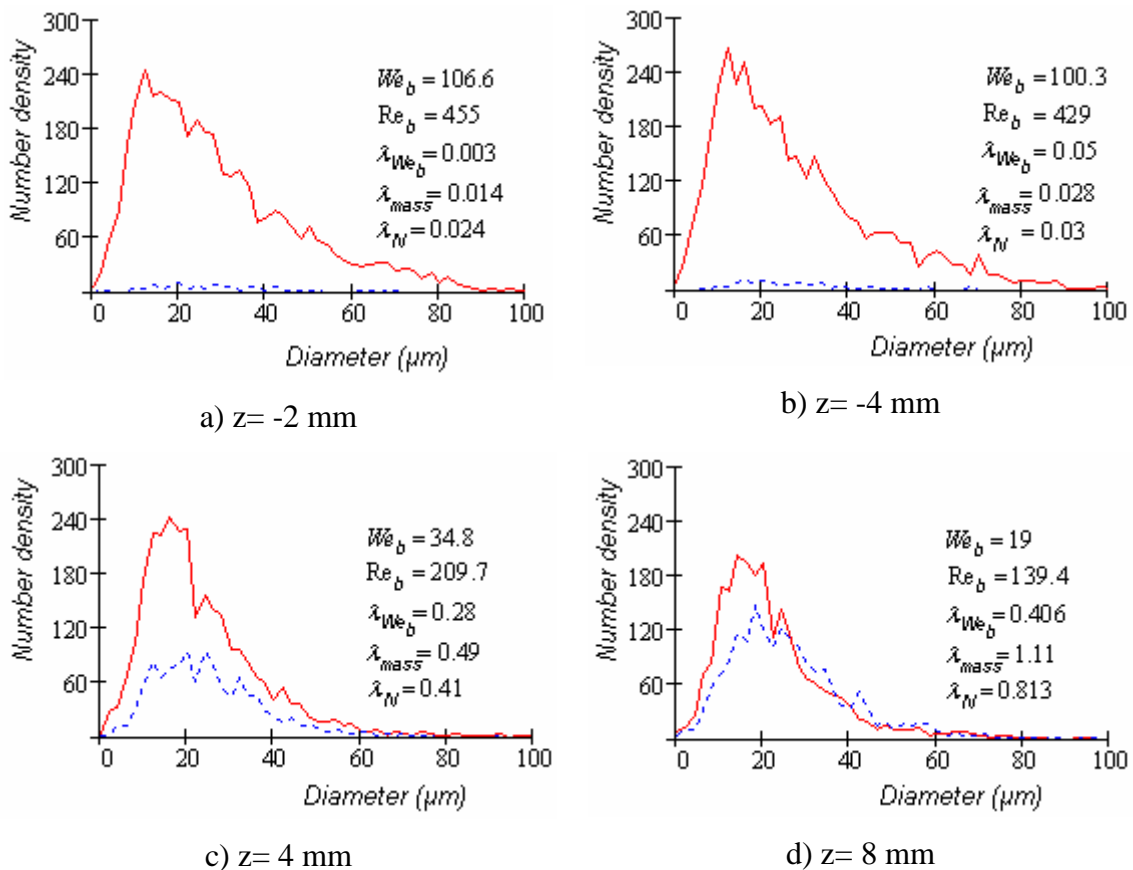


Fig. 3-11: Number density distribution of primary and secondary droplet sizes for four measurement points, measured 1 mm above the wall ($x = -1$); solid line: before impact, dashed line: after impact.

A further result in Fig. 3-12a shows that the average secondary droplet size (d_{10a}) increases slightly with increasing impact droplet size. The average drop size ratio (secondary to impacting drop size) falls within the fairly narrow range $0.8 < \lambda_{d10} < 1.2$ over all measurement positions and operating conditions as indicated in Fig. 3-12b. This ratio consistently decreases with increasing Weber number (We_{nb}) based on the normal component of velocity before the impact. A linear correlation can be used to describe this dependency, as

$$\lambda_{d10} = d_{10a}/d_{10b} = -0.003 \cdot We_{nb} + 1.2 \quad (r=0.869) \quad (3.4)$$

Where d_{10a} and d_{10b} are the arithmetic mean droplet diameters of ejected droplets and impinging droplets respectively.

To examine the statistical reliability of the obtained correlation (3.4), the obtained correlation factor (r) is examined according to the method of Snedcore and Cockran (1989) and considering the degrees of freedom of the system, i.e., $df=n-1$; n being number of the measurements used to obtain the correlation. The minimum correlation factor from the table of Snedcore and Cockran (1989) is obtained as $r_{min}=0.393$, see Table 3-5. Since the obtained correlation factor for expression 3.4 is larger than the minimum required correlation factor, i.e., $r=0.869 > 0.393$, we can conclude that the obtained correlation (3.4) is statistically significant.

Table 3-5: Excerpt from the Table of Snedcore and Cockran (1989) for correlation factor test (r-test).

df =n-1	$\xi=5\%$	$\xi=1\%$
35	0.325	0.418
40	0.304	<u>r = 0.393</u>

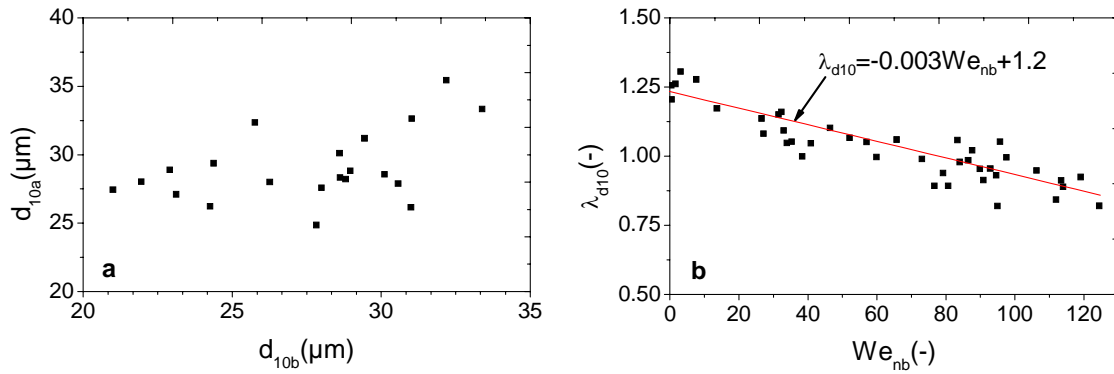


Fig. 3-12: a) Correlation between mean drop size before and after impact, and b) correlation for drop size ratio normal impact Weber number.

3.3.2. Distribution of velocity

In Fig. 3-13 the velocity of ejected droplets is compared with the velocity of the impacting droplets for each of the normal and tangential components for one specific spray condition, albeit very representative of other operational conditions. These velocities are shown as a function of measurement position above the target and for a single position of the nozzle. The results indicate clearly that the normal component of velocity for ejected droplets never exceeds about 3 m/s and this is valid for all experiments conducted in this study, despite the fact that the impingement velocity extended beyond 11 m/s. Perhaps even more interesting is that this magnitude is very poorly correlated with the normal component of impingement velocity (Fig. 3-13a). On the other hand the tangential component of ejection velocity behaves quite differently. Not only does the ejected magnitude sometimes exceed the impingement magnitude (e.g. $0 < z/D < 0.5$), the two are also very closely correlated with one another. Clearly the tangential momentum is conserved to a large extent upon impingement, whereas the normal momentum is dissipated or diverted into the tangential momentum. Any model describing the spray impingement must reflect such observations.

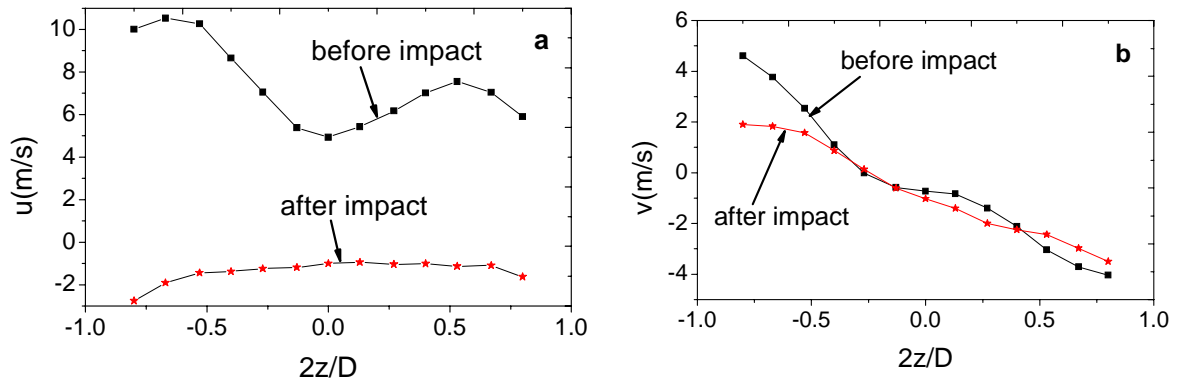


Fig. 3-13: Comparison of droplet velocity before and after impact for various positions of the measurement volume above the $D=15$ mm target: (a) normal component, and (b) tangential component; average film thickness $\bar{h} \approx 20$ μm .

The results show that the ratio of the normal component of velocity (u_a/u_b) decreases with increasing Weber number (We_{nb}) based on the normal component of velocity before the impact (Fig. 3-14a), but the ratio of tangential component of velocity (v_a/v_b) is independent of the impact Weber number (Fig. 3-14b). The ratio (u_a/u_b) falls in the range $0.15 < (u_{nb}/u_{na}) < 0.5$ for $We_{nb} > 10$. A general correlation for normal component of velocity can be written as

$$u_a / u_b = -1.1 \cdot (We_{nb})^{-0.36} \quad (r=0.65) \quad (3.5)$$

On the other hand, a linear correlation between the tangential component of velocities before and after impact was found for all measurement conditions as

$$v_a = 0.862 \cdot v_b - 0.094 \quad (r=0.93) \quad (3.6)$$

as illustrated in Fig. 3-14c.

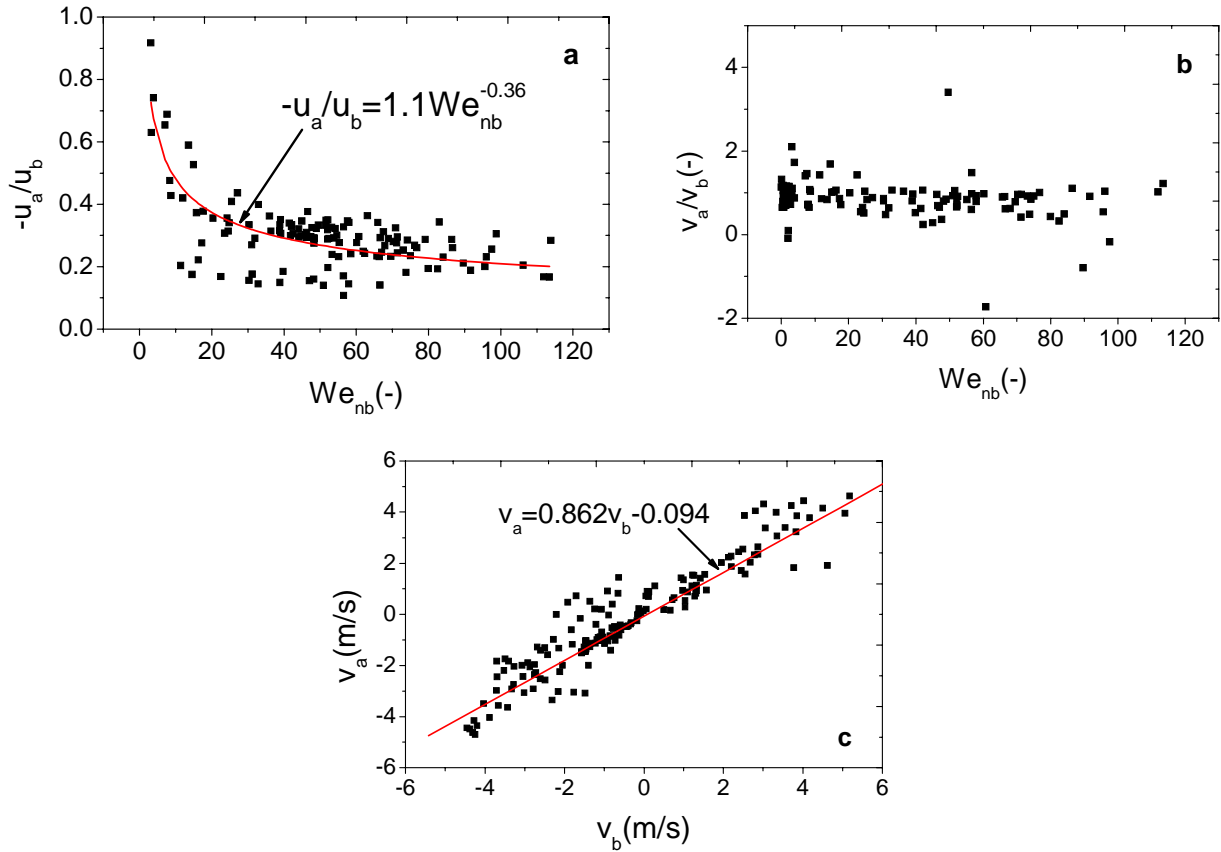


Fig. 3-14: Mean velocity ratio of ejected to impinging droplets as a function of impact Weber number: a) normal component, b) tangential component, and c) tangential component of after against before impact velocity.

3.3.3. Trajectory of secondary droplets (ejection angle of secondary droplets)

The ejection angle of the droplets depends strongly on the impingement angle, as shown in Fig. 3-15a. Definition of the ejection angle is given in chapter 2, see Eq. (2.20). A correlation of these results yields:

$$\theta_a [^\circ] = 0.623 \cdot \theta_b [^\circ] + 41^\circ \quad (r=0.80) \quad (3.7)$$

The correlation expressed in Eq.(3.7) indicates that the ejection angle of secondary droplets is on average much higher than that of primary droplets.

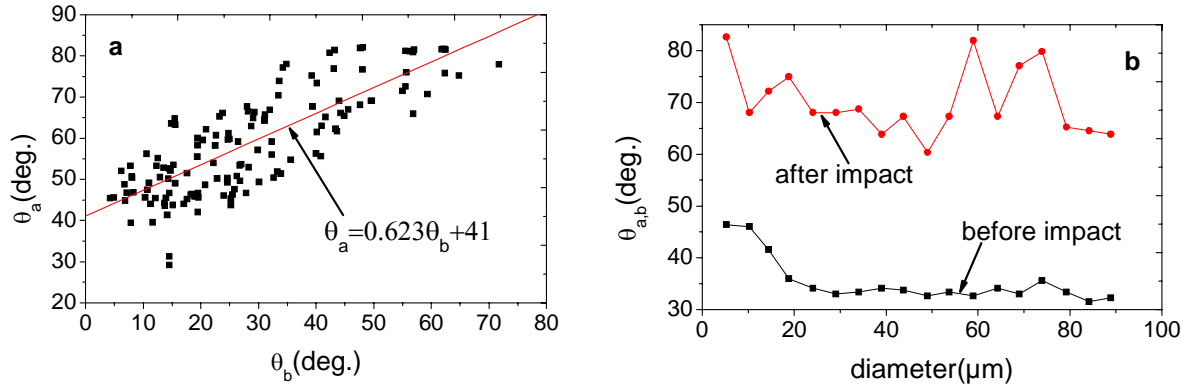


Fig. 3-15: a) Correlation between mean ejection angle and impingement angle of droplets, collected over all experiments; b) Impingement (θ_b) and ejection (θ_a) angle of droplets at a single measurement point and as a function of droplet diameter.

This is consistent with data presented in section 3.4.2 for the normal and tangential velocity components since

$$\theta_a = \tan^{-1}(v_a / u_a) \quad (3.8)$$

In non-dimensional terms the ejection angle dependence on impact Weber number can be expressed as

$$\eta = \tan \theta_a / \tan \theta_b = 0.784 We_{nb}^{0.36} \quad (3.9)$$

This functional dependence is illustrated in Fig. 3-16 and shows that the ejection angle of droplets is almost always larger than the impingement angle.

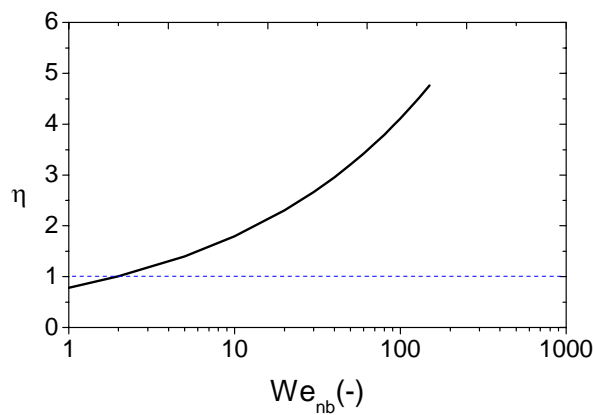


Fig. 3-16: Coefficient of ejection angle of secondary droplets.

Note, that if any one measurement point is examined in more detail, no significant dependence of ejection angle on droplet diameter can be observed, as exemplary shown in Fig. 3-15b. Only for very small droplets is a small increase in impingement and ejection angle observed (i.e., $d_b < 20\mu\text{m}$).

3.3.4. Distribution of the ejection Weber number

The previous results can also be examined in terms of Weber number before and after the impact, in this case computed using the velocity magnitude. Such a diagram is shown in Fig. 3-17, in which the Weber number of ejected droplets first increases with increasing impact Weber number, but then after reaching a maximum value, again decreases. In this representation three regimes can be identified: first a low impact Weber number range ($We_{nb} < 20$) in which the rebounded droplet increases with increasing the Weber number (region I in Fig. 3-17). This is followed by deposition range ($20 < We_{nb} < 80$), in which the deposition rate is high and fewer secondary drops are ejected (region II in Fig. 3-17), and finally at high Weber numbers $We_{nb} > 80$, a condition of splashing or ejected wall film, in which the secondary droplets ejected from splashed corona are small and also the velocities are small, leading to lower ejection Weber numbers (region III in Fig. 3-17). The Weber number 80 is often found in the literature as a limit for splash onset, see e.g., Bai and Gosman (1995).

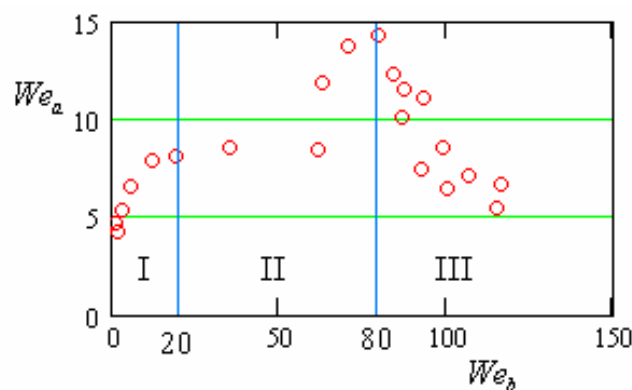


Fig. 3-17: Weber number of ejected droplets against impact Weber number.

At any single measurement point, the impact Weber number increases linearly with mean droplet diameter, whereas the ejected Weber number at first increases with diameter (up to $d_b \approx 20\mu\text{m}$) then does not change significantly or decreases, as illustrated in Figs. 3-18a and b.

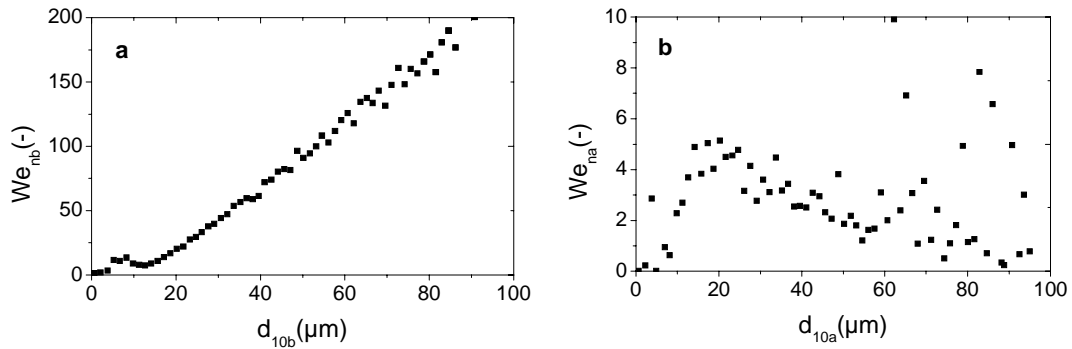


Fig. 3-18: Distribution of: a) impact, and b) ejection Weber numbers at a single measurement point above a spherical target.

Note that the computed Weber number in Fig. 3-18a and b depends also on the drop velocity, but however linear variation of the before impact Weber number with the mean drop size computed within the different size classes, indicates the Inter-correlation between drop size and drop velocity for impacting spray. Absence of such behavior for after impact spray indicates that no inter-correlation between drop size and drop velocity exist for secondary droplets, see Fig. 3-19.

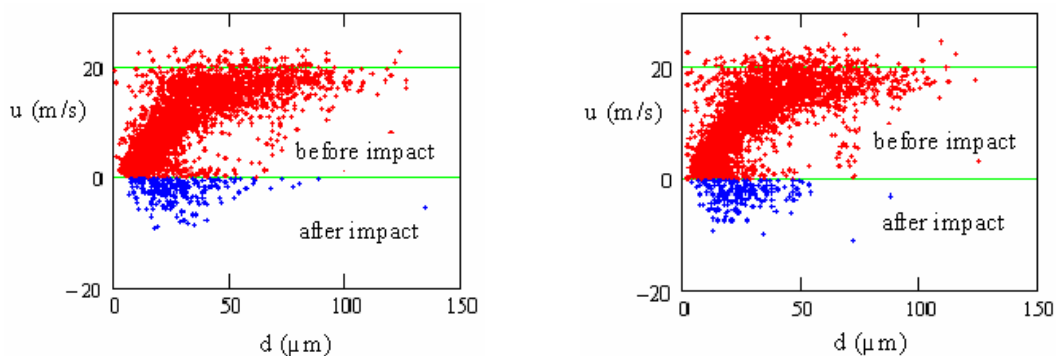


Fig. 3-19: Exemplary variation of the droplet velocity and droplet size for before impact ($u > 0$) and after impact ($u < 0$).

3.3.5. Distribution of secondary to incident mass and number ratios

The total local secondary-to-incident mass ratio ($\lambda_m = \dot{m}_a / \dot{m}_b$) is affected by several complex parameters such as droplet Weber number based on the normal component of impact velocity (We_{nb}), impact Weber number ratio (We_{ib}/We_{nb}), impact Reynolds numbers (Re_{nb}), relative wall roughness ($\bar{\varepsilon}^* = \bar{\varepsilon} / d_b$) and relative wall film thickness ($\bar{h}^* = \bar{h} / d_b$); hence a general correlation for mass ratio is difficult to derive. Generally, total local secondary-to-incident mass ratio ($\lambda_m = \dot{m}_a / \dot{m}_b$) can be expressed in dimensionless form as

$$\lambda_m = (\dot{m}_a / \dot{m}_b) = f \left(We_{nb}, \lambda_{We_b}, Re_b, \bar{\varepsilon}^*, \bar{h}^* \right) \quad (3.10)$$

The total local secondary-to-incident mass ratio ($\lambda_m = \dot{m}_a / \dot{m}_b$) in this study is computed by means of

$$\lambda_m = \frac{m_a}{m_b} = \frac{\sum_{i=1}^{N_a} (d_a^3)_i}{\sum_{j=1}^{N_b} (d_b^3)_j} \quad (3.11)$$

Note that these estimates of the mass or the mass flux ratios can be considered more accurate than estimates of the absolute mass flux values. The reason for this is that the summations given in Eqns. 3.11 and 3.12 do not account for drops not detected or validated by the phase Doppler system. The subsequent error in the numerator and denominator of expressions 3.11 and 3.12 will not exactly cancel, but assuming that the percentage of non-detected or non-validated drops is constant and that there exists no correlation between missed droplets and velocity sign, then the error in the ratio will be reduced.

Note that previous models have not considered any systematic dependencies of λ_m , for instance in the model of Bai and Gosman (1995) λ_m takes a random value in the range [0.2, 0.8] for spray impact onto a dry wall and [0.2, 1.1] for spray impact onto a wetted wall.

The result of present study shows that the Weber number ratio, We_{ib}/We_{nb} , which compares the ratio of the square of the tangential velocity to the normal velocity before impact, plays an important role in the spray-wall interaction phenomena. As an example, the mass and number ratios ($\lambda_m = \dot{m}_a/\dot{m}_b$, $\lambda_N = \dot{N}_a/\dot{N}_b$) correlate with this Weber number ratio much better than with the normal component of impact velocity in the Weber number (We_{nb}), at least for the oblique impact condition and relatively constant film thickness. To illustrate this, λ_N is plotted together with We_{nb} (Fig. 3-20a), and with $\lambda_{We_b} = We_{ib}/We_{nb}$ (Fig. 3-20b) for the same data set across the impact target. Note that the measurements in Fig. 3-20a and b are not symmetric and the nozzle was placed in an off-axis angle in compare to the target centreline. In this experiment, the impact obliqueness changes in the approximate range $0^\circ < \theta < 26^\circ$ over the z-positions shown in Figs. 3.20a and b. It can be seen that in the latter case the two quantities exhibit a very similar behaviour, indicating a strong correlation. This result indicates clearly that the spray-wall interaction models based on the results from normal drop impact alone cannot adequately describe the actual conditions of spray impact phenomena. The quantity λ_m behaves similarly.

Generally, in an oblique impact condition the secondary-to-incident mass ratio (λ_m) decreases with the impact Weber number based on the normal component of velocity (We_{nb}), but increases with the impact Weber number ratio (λ_{We_b}). In the case of a normal impact condition, the quantity λ_m increases with the impact Weber number based on the normal velocity component. Therefore two different impact conditions can be defined as:

Normal impact: $\lambda_{We_b} = We_{ib}/We_{nb} < 0.1$, for which no significant dependency between secondary-to-incident mass ratio (λ_m) and impact Weber number ratio (λ_{We_b}) was observed, Fig. 3-21a.

- Oblique impact: $\lambda_{We_b} = We_{ib}/We_{nb} \geq 0.1$, for which the secondary-to-incident mass ratio (λ_m) increases with impact Weber number ratio (λ_{We_b}), Fig. 3-21b.

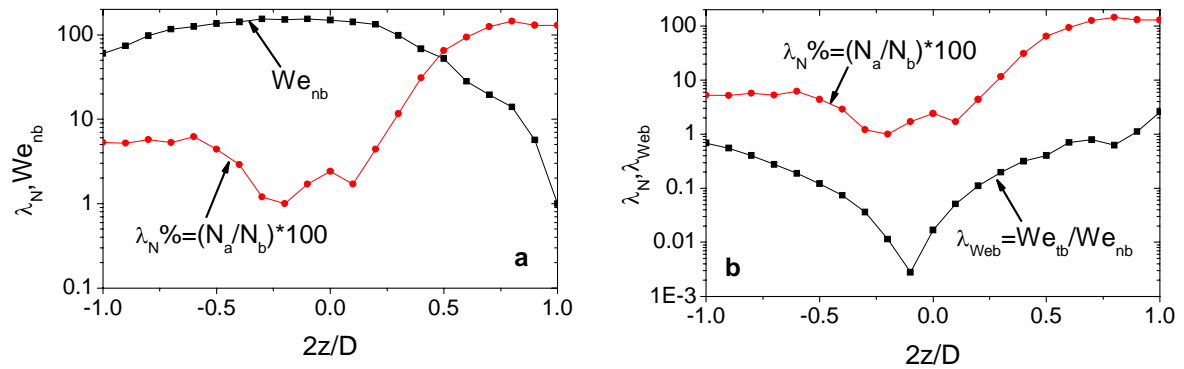


Fig. 3-20: Variation of number and Weber number ratio across the target: a) number ratio (λ_N) and Weber number based on the normal velocity component before impact (We_{nb}), and b) number ratio (λ_N) and Weber number ratio $\lambda_{Web} = We_{tb}/We_{nb}$.

In the case of normal impact ($\lambda_{We_b} < 0.1$), the secondary-to-incident mass ratio (λ_m) mostly falls in the range [0.002, 0.85], whereas this ratio falls in the range [0.016, 1.12] for oblique impact conditions ($\lambda_{We_b} \geq 0.1$). The upper limit of the mass ratio in the case of oblique impact (i.e., $\lambda_m = 1.12$) clearly indicates that for some conditions more liquid mass is ejected from the local wall film than impacts with the drops, this observation can be explained by the film flow on the wall from the local dense impacting region to the local measurement position or “by the flow from the dense spray regions to the detection volume, Roisman: private communication”.

For all of the conducted measurements, two limiting values, $\lambda_m > 1$ and $\lambda_m < 0.01$ were observed for oblique and normal impact conditions, respectively, see Figs.3.21a and b.

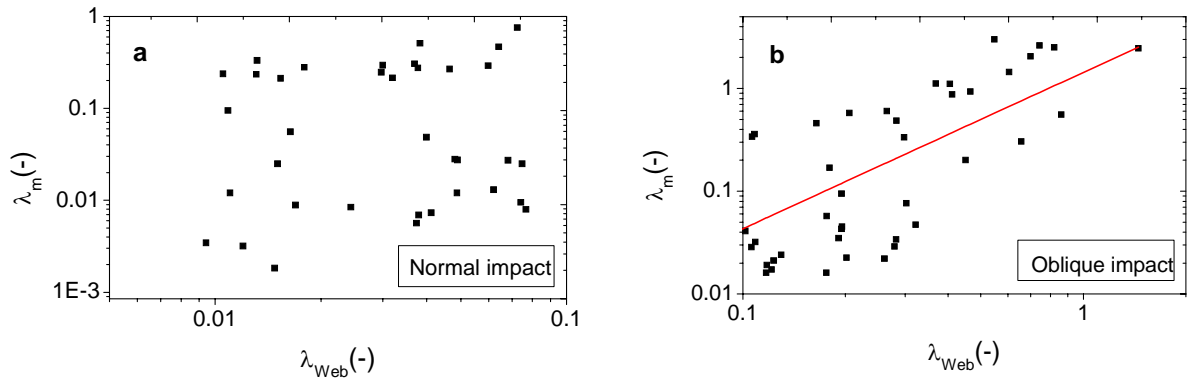


Fig. 3-21: Distribution of secondary-to-incident mass ratio (λ_m) for: (a) normal impact condition $\lambda_{We_b} < 0.1$, and (b) oblique impact condition $\lambda_{We_b} \geq 0.1$.

The results of this study indicate that in the case of normal impact conditions ($\lambda_{We_b} < 0.1$), the secondary-to-incident mass and number ratio, λ_m and λ_N , increase linearly with the impact Weber number based on the normal component of the impact velocity (We_{nb}).

$$\lambda_m = (\dot{m}_a / \dot{m}_b) = 6.74 \times 10^{-3} \cdot We_{nb} - 0.204 \quad (r=0.89) \quad (3.12)$$

$$\lambda_N = (\dot{N}_a / \dot{N}_b) = 2.16 \times 10^{-3} \cdot We_{nb} + 8.96 \times 10^{-2} \quad (r=0.64) \quad (3.13)$$

These correlations were derived using all conducted measurements in the range $35 \leq We_{nb} \leq 165$ and $\lambda_{We_b} < 0.08$, Figs. 3-22a and b.

The influence of the target diameter in the correlations (Eqs. 3.12 and 3.13) can be neglected if the dimensionless film thickness accumulated on the wall remains in the thin liquid film condition, i.e., $\bar{h}^* \leq 0.1$. In this case, the most influencing quantity on the total secondary-to-incident mass and number ratios will be the impact Weber number. More discussion about the influence of the average film thickness on the ejected mass is given in chapter 4, see e.g., Fig. 4-13.

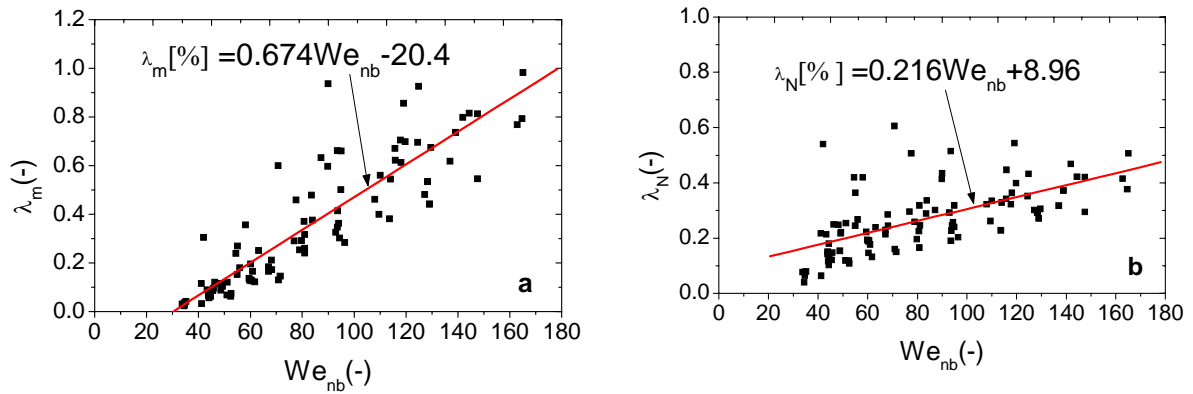


Fig. 3-22: Correlation of secondary-to-incident: a) mass ratio λ_m , and b) number ratio λ_N with impact Weber number based on the normal component of velocity We_{nb} for normal impact conditions $\lambda_{We_b} < 0.1$.

In the case of oblique impact conditions ($\lambda_{We_b} > 0.1$), the secondary-to-incident mass and number ratio (λ_m, λ_N) behave quite differently. These two quantities λ_m and λ_N decreases with the impact Weber number based on the normal component of the impact velocity (We_{nb}) and increases with the impact Weber number ratio (λ_{We_b}), see Fig. 3-21b and Figs. 2-23a and b. In contrast to the results presented in Figs. 3-22a and b for normal impact condition, larger secondary-to-incident mass and number ratios can be observed for smaller impact Weber numbers in the case of an oblique impact condition, as illustrated in Figs. 3-23a and b. This is due to a larger impact Weber number ratio (λ_{We_b}) at smaller impact Weber numbers (We_{nb}) in oblique impact condition, see also Fig. 3-21b. Note that in the case of oblique impact conditions, the impact Weber number ratio simultaneously increases with decreasing impact Weber number based on the normal component of impact velocity, see Fig. 3-21b. To better understand the oblique impact phenomena, a sketch of the oblique impact region is shown in Fig. 3-24c. It is found from the experiments that the impact Weber number decreases from point “A” to “C” in Fig. 3-24c, i.e., $(We_{nb})_A > (We_{nb})_B > (We_{nb})_C$, but the total secondary-to-incident mass ratio increases from point “A” to point “C”, i.e., $(\lambda_m)_A < (\lambda_m)_B < (\lambda_m)_C$ at a given atomizing pressure. This fact is due to the contribution of the impact Weber number ratio, which increases from point “A” to point

“C”, i.e., $(\lambda_{We_b})_A < (\lambda_{We_b})_B < (\lambda_{We_b})_C$. In the case of oblique impact conditions, two approximate correlations for mass and number ratio can be given as

$$\lambda_m = (\dot{m}_a / \dot{m}_b) = 35 \cdot We_{nb}^{-1.63} \quad (r=0.72) \quad (3.14)$$

$$\lambda_N = (\dot{N}_a / \dot{N}_b) = 7.1 \cdot We_{nb}^{-1.14} \quad (r=0.70) \quad (3.15)$$

Note that Fig. 3-20a clearly indicates that We_{nb} alone is not sufficient for describing oblique impacts. Fig. 3-20b indicates that the ratio $\lambda_{We_b} = We_{ib} / We_{nb}$ correlates better with the ejected mass fraction, but also this correlation is not outstanding. In any case both We_{nb} and λ_{We_b} exert an influence on the splashed mass fraction (at least for oblique impacts), i.e., $\lambda_m = f(We_{nb}, \lambda_{We_b})$, and these two parameters are coupled, i.e., they are not independent.

It would be presumptuous to think that we have sufficient data and insight of the physical process to try and develop a model which accounts for these rather complicated dependencies. As an alternative, we have partitioned our model into ‘normal’ impacts ($\lambda_{We_b} = We_{ib} / We_{nb} < 0.1$) and oblique impacts ($\lambda_{We_b} = We_{ib} / We_{nb} \geq 0.1$). For oblique impacts we investigated the correlation with both We_{nb} (Fig. 3-22a) and λ_{We_b} (Fig. 3-21b) but finally used the correlations with We_{nb} because this exhibited a higher correlation coefficient. This may appear too arbitrary, on the other hand, most present models simply use a random number to generate splash mass fraction according to the impact K-number ($K = Oh \cdot Re^{1.25}$), e.g. Bai and Gosman (1995).

Note that in the case of a normal impact condition, i.e., $\lambda_{We_b} = We_{ib} / We_{nb} < 0.1$, the prediction of the ejected mass and number flux of secondary droplets is much simpler, since they are independent of the impact Weber number ratio (λ_{We_b}), see Fig. 3-21a. In this case, the total secondary-to-incident mass ratio (λ_m) increases with the impact Weber number based on the normal component of velocity (We_{nb}). The major problem remains with the oblique impact condition. However, this is felt to be a rather large step forward in modeling spray impact, since no previous model considers these aspects.

A sketch for the region of applicability of the obtained correlations for mass and number ratio for both normal and oblique impact regions is illustrated in Fig. 3-24.

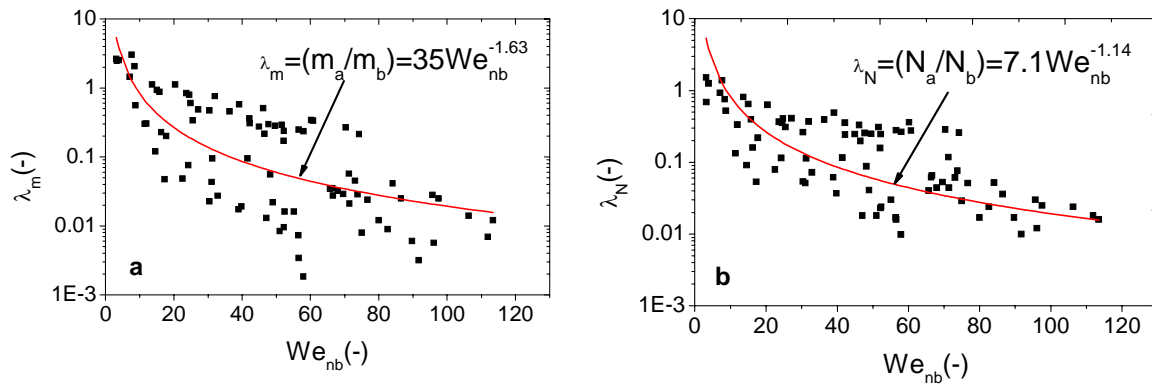


Fig. 3-23: a) Correlation of secondary-to-incident: mass ratio λ_m and number ratio λ_N , and b) with impact Weber number based on the normal component of velocity We_{nb} for oblique impact condition $\lambda_{We_b} > 0.1$.

These expressions (Eqns. 3.14 and 3.15) were derived using all conducted measurements in the range $10 < We_b < 160$ and $0.1 < \lambda_{We_b} < 0.86$ which are pictured in Figs. 3-23a and b. These expressions are valid for smooth target surfaces, i.e., $\bar{\varepsilon}^* = \bar{\varepsilon}/d_b \ll 1$. The average thickness of accumulated wall film for these measurements is described in the following section.

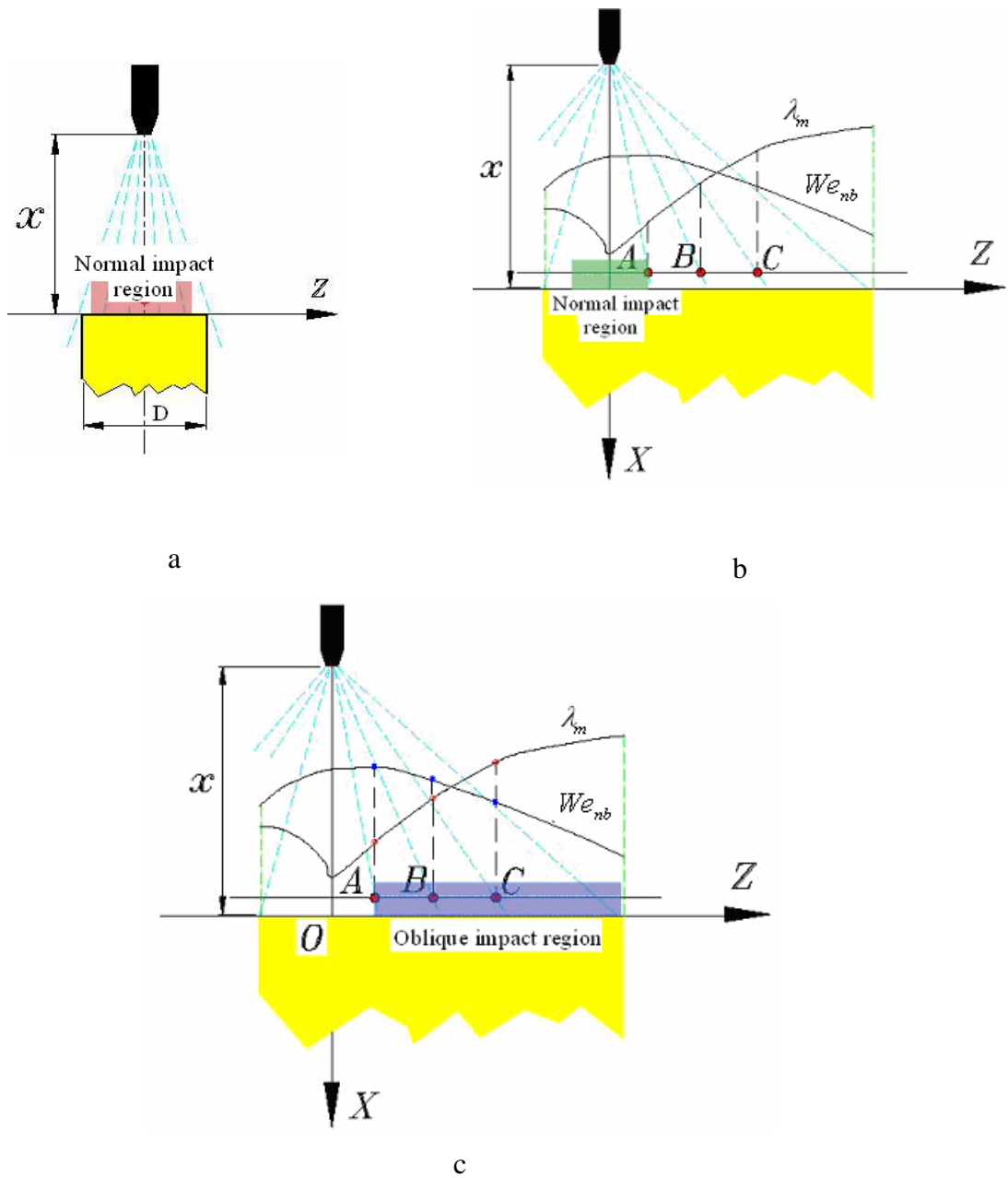


Fig. 3-24: Sketch for the normal impact region (a, and b), and oblique impact region (c).

3.3.6. Average film thickness

Parallel to the drop measurements using the phase Doppler technique, visualization of the liquid film on the target was performed in order to estimate the average thickness of the liquid film. Such visualization and its evaluation are pictured in Fig. 3-25.

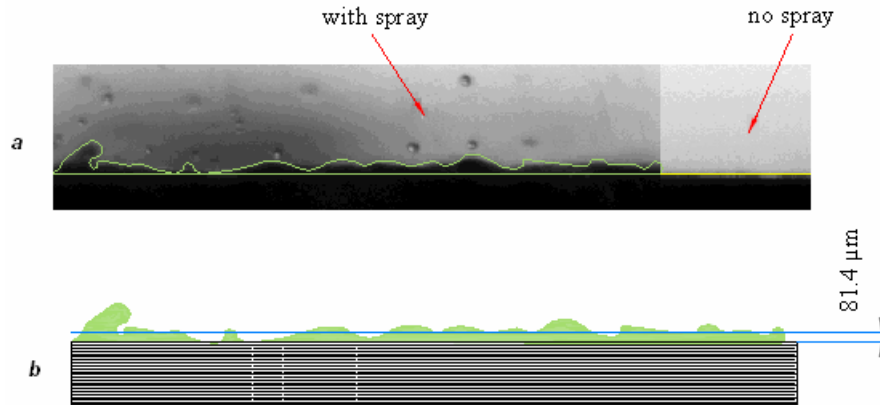


Fig. 3-25: Thin liquid film formed under spray impact: a) original image of CCD camera with interface contour added, and b) synthesized image to be integrated yielding the average film thickness.

The average film thickness was then calculated by averaging 60 to 100 randomly chosen images from 500 instantaneous film thicknesses obtained by high speed CCD camera. The average film thickness is then computed from wall film images using the Eq. (3.17) as pictured in Fig. 3-26.

$$\bar{h} = \frac{1}{L} \int_0^L h(z) dz \quad (3.16)$$

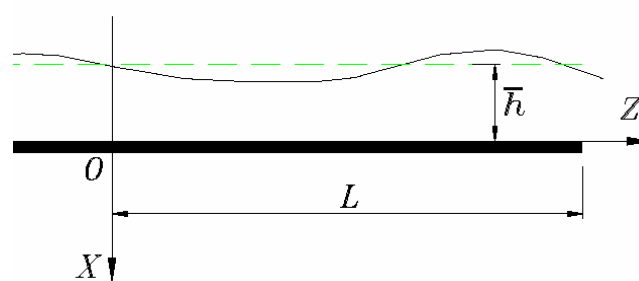


Fig. 3-26: Sketch for the accumulated wall liquid film to be integrated yielding the average film thickness.

In the experiments reported above, the film thickness varied in the range $8\mu\text{m} \leq \bar{h} \leq 107\mu\text{m}$ and the standard deviation in the range $(5\mu\text{m} \leq \bar{\sigma}_h \leq 22.34\mu\text{m})$ for corresponding impingement Weber numbers in the range $10 < \text{We}_{nb} < 160$. An exemplary variation of the standard deviation σ_h as a function of the measured average film thickness is illustrated in Fig. 3-27. It is recognized from this figure that the standard deviation of the measured film thickness does not correlate with the measured average film thickness.

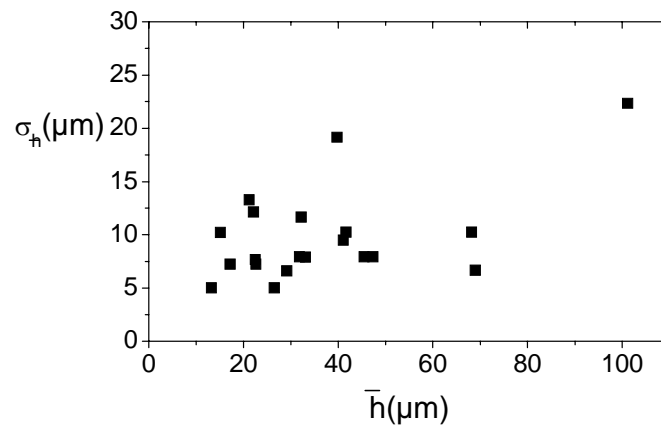


Fig. 3-27: An exemplary variation of the standard deviation σ (h) as a function of the measured average film thickness.

Results of this study indicate that the average film thickness decreases with increasing the nozzle pressure at a given nozzle height, Fig. 3-28a. In Fig. 3-28b the variation of the measured average film thickness (\bar{h}) as a function of impact Reynolds number based on the normal component of velocity is presented for a normal impact condition, i.e., the impact Weber ratio was negligible ($\lambda_{we_b} \leq 0.023$). It is shown in Fig. 3-28b that the average film thickness decreases significantly with the impact Reynolds number in this experiment. A simple correlation for variation of the average film thickness as a function of impact Reynolds number can be expressed as

$$\bar{h} / d_{30b} = a \text{Re}_{nb}^{-b} \quad (r=0.84) \quad (3.17)$$

The coefficients a and b were found to be $\approx 2.21 \times 10^4$ and 1.77, respectively, based on the measured data in this study for a water spray impacting onto a stainless steel target with 5 mm in diameter ($D = 5\text{mm}$), negligible surface roughness ($\bar{\varepsilon}^* \ll 1$ and $\bar{\varepsilon}^* \ll \bar{h}$) and normal impact condition ($\lambda_{We_b} \leq 0.023$).

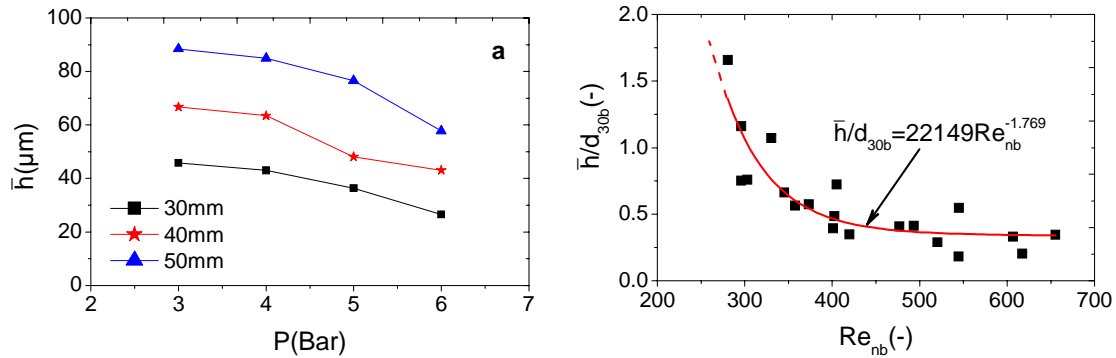


Fig. 3-28: Variation of the average film thickness: a) with the nozzle pressure at different nozzle height, and b) with the Reynolds number, for a stainless steel target with diameter of 5mm ($D = 5\text{mm}$).

Two exemplary results of the average film thickness (\bar{h}) together with the impact Weber number (We_{nb}), mass ratio (λ_m) and flux density (\dot{q}) are illustrated in Figs. 3-29a and b as a function of nozzle height (x) for two different nozzle pressures (3 and 6 bar) for a stainless steel target with diameter of 5mm ($D = 5\text{mm}$). It should be noted that both impact Weber number and flux density of impacting drops decrease with the nozzle height. It is shown in this figure that decreasing the impact Weber number yields an increase the accumulated wall film thickness but the decrease of the secondary-to-incident mass ratio (λ_m). The same behaviour was observed for the secondary-to-incident number ratio (λ_N). Note that in the conducted experiments, the entire target surface was exposed to the impacting spray, i.e., $D_{spray} / D > 1$.

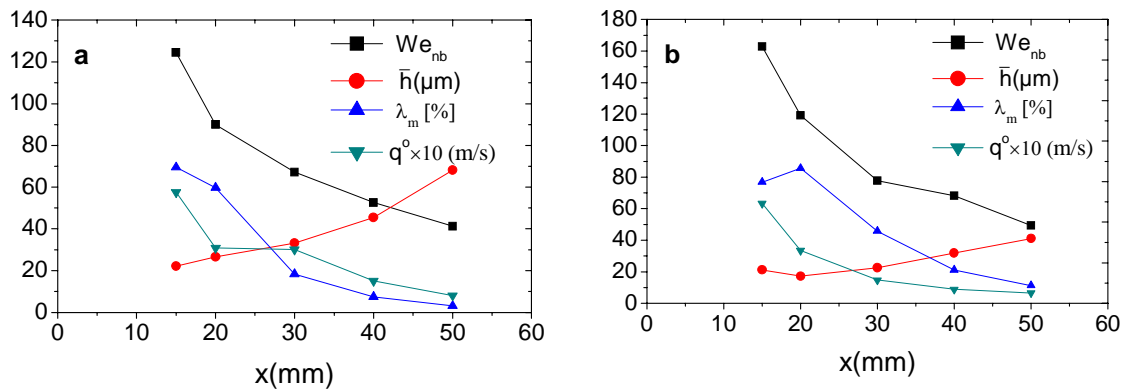


Fig. 3-29: Variation of the impact Weber number (We_{nb}), average film thickness (\bar{h}), mass ratio (λ_m) and flux density (\dot{q}) with the nozzle height (x) for two exemplary nozzle pressures: (a) 3 bar, and (b) 6 bar; for a stainless steel target with diameter of 5mm ($D = 5\text{mm}$).

3.4. Conclusions

From these experiments some general conclusions and quantitative experiments about the mean statistics of ejected drop properties as a function of impinging spray properties can be obtained. The quantitative experiments are summarized in Table 3-7, which are valid for the following experimental conditions:

- Smooth target surface, i.e., negligible surface roughness ($\bar{\varepsilon}^* \ll 1$ and $\bar{\varepsilon}^* \ll \bar{h}^*$).
- The entire target surface exposed to the impacting spray, i.e., $D_{\text{spray}}/D > 1$.
- The accumulated wall film thickness in the range $8\mu\text{m} \leq \bar{h} \leq 107\mu\text{m}$.
- Impingement Weber number in the range $10 < We_{nb} < 160$, based on the normal component of velocity before the impact.
- Low spray fluid viscosity, i.e., $Oh \ll 0.1$.

Some of the more important general observations are given in the points below.

- The average drop size ratio λ_{d10} (ejection to impingement) decreases with increasing Weber number (We_{nb}) based on the normal component of velocity before the impact.

- The normal component of velocity after the impact does not correlate well with the normal velocity component of the impinging droplet, while the tangential component of the ejected droplets correlates closely with the impingement tangential velocity.
- With increasing impact Weber number the ejection Weber number at first increases and then after reaching a maximum value decreases.
- At each measurement point, the impact Weber number increases monotonically with impact droplet size, while the ejection Weber number at first increases with ejected droplet size and then takes on a relative constant value.
- The mean reflection angle of ejected droplets strongly depends on the mean incident angle of impinging droplet, although no significant relationship between angle of droplets and droplet diameter can be observed at any one single measurement point.
- The mean impact Weber number ratio ($\lambda_{We_b} = We_{tb} / We_{nb}$) positively influences the number density of secondary droplets.
- The mass and number ratios ($\lambda_m = \dot{m}_a / \dot{m}_b$, $\lambda_N = \dot{N}_a / \dot{N}_b$) exhibit a very similar behavior compared with the Weber number ratio (λ_{We_b}) for oblique impact conditions ($\lambda_{We_b} > 0.1$). This is not true when these ratios are compared with the normal component of the impingement Weber number (We_{nb}).
- Two different impact conditions can be distinguished in a spray impact onto a flat and rigid wall: 1) normal impact: $\lambda_{We_b} = We_{tb} / We_{nb} < 0.1$, with no significant dependency between secondary to incident mass ratio (λ_m) and impact Weber number ratio (λ_{We_b}) and 2) oblique impact: $\lambda_{We_b} = We_{tb} / We_{nb} \geq 0.1$, with secondary to incident mass ratio (λ_m) increasing with impact Weber number ratio (λ_{We_b}).
- In the case of normal impact conditions ($\lambda_{We_b} < 0.1$), the secondary to incident mass ratio (λ_m) increases with impact Weber number based on the

normal velocity component (We_{nb}) whereas this ratio decreases with impact Weber number in the case of oblique impact conditions ($\lambda_{We_b} \geq 0.1$).

- In the case of normal impact conditions ($\lambda_{We_b} < 0.1$), the secondary to incident mass ratio (λ_m) mostly falls in the range [0.002, 0.85], whereas this ratio falls in the range [0.016, 1.12] for oblique impact conditions ($\lambda_{We_b} \geq 0.1$).
- Non-dimensional crown radius and height of a splashing droplet in spray impact phenomena have mostly smaller growth rate in compare with a single or train of drop impact onto a stationary liquid film.
- The average film thickness decreases with increasing the impact Weber number (We_{nb}) in the case of a normal impact condition.
- The average film thickness decreases with increasing nozzle pressure at a given nozzle height.
- Average film thickness increases significantly with the nozzle height.

Table 3-6: Summary of the empirical model for a water spray impact onto small flat and rigid walls.

Measured quantity	General correlation	Coefficients	Correlation coefficient (r)
Normal component of velocity (m/s)	$u_a / u_b = -\alpha_1 \cdot (We_{nb})^{-\beta_1}$	$\alpha_1 = 1.1$ $\beta_1 = 0.36$	0.65
Tangential component of velocity (m/s)	$v_a = \alpha_2 \cdot v_b + \beta_2$	$\alpha_2 = 0.862$ $\beta_2 = 0.094$	0.93
Droplet trajectory angle (deg)	$\theta_a = \alpha_3 \cdot \theta_b + \beta_3$	$\alpha_3 = 0.623$ $\beta_3 = 41$	0.80
Mean droplet size (um)	$d_{10a} / d_{10b} = -\alpha_4 \cdot We_{nb} + \beta_4$	$\alpha_4 = 0.003$ $\beta_4 = 1.2$	0.90
Mass ratio (normal impact, $\lambda_{We_b} < 0.1$)	$\lambda_m = (\dot{m}_a / \dot{m}_b) = \alpha_5 \cdot We_{nb} + \beta_5$	$\alpha_5 = 6.74 \times 10^{-3}$ $\beta_5 = -0.204$	0.89
Mass ratio (oblique impact, $\lambda_{We_b} \geq 0.1$)	$\lambda_m = \alpha_6 \cdot We_{nb}^{-\beta_6}$	$\alpha_6 = 35$ $\beta_6 = 1.63$	0.72
Number ratio (normal impact, $\lambda_{We_b} < 0.1$)	$\lambda_N = (\dot{N}_a / \dot{N}_b) = \alpha_7 \cdot We_{nb} + \beta_7$	$\alpha_7 = 2.2 \times 10^{-3}$ $\beta_7 = 8.96 \times 10^{-2}$	0.64
Number ratio (oblique impact, $\lambda_{We_b} \geq 0.1$)	$\lambda_N = (\dot{N}_a / \dot{N}_b) = \alpha_8 \cdot We_{nb}^{-\beta_8}$	$\alpha_8 = 7.1$ $\beta_8 = 1.14$	0.70

Chapter 4

4. Spray impact onto flat and rigid walls: Formation of the liquid film

This section presents an experimental study of the liquid film under various well-defined spray conditions in which both the impinging and the secondary spray characteristics are captured. The experimental results are complemented by theoretical expressions regarding the hydrodynamics of liquid films under sprays and preliminary models for the average wall film thickness and secondary spray are formulated.

4.1. Introduction

In the phenomena of spray/wall interaction, it has become apparent in recent years that the liquid film formed on the surface plays an important role in determining the velocity and size of ejected droplets as well as the deposited mass fraction, see e.g., Bai et al. (2002), Cossali et al. (1999). This is also evident from the results of the previous chapter, in which the wall film thickness displayed systematic dependencies on the operating conditions of the spray. Nevertheless, formation of the wall film often being neglected in spray impact models. However, prediction of average film thickness and average velocity is very important for many industrial applications, especially involving spray cooling systems or for fuel injection sprays onto heated walls because

these parameters significantly affect the efficiency of heat transfer in the sprayed surfaces. In some technical applications, it is desirable to eliminate the deposited film on the wall as far as possible, e.g. in internal combustion engines, whereas in some cases the maximum deposition is required, e.g. in spray coating, spray painting or agricultural sprayers. On the other hand, the induced fluctuations in liquid layer formed on the rigid walls may decrease the quality of coated or painted surfaces. Meanwhile, the average film thickness can affect the properties of secondary spray, splashing threshold, ejected mass and number of secondary droplets. It is shown by Cossali et al. (1997) that in the case of a single drop impact onto a stationary liquid film, the number of secondary droplets decreases as the depth of liquid layer is increased. For indicating the influence of the average liquid film thickness on the splash limiting criterion, several expressions have been introduced, e.g. $K_{Cr} = 2100 + 5880 \cdot \bar{h}^*$ ($\bar{h}^* = \bar{h} / d_b$, where \bar{h} is the average film thickness) by Cossali et al. (1997), or $K_{Cr} = 1304 + 5032\bar{h}^*$ for $0.1 < \bar{h}^* \leq 1$ by Kalantari and Tropea (2006b). In these criteria, splashing occurs if: $K = We \cdot Oh^{-0.4} > K_{Cr}$, where Oh is Ohnesorge number defined as: $Oh = \sqrt{We} / Re$.

Furthermore it seems that the velocity fluctuations inside the accumulated wall film have an influence on the splashing phenomenon, since in a spray impact the crown base radius exhibits a growth rate proportional to $(t^* - \tau_R)^{n_R}$; $0.2 \leq n_R \leq 0.32$, significantly different than that of a single or train of single droplets impacting onto an undisturbed liquid layer, $\sim (t^* - \tau_R)^{0.5}$, as investigated theoretically by Yarin and Weiss (1995).

There exist numerous models regarding the formation of the wall film generated by an impacting liquid spray, see e.g., Stanton and Rutland (1996), Lee et al. (2001), and Bai and Gosman (1996), Ahmadi-Befuri et al. (1996).

The model of Stanton and Rutland (1996) solves the continuity and momentum equations for a two-dimensional film flow over an arbitrary solid surface using the Euler equations. This model considers many physical effects such as shear forces and dynamic pressure of impacting droplets, but neglects the Laplace (capillary) pressure arising from curvature of the air-liquid film interface. In this model the dynamic pressure of impacting droplets is expressed in the form of

$$P_{dyn} = \rho_L \sum_{i=1}^{N_b} \left[u_b^2 (A_d / A_{wall}) \right]_i \quad (4.1)$$

where u_b is the normal velocity component of the impacting droplet, A_d and A_{wall} are the area of the impacting droplet and wall cell area, respectively.

The model of Lee et al (2001) uses a different expression for the dynamic pressure of impacting droplet

$$P_{dyn} = \left[(1 - \theta) \rho_L \cdot u_b^2 \right] \cdot \xi \quad (4.2)$$

where θ is the void fraction and ξ is a random number; $\xi = \text{rnd}(0,1)$.

In general, the previous models do not take into account the flux density of impacting spray, an issue which will be considered in the theoretical derivations presented in this chapter and suitable estimators for dynamic pressure of impacting spray will be presented.

The present section is an experimental study of the liquid film under various well-defined spray conditions in which both the impinging and the secondary spray characteristics are captured. The experimental results are complemented by theoretical expressions regarding the hydrodynamics of liquid films under sprays and preliminary models for the average wall film thickness and secondary spray are formulated.

4.2. Experimental set-up

The experimental set-up used in this work is similar to the test rig used in the previous chapter. The spray was created using two different full-cone nozzles from Spraying System Co., operated at pressures between 3 and 7 bars. Two different stainless steel targets with diameter of 5mm and 15mm ($D=5$ and 15mm) have been used in this study, using the end face of the cylinders.

The nozzles were placed at different positions above the target surface varied from 20 to 50 mm, e.g. ($x_{nozzle} = -20$ mm). To characterise the spray, a dual-mode phase Doppler instrument from Dantec Dynamics was used, comprising a transmitting optics with a 400mm focal length, a receiving optics with a 310mm focal length, and an ‘‘A’’ type mask at a 34° scattering angle. The impacting and ejecting droplets were measured 1mm above each target (i.e., $x = -1$ mm). Experimentally the film has been characterised using a high-speed CCD camera. The average wall film thickness (\bar{h}) is obtained by

averaging over several instantaneous images after first removing the reference wall image.

4.3. Formation of the wall liquid film

In general, spray impingement on walls is characterized by the two different structures: the generated secondary spray, and the accumulated liquid wall film, see Fig. 4-1. The thickness of the accumulated wall film varies between microns to millimetres, depending on the condition of impacting spray and the boundary conditions on the target. Experimentally it is equally important to also capture the prevailing boundary conditions for any particular film, which in this case comprises the physical boundaries of the rigid surface, e.g. spherical target, flat plate, deep pool etc., and the characteristics of the impacting spray in terms of velocity, size and number density of impacting droplets.

Formation of the liquid film on a rigid-flat wall due to spray impact can be divided into the two different regions (Fig. 4-1);

- (i) Impingement region that is under influence of the impacting droplets and has lower thickness, and
- (ii) Outer region that is free of any impact phenomena. Film flow in this region depends on the film Reynolds number; $Re_f = \rho \bar{u}_f \cdot \bar{h} / \mu$, and can be either laminar or turbulent.

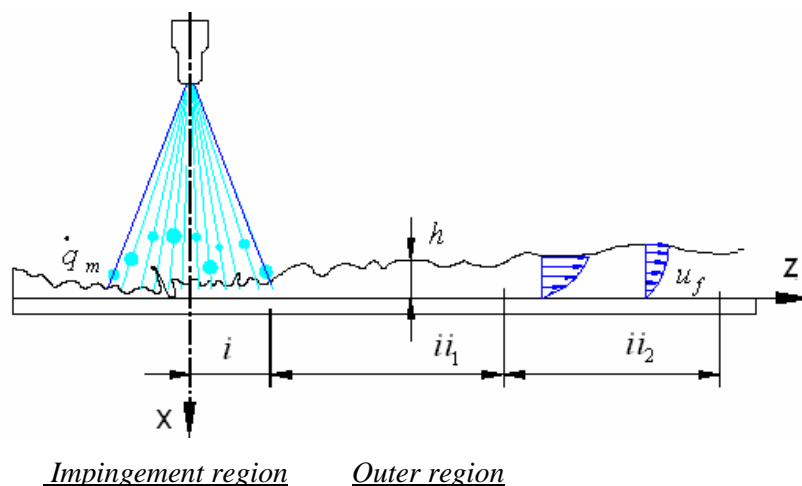


Fig. 4-1: Impingement and outer region of thin liquid film formed under spray impact.

A characterization of the accumulated wall liquid film can be achieved using:

- average film thickness (\bar{h})
- average spreading film velocity (\bar{u}_f)
- velocity fluctuations inside the accumulated liquid film (u'_f)

The average film thickness depends on several parameters of the impacting spray; mean normal and tangential components of impact velocity \bar{u}_b and \bar{v}_b , flux density of impacting spray ($\dot{q} = q/A$; “q” and “A” to be flux of the impacting spray and the reference area over which flux is measured), volume-averaged diameter of impacting droplets (d_{30b}), density (ρ) and viscosity of the liquid used in spray (μ) and also the boundary condition of the target; average target surface roughness ($\bar{\varepsilon}^*$, where $\bar{\varepsilon}^* = \bar{\varepsilon}/d_{10b}$) and target size (D). A general expression for the average film thickness can be written as

$$\bar{h} = \psi \left(\bar{u}, \bar{v}, d_{30b}, \dot{q}, \rho, \mu, \bar{\varepsilon}^*, D_{\text{spray}} / D \right) \quad (4.3)$$

where, D_{spray} is the diameter of the effective impinging spray on the target defined as:

$D_{\text{spray}} = 2x_{\text{Nozzle}} \cdot \tan(\alpha/2)$, α is the spray cone angle. The parameters $\bar{u}, \bar{v}, d_{30b}, \dot{q}$ and D_{spray} vary with nozzle pressure and nozzle height above the target. The three first parameters may be able to be combined into an impact Reynolds or Weber number. However \dot{q} is not an independent parameter and depends also on the impact Weber number, since flow rate of a atomizer and atomizing pressure (P) which influences the impact Weber number, are connected to each other with a power law; $q \sim P^{0.5}$. This dependency can be obtained theoretically by considering the Bernoulli's equation for inside and outside of the atomizing nozzle or experimentally as examined in this study.

Two exemplary images of thin liquid film formed on the rigid surface are presented in Fig. 4-2, for a relative sparse spray (a) and for a relative dense spray (b). It is apparent from these sample images that in describing the hydrodynamics of the film, e.g. velocity fluctuations inside the film, the capillary pressure will be non-negligible. Furthermore, the local film velocity will be an important parameter determining the outcome of any single drop impact event.

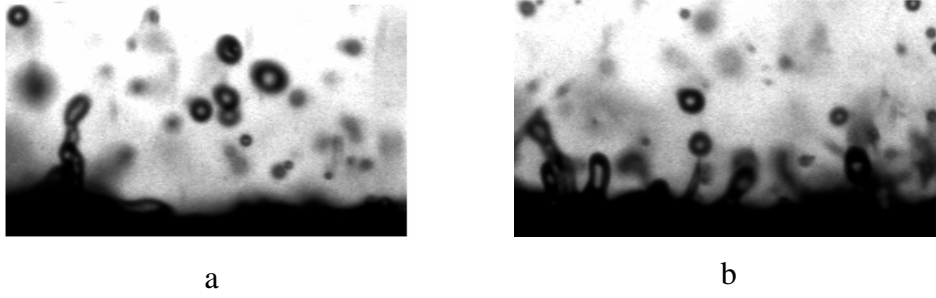


Fig. 4-2: Sample images of the liquid film interface formed under spray impact: a) relatively sparse spray, b) relatively dense spray.

Assuming that spray and liquid film formed on the wall are isotropic in the Y - Z plane, the continuity equation of the film thickness for both regions can be written in the form:

$$\frac{\partial h}{\partial t} + \frac{\partial(hu)}{\partial z} + \frac{\partial(hv)}{\partial x} = \Gamma_m \quad (4.4)$$

and the momentum equation is

$$\frac{\partial(\rho u)}{\partial t} + \frac{\partial(\rho uu)}{\partial z} + \frac{\partial(\rho uv)}{\partial x} = -\frac{\partial P}{\partial z} + \mu \left(\frac{\partial^2 u}{\partial z^2} + \frac{\partial^2 u}{\partial x^2} \right) + \rho g \quad (4.5)$$

In the following sections, different sources of the pressure term (P), influence of the gravity term (g) and mass source term (Γ_m) of the wall film will be discussed in more details.

4.3.1. Hydrodynamic pressure source in the wall liquid film

The pressure term for the liquid film can be considered as the sum of various contributions.

$$P = -P_\sigma + P_g + P_{dyn} \quad (4.6)$$

P_σ is the Laplace pressure due to the curvature of the air-liquid film interface, P_g is the pressure exerted from the ambient gas (air flow) onto the air-liquid interface and P_{dyn} is the dynamic pressure exerted from impacting droplets.

The dynamic pressure produced by the impinging droplets is the main source responsible for spreading and thinning of the liquid wall film in the impingement region.

On the other hand, the non-continuous nature of the impacting droplets causes a wavy form of the spreading liquid film interface in both regions (Fig. 4-1 and Fig. 4-2), therefore the capillary pressure gradient (P_σ) arises from film interface curvature either in the inner or in the first part of the outer zone, expressed by

$$P_\sigma = -\frac{\sigma}{(1+(dh/dz)^2)^{3/2}} \cdot \frac{d^2h}{dz^2} \quad (4.7)$$

To a first approximation, we may neglect the nonlinear terms involving the slope of the liquid-air interface ($dh/dz \ll 1$) to have a simpler and linear set of conditions at the interface, yielding

$$P_\sigma \cong -\sigma \frac{\partial^2 h}{\partial z^2} \quad (4.8)$$

In the second part of the outer region (ii_2 in Fig. 4-2), the Laplace pressure induced by the curvature of the air-liquid film interface is negligible, since the wavy surface has been stabilized. With such assumptions the velocity profile in the second part of the outer region can be considered to be in a quasi-steady-state form.

The main factor responsible for the spreading and thinning of the liquid film in the impingement region is the dynamic impingement pressure generated by the impacting droplets. This influence has been introduced already by Stanton and Rutland (1996) and Stanton and Rutland (1998).

The general form of the dynamic pressure of an impacting spray can be found in Roisman and Tropea (2005). The normal component of the dynamic force exerted on the wall by an impacting drop is given by

$$F_{dyn} = (m_b \cdot u_b - m_a \cdot u_a) / \Delta t \quad (4.9)$$

where subscripts a and b refer to after and before impact, respectively.

Defining the volume flow rate of the impacting drop by $q = V / \Delta t$, Eq. (4.7) can be rewritten as

$$F_{dyn} = \rho_L (q_b \cdot u_b - q_a \cdot u_a) \quad (4.10)$$

Considering the definition of dynamic pressure ($P_{dyn} = F_{dyn} / A$) and flux density of impacting droplets $\dot{q} [m/s] = q / A$, (4.8) yields

$$P_{dyn} = \rho_L \left(\dot{q}_b \cdot u_b - \dot{q}_a \cdot u_a \right) = \rho_L \dot{q}_b u_b \left(1 - \frac{m_a u_a}{m_b u_b} \right) \quad (4.11)$$

The coefficient $\beta = 1 - m_a u_a / (m_b u_b)$ in (4.11) takes into account the generated secondary droplets by an inertial impacting spray. By considering that u_a and u_b have different sign, an useful form of the coefficient β can be expressed in the form of

$$\beta \approx \max \left\{ 1, \left(1 + \lambda_m \cdot \left| \bar{u}_a / \bar{u}_b \right| \right) \right\} \quad (4.12)$$

Another approach for estimating the dynamic pressure of an impacting spray can be obtained by assuming that the rebounding drops have the same size and velocity as of the primary drops, i.e. $d_a = d_b$ and $u_a = -u_b$; then the dynamic pressure exerted on the wall by a rebounding drop is

$$P_{dyn-reb.} = 2 \rho_L \dot{q}_b u_b \quad (4.13)$$

The same procedure for a deposited droplet gives

$$P_{dyn-dep.} = \rho_L \dot{q}_b u_b \quad (4.14)$$

In the case of a spray impact, some droplets rebound, some others deposit on the wall, whereas some of them splash, therefore a constant factor β depending on the number of rebounding or depositing droplets should be considered, for instance

$$P_{dyn} = \beta \cdot \rho_L \bar{u}_b \dot{q} ; 1 < \beta < 2 \quad (4.15)$$

For a spray, the coefficient β can be estimated based on the number of ejected droplets from the wall in comparison to all the primary droplets, defined as

$$\beta \approx \min \left\{ \left(1 + \dot{N}_a / \dot{N}_b \right), 2 \right\} \quad (4.16)$$

As an asymptotic condition, if all of the impacting droplets rebound from the wall or deposit on the wall, then the expression (4.16) yields $\beta = 2$ or $\beta = 1$, respectively. A value between 1 and 2 accounts implicitly also for those droplets which result in partial deposition. In the case of a normal impact condition ($\lambda_{We_b} < 0.1$), the ratio \dot{N}_a / \dot{N}_b can be estimated as, see Fig. 4-4.

$$\lambda_N = (\dot{N}_a / \dot{N}_b) = 2.16 \times 10^{-3} \cdot We_{nb} + 8.96 \times 10^{-2} \quad (4.17)$$

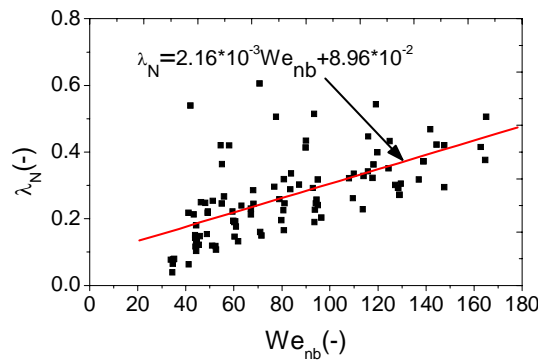


Fig. 4-3: Total secondary-to-incident number ratio as a function of impact Weber number based on the normal velocity component.

Note that the ratio \dot{N}_a / \dot{N}_b and N_a / N_b are identical in the spray/wall interaction, since the acquisition time for measuring the impinging and ejecting droplets from the wall is same (see section 3.3.5).

4.3.2. Influence of the gravity in the wall liquid film

In general, the shape of the air-liquid film interface is determined by the capillary (Laplace) length, defined by

$$L_c = \sqrt{2\sigma / (\rho g)} \quad (4.18)$$

If the capillary length is large compared to the dimensions of the system, i.e. depth of the liquid film, then gravity does not play a significant role in determining the shape of the air-liquid film interface and hydrodynamics of the liquid film. As an example, the

typical film thickness in this study was in the range $10\mu m \leq \bar{h} \leq 110\mu m$. Considering the average depth of the liquid film equal to $60\mu m$, $\sigma = 73 \times 10^{-3} N/m$ and $\rho = 1000 kg/m^3$ for water droplets, the dimensionless capillary length gives $L_c/\bar{h} = 64 \gg 1$, suggesting that the gravity may be neglected in the hydrodynamics of the spreading liquid film in this study. The same condition is consistent for most of the inertial spray impacting onto a rigid-flat surface. Neglecting the unnecessary gravity term in hydrodynamics of a spreading liquid film can significantly reduce the time required for the numerical computations.

4.3.3. Mass source term of the wall liquid film (Γ_m)

Results obtained in this study indicate that in the case of a normal spray impact ($\lambda_{We_b} < 0.1$), the secondary-to-incident mass ratio (λ_m) mostly falls in the range [0.002, 0.85], whereas for oblique impact conditions ($\lambda_{We_b} \geq 0.1$) this ratio falls in the range [0.016, 1.12]. The results also indicate that in the case of a normal impact condition ($\lambda_{We_b} < 0.1$), the secondary-to-incident mass and number ratio, λ_m and λ_N , increase linearly with the impact Weber number based on the normal component of the impact velocity (We_{nb}).

$$\lambda_m = (\dot{m}_a / \dot{m}_b) = 6.74 \times 10^{-3} \cdot We_{nb} - 0.204 \quad (4.19)$$

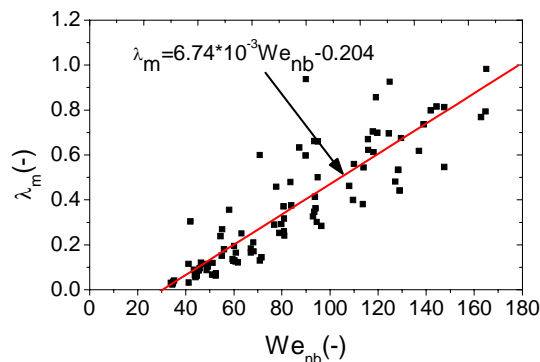


Fig. 4-4: Total secondary-to-incident mass ratio as a function of impact Weber number based on the normal velocity component.

Therefore, the mass source term of the wall liquid film in governing continuity equation (4.2) can be expressed as

$$\Gamma_m = \dot{m}_{dep}/(\rho A) = \dot{q}_{dep} \quad (4.20)$$

where $\dot{m}_{dep} = \dot{m}_b - \dot{m}_a$ for the inner region of the wall liquid film and can be obtained from (4.15) as

$$\dot{m}_{dep} = (1 - \lambda_m) \cdot \dot{m}_b \quad (4.21)$$

Therefore the mass source term for inner region can be expressed in the form

$$\Gamma_m = (1 - \lambda_m) \cdot \dot{q}_b \quad (4.22)$$

For the outer region of the liquid film, $\Gamma_m = 0$.

The correlations (4.17) and (4.19) were derived from numerous measurements conducted in the range $35 \leq We_{nb} \leq 165$ and $\lambda_{We_b} < 0.08$, Figs. 4-3 and 4-4, whereby again, each data point in these figures represent an average over 8000 to 20000 single drops.

4.4. Asymptotic solution for the wall film thickness

In the following sections, asymptotic solution for the average wall film thickness is divided into two different regimes:

- Low Reynolds regime, and
- High Reynolds regime.

4.4.1. Film flow in low-Reynolds regime

In the impingement region of a sparse, symmetric and stationary spray, we may assume that the frequency of the impacting drops is low enough, such that the velocity fluctuations inside the film and also the air-liquid film interface fluctuations are damped out ($\lambda \gg \bar{h}$ or $\varepsilon \ll \bar{h}$, see Fig. 4-5a) between the impact of two neighboring droplets. Under these conditions, the Laplace pressure arising from the air-liquid film interface

can be neglected. We may assume that the velocity inside the liquid film has only a horizontal component (\bar{u}_f), therefore the continuity equation can be simplified to

$$\int_0^{\bar{h}} \bar{u}_f \cdot dh = \int_0^L (1 - \lambda_m) \cdot \dot{q}_b \cdot dz \quad (4.23)$$

which after integration yields

$$\bar{h} = (1 - \lambda_m) \cdot \dot{q}_b \cdot L / \bar{u}_f \quad (4.24)$$

where L is size of the control volume in the Z -direction, i.e. length of the impact area on the rigid target exposed to the symmetric impacting spray (e.g. in the case of an symmetric impacting spray, L can be considered as radius of the target). On the other hand, the momentum equation of the wall film yields

$$-\frac{\partial P}{\partial z} + \mu \left(\frac{\partial^2 u}{\partial x^2} \right) = 0 \quad (4.25)$$

One possible solution for this differential equation (4.25) can be derived by considering that the second term on the (4.25) is constant in integrating over the z -component. After inserting the boundary condition ($x=0, u=0$) and ($x=h, \sigma_{xz} = \mu \frac{\partial u}{\partial x} = 0$), (4.25)

yields

$$u_f = A(hx - x^2/2) ; A = \frac{1}{\mu} \left(\frac{\partial P}{\partial z} \right) \quad (4.26)$$

where $u_f = \bar{u}_f + u'_f$

With the help of (4.26), the average velocity inside the liquid film can be expressed as

$$\bar{u}_f = \frac{1}{h} \int_0^{\bar{h}} A(hx - x^2/2) dx = \frac{1}{3} A \bar{h}^2 \quad (4.27)$$

Substituting the expression (4.27) into Eq. (4.24) yields

$$\bar{h}^3 = 3\mu \cdot (1 - \lambda_m) \dot{q}_b L \left(\frac{dP}{dz} \right)^{-1} \quad (4.28)$$

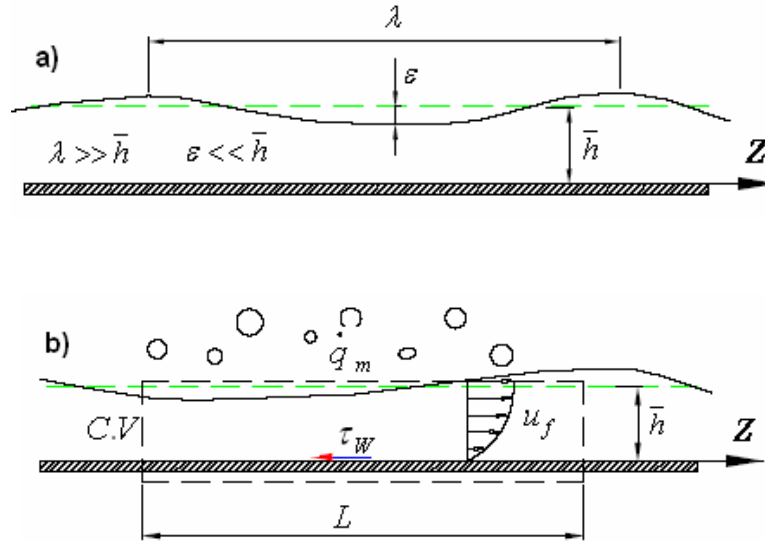


Fig. 4-5: a) Curvature of the liquid film-air interface, and b) Control volume (C.V.) for a spreading wall liquid film.

However this expression is difficult to use for estimating the average thickness of the deposited liquid film, because the values of dP/dz must be first estimated. Neglecting the pressure terms associated with the ambient gas flow and from the Laplace pressure, and assuming that dP associated by impacting droplet vanishes linearly in the z -direction; a simple form of dP/dz can be considered as, see Fig. 4-6.

$$\frac{dP}{dz} = \frac{P_2 - P_1}{z_2 - z_1} = \frac{C_1' P_1 - P_1}{C_1'' L} = \frac{(C_1' - 1) P_1}{C_1'' L} = C_1 \cdot P_{dyn} / L \quad (4.29)$$

Substituting (4.29) into (4.28) yields

$$\bar{h} = C \left[3\mu \cdot (1 - \lambda_m) \dot{q}_b L^2 / P_{dyn} \right]^{1/3} \quad (4.30)$$

Considering again the dynamic pressure of the impacting spray (4.15) and substituting into (4.30), one obtains after simplifications

$$\bar{h} / d_{10_b} = C \text{Re}^{-1/3} \left[3\beta^{-1} \cdot (1 - \lambda_m) L^2 \cdot d_{10_b}^{-2} \right]^{1/3} \quad (4.31)$$

In this expression, the coefficient C ($C = C_1^{-1/3}$) depends on the surface roughness, wall temperature and maybe the surface material, found to be equal to 32 for the measurements reported in this study.

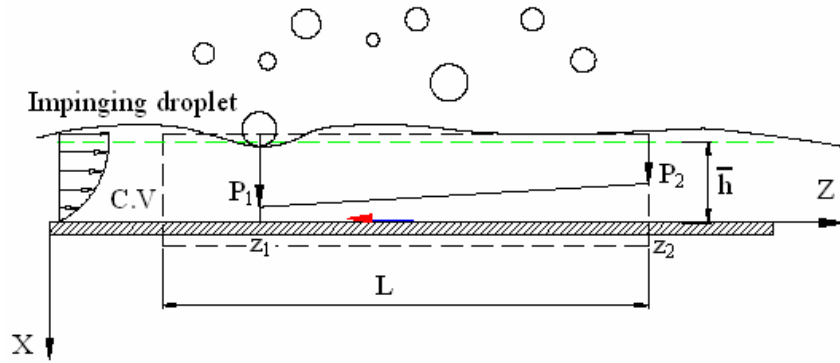


Fig. 4-6: Variation of the dynamic pressure due to the impinging droplets in a spray.

4.4.2. Scaling for the film thickness in the high-Reynolds regime

In the case of an inertial spray impact, i.e. $We / \sqrt{\text{Re}} \gg 1$, and using the dimensional analysis Eq. (4.3) for characterizing the average film thickness accumulated on the wall due to spray impact, the following expression can be derived:

$$\left(\frac{\bar{h}}{d_{30b}} \right) = f \left(\frac{1}{\text{Re}_b}, \frac{\dot{q}_b}{u_b} \right) \quad (4.32)$$

This is as far as dimensional analysis can predict. In this expression, d_{30b} is the volume

averaged droplet diameter defined as: $d_{30b} = \left(\sum_{i=1}^N d_i^3 / N \right)^{1/3}$.

An asymptotic solution of the average wall film thickness for a relative sparse spray (Fig. 4-7) can be obtained from result of a single drop impact onto a flat-rigid surface if the time period between the impacting droplets is much larger than the time scale required for complete spreading of the deposited liquid droplet (Fig. 4-8). This can be expressed in the following term

$$\overline{\Delta T}_{i,i-1} \gg t_{sp}^* \cdot \bar{d}_{dep} / \bar{u}_{dep} \quad (4.33)$$

where $\overline{\Delta T}_{i,i-1}$ is the average time period between the two neighbour impacting droplets, i.e. indicating the frequency of the impacting droplets ($\bar{f} = 1/\overline{\Delta T}_{i,i-1}$). Also t_{sp}^* is the dimensionless time required for complete spreading of the deposited droplet, \bar{d}_{dep} and \bar{u}_{dep} are the average diameter and velocity of the deposited droplets before the impact, respectively.

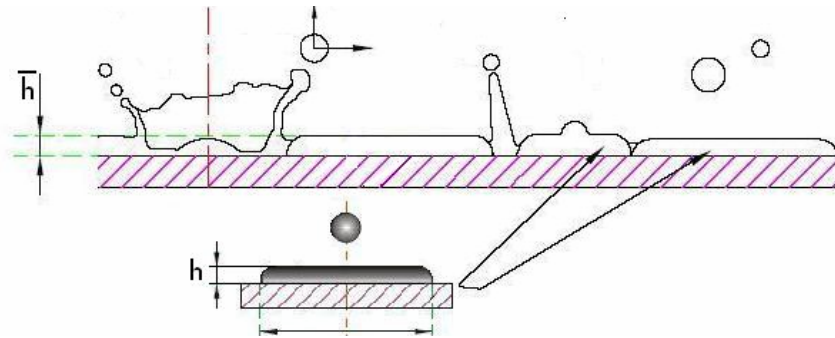


Fig. 4-7: Formation of the average film thickness under a relatively sparse spray.

Dimensionless time (t_{sp}^*) required for complete spreading stage is $8/3$ found by Pasandideh-Fard et al. (1996) or $(We/6)^{0.5}$ proposed by Fedorchenko and Wang (2004).

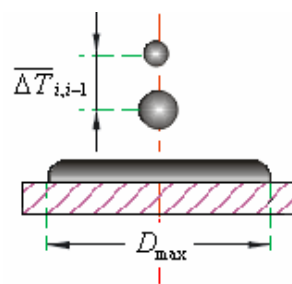


Fig. 4-8: Frequency of the impinging droplets in a spray.

In the case of a single drop impact, results of theoretical work (Pasandideh-Fard et al., 1996) indicate that impact of a single droplet onto a flat-rigid wall produces a splat with the maximum dimensionless diameter of

$$\xi = D_{\max} / d_0 = \sqrt{\frac{We + 12}{3(1 - \cos \theta_{ad}) + 4We / \sqrt{Re}}} \quad (4.34)$$

Experimental observations obtained by Pasandideh-Fard et al.,(1996) indicate that the maximum advancing dynamic contact angle (θ_{ad}) mostly falls in the range $110^\circ \leq \theta_{ad} \leq 140^\circ$ for different liquid droplets and will be considered equal to 110° for a water droplet impinging onto the rigid surface.

Considering the $We \gg \sqrt{Re}$ and $We_b \gg 12$ which is valid for most a inertial spray-wall interactions, Eq. (4.28) can be simplified into

$$\xi \cong 0.5 Re^{0.25} \quad (4.35)$$

Considering the mass balance for spreading droplet at its maximum diameter and assuming a disk shape yields

$$h^* = (2/3)\xi^{-2} \quad (4.36)$$

where h^* is the dimensionless film thickness formed on the wall defined as $h^* = h / d_0$.

Substituting (4.35) into (4.36) yields

$$h^* \cong 2.67 \cdot Re^{-1/2} \quad (4.37)$$

The dependency of h^* on $Re_b^{-1/2}$ in the case of a single drop impact for inertial impact condition, i.e. $We / \sqrt{Re} \gg 1$, indicates that maybe we can factor out the Reynolds number from (4.32), yielding

$$\left(\frac{\bar{h}}{d_{30b}} \right) = Re_b^{-1/2} \cdot f_1 \left(\frac{\dot{q}_b}{u_b} \right) \quad (4.38)$$

In the measurements conducted in this study, the ratio We / \sqrt{Re} falls in the range; $3.5 < We / \sqrt{Re} < 16$.

It is interesting to note that based on the work of Roisman et al. (2005), the crown lamella thickness (h_L) is expressed in the form of $h_L / d_0 \sim Re^{-1/3}$ for low impact Reynolds numbers ($Re < 1000$) and in the form of $h_L / d_0 \sim Re^{-1/2}$ for high impact Reynolds numbers ($Re > 2000$). Based on this result and Eq. (4.37) for dimensionless film

thickness on the wall due to a single drop impact, we may emphasize the role of Reynolds number as a scaling parameter of film hydrodynamics.

One simple form of the (4.38) can be written as

$$\bar{h} = \alpha \cdot d_{30b} \cdot \text{Re}_b^{-1/2} \cdot \left(\frac{\dot{q}_b}{u_b} \right)^\gamma \quad (4.39)$$

Where α and γ are constant values found to be 4 and -0.5, respectively. These constants have been found based on the measured data in this study for a water spray impacting onto a stainless steel target with 5 mm in diameter ($D = 5\text{mm}$), negligible surface roughness ($\bar{\varepsilon}^* \ll 1$ and $\bar{\varepsilon}^* \ll \bar{h}$) and normal impact condition ($\lambda_{we_b} \leq 0.023$).

4.5. Results and discussion

The dimensionless average film thickness accumulated on the flat-rigid wall as a function of Reynolds number before the impact is presented in Fig. 4-9 together with the predictions obtained from Eq.(4.31). Results in this figure indicate that the dimensionless average film thickness decreases significantly with the Reynolds number before the impact. Results presented in this figure also indicate that the theoretical prediction presented in this study (Eq.4.31) yields good agreement with the experimental data, mostly for the thin or shallow liquid film condition, Kalantari and Tropea (2006d).

In the experiments presented in this figure (Fig. 4-9), the normal velocity component varies in the range $8 \text{ m/s} \leq \bar{u}_b \leq 18 \text{ m/s}$, the flux density of the impacting spray varies in the range $0.5 \text{ m/s} \leq \dot{q}_b \leq 16 \text{ m/s}$, and the volume averaged droplet size varies in the range $53 \mu\text{m} \leq d_{30b} \leq 75 \mu\text{m}$. The coefficient C is found to be 32 based on the measurements condition reported above for a stainless steel flat-rigid target with the smooth surface condition, i.e. $\bar{\varepsilon}^* \ll 1$.

The obtained theoretical expression for estimating the average film thickness on the wall (4.31) has been derived based on the laminar boundary layer type film flow, i.e. $Re_{\text{film}} < 500$, and also examined for the lower Reynolds numbers in this study ($Re_{\text{nb}} < 700$). Therefore validity of this expression remains consistent for $Re_{\text{film}} < 500$. The

dependency of the film thickness on the impact Reynolds number in this expression, i.e., $\bar{h}/d10_b \sim Re^{-1/3}$, is consistent with the results of Roisman et al. (2005) which is valid for low impact Reynolds numbers ($Re < 1000$), see Fig. 4-10.

On the other hand, the obtained expression based on dimensional analysis (4.39) has been derived for a general spray impact condition and has no limitation to use. However applicability of this expression for higher Reynolds number should be examined in future applications. The only important note in using both expressions for film thickness is that the entire target surface should be exposed to the impacting spray, i.e., the whole target surface should be under the impacting spray ($D_{spray}/D > 1$).

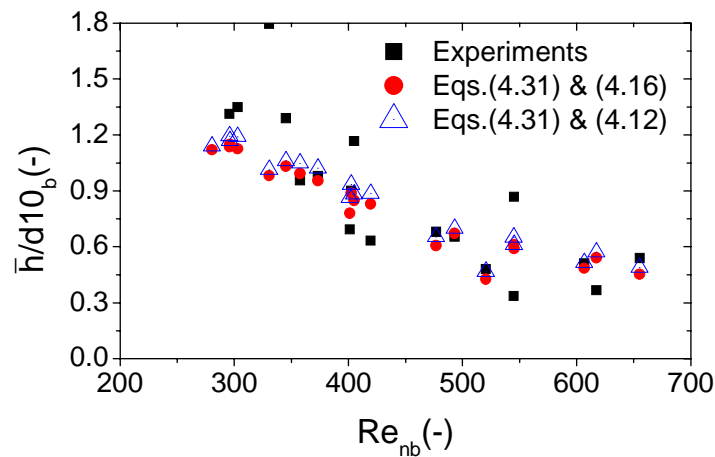


Fig. 4-9: Average dimensionless film thickness accumulated on the flat-rigid wall as a function of Reynolds number before the impact.

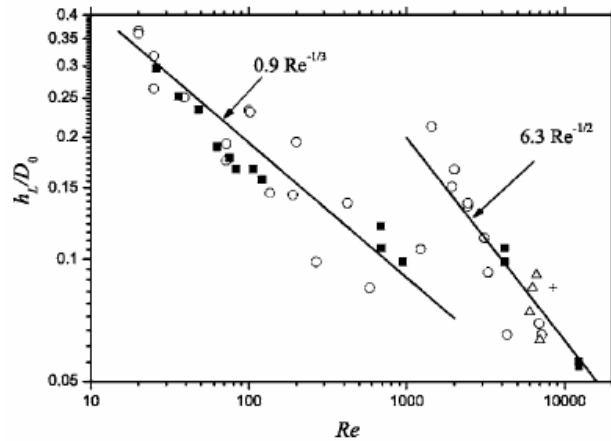


Fig. 4-10: Variation of the non-dimensional thickness of the spreading lamella as a function of impact Reynolds number at the instant of d_0/u_0 , Ref: Roisman et al., (2006).

In Fig. 4-11 predictions of the dimensional analysis (Eq.4.39) for the average film thickness is presented together with the many individual measurements data as a function of Reynolds number before the impact. In this figure each individual average film thickness (\bar{h}) is normalized by the volume averaged droplet diameter before the impact (d_{30b}). The results presented in this figure indicate good prediction of the average film thickness obtained from dimensional analysis (Eq.4.39). Results presented in this figure also indicate that the Reynolds number before the impact is the main factor responsible for spreading and thinning the liquid film accumulated on the flat-rigid walls and indicates that the average impact Reynolds number must be appeared in the characteristic length scale of the average film thickness. Influence of the impact Reynolds number on the average film thickness can be observed also from the theoretical expression derived for the averaged film thickness (Eq.4.31).

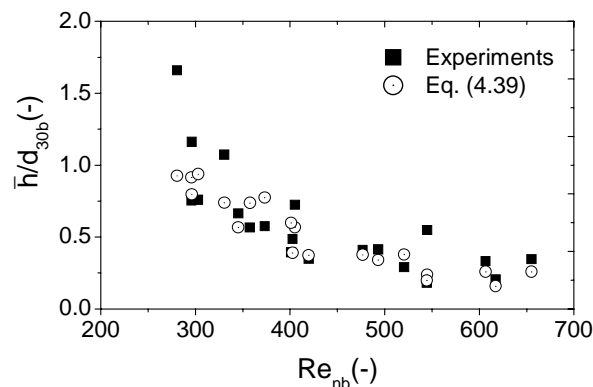


Fig. 4-11: Prediction of the dimensional analysis for the average film thickness.

In Fig. 4-12a and b, the total secondary-to-incident mass (λ_m) and number (λ_N) ratio of the impacting spray as a function of the average wall film thickness is presented. Results presented in this figure indicate that the total secondary-to-incident mass and number ratio decreases significantly with increasing the average wall film thickness. Note that the impact Weber number is not constant for measurements presented in this figure (Fig. 4-12a, b) and the average film thickness changes due to the variation of the impact Weber number. Impact Weber number based on the normal velocity component varies within the range $20 \leq We_{nb} \leq 165$ in this figure.

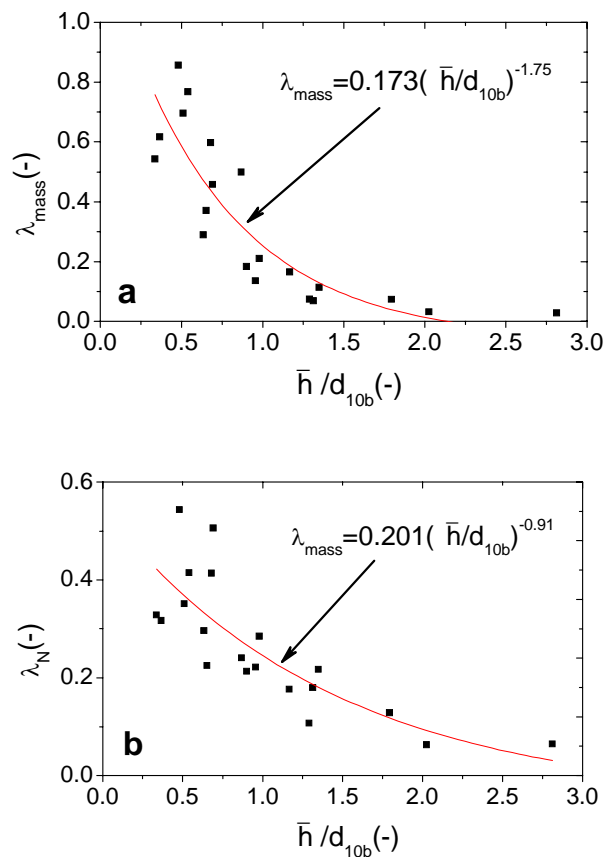


Fig. 4-12: Total secondary-to-incident: a) mass ratio (λ_m), and b) number ratio (λ_N).

For illustrating the influence of the average wall film thickness on the total secondary-to-incident mass and number ratio, simple correlations are obtained:

$$\lambda_m = (\dot{m}_a / \dot{m}_b) = 0.173 \cdot (\bar{h} / d_{10b})^{-1.75} \quad (4.40)$$

$$\lambda_N = (\dot{N}_a / \dot{N}_b) = 0.201 \cdot (\bar{h} / d_{10b})^{-0.91} \quad (4.41)$$

Note that empirical expressions for λ_m and λ_N were also given in chapter 3 for normal and oblique spray impact (Eqns. 3-12 to 3-15). These did not include any direct influence of the film thickness, but expresses the λ_m and λ_N only as a function of the normal impact Weber number We_{nb} . However it must be recognized that the film thickness used in Eqns. 4-40 and 4-41 is inherently also a function of We_{nb} .

For illustrating the influence of the wall film thickness on the mass ratio in the case of constant impact Weber numbers, some exemplary results are presented in Fig. 4-13. It is shown in this figure that the average wall film thickness has non-predictable and complex influence on the mass ratio in the presence of a constant impact Weber number. The results presented in this figure indicate again the complexity of the spray impact phenomena. Physically increasing the average wall film thickness, yields a decrease in the number of splashed droplets (resulting in a decrease of the number of ejected droplets from splashed droplets), but yields also an increase of the number of secondary droplets generated from ejected wall films. Meanwhile several interaction sources must also be considered in generating the secondary droplets; interactions between two droplets (two ingoing drops, ingoing and ejecting drop or two secondary droplets), between an uprising jet and a drop and between a splashing droplet and other droplet (ingoing or ejecting droplet). Therefore all of these phenomena are involved in generating the secondary spray and this fact is reflected in the scatter of the data points in this figure. It is also shown in this figure that the impact Weber number has a strong influence on the total secondary-to-incident mass ratio in the case of a normal impact condition. As an example, decreasing the impact Weber number from 128 to 60 yields decreasing the mass ratio from 0.5 to 0.1.

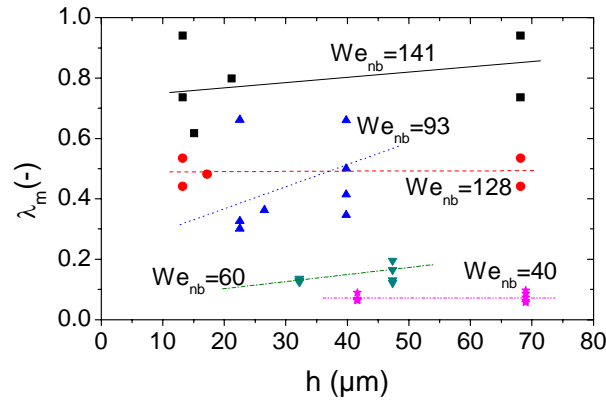


Fig. 4-13: Influence of the average film thickness on the total secondary-to-incident mass ratio for different constant impact Weber numbers.

Note that in the conducted experiments, the entire target surface was exposed to the impacting spray, i.e., $D_{spray} / D > 1$. In this definition, D_{spray} is the diameter of the effective impinging spray on the target defined as: $D_{spray} = 2x_{Nozzle} \cdot \tan(\alpha / 2)$, α is the spray cone angle.

4.6. Discussion

This chapter presents a new simplified theoretical model for predicting the average film thickness as a function of mean Reynolds number of impacting drops, flux density of the impacting droplets, and the average drop diameter. Theoretical derivation for the average film thickness shows good agreement with the measured data in the thin liquid film condition, i.e. $\bar{h}^* = \bar{h} / d_{10b} \leq 1$. Predictions of the obtained expression for the average film thickness based on the dimensional analysis indicate also good agreement for most of the many individual measurements. Results obtained in this study indicate a significant influence of the Reynolds number on the average film thickness accumulated on the flat-rigid wall due to a liquid spray impact.

In the case of constant impact Weber numbers, the average film thickness has a complex and non-predictable influence on the total secondary-to-incident mass ratio for the conducted measurements in this study, despite the fact that the dimensionless average film thickness falls in the thin liquid film conditions $\bar{h}^* \leq 1$.

As illustrated above, the mean film thickness varied in the range $8\mu\text{m} < \bar{h} < 107\mu\text{m}$, corresponding to an impingement Weber number in the range $10 < We_{nb} < 165$, based on the normal velocity component.

Chapter 5

5. Comparison between splash of a droplet in isolation and in a spray

In this chapter, an experimental and theoretical study of splashing droplet in isolation and in a spray is presented. A high-speed camera with 32 kfps has been used to characterize the splashing droplets in spray impact. The present work provides a fundamental comparison of the splashing phenomenon for single drops and for drops in a spray, followed by a theoretical model. Such comparisons can be very valuable for future modelling of spray impact.

5.1. Introduction

In an overall effort to model the impact of liquid sprays onto rigid walls, the splashing phenomena plays an important role in determining the velocity and size distribution of ejected droplets from the wall as well as the ejected mass fraction, see e.g., Coghe et al. (1999), Cossali et al. (1997), Cossali et al. (1999), Kalantari and Tropea (2005), Kalantari and Tropea (2006d), Mundo et al. (1997), Mundo et al. (1998), Roisman et al. (2002), Roisman et al. (2005), Roisman et al. (2006), Sivakumar and Tropea (2002). Especially in the splash dominant region of an impacting spray, i.e., $We_{nb} > 80$, due to increasing the number of splashing droplets, the Weber number after impact decreases with increasing impact Weber number, Kalantari and Tropea (2005). In practice, increasing the number of splashing droplets in spray impact phenomena can decrease

the quality of coated or painted surfaces. A large number of parameters and variables can influence the splashing phenomenon; physical properties of droplet fluid: viscosity, surface tension and density, impact parameters: impact velocity, flux density of impacting droplets, i.e. frequency of impacting droplets, and droplet trajectory, and target characteristics (rigid wall: dry or wetted wall (surface roughness, wall temperature), liquid layer (film thickness, surface roughness). From the listed parameters, two of them are very important in determining the onset of splashing: surface roughness and average depth of accumulated liquid film on the wall, e.g. splashing takes place faster for rough surfaces as postulated by Mundo et al. (1998) and Range and Feuillebois (1998). Therefore, the ratio of average wall roughness to the average primary droplet size ($\bar{\varepsilon}^* = \bar{\varepsilon}/d_b$, where $\bar{\varepsilon}$ is the average of roughness of the target surface) should be considered if rough or structured surfaces are used. Josserand et al. (2005) investigated the triggering of splashing by using a small obstacle on a dry-solid surface. Also the ratio of the average liquid film thickness accumulated on the wall to the average primary droplet size ($\bar{h}^* = \bar{h}/d_b$, where \bar{h} is the average film thickness) must be considered in the case of accumulated wall film. For indicating the influence of the average liquid film thickness on the splash limiting criterion, several expressions have been introduced, e.g. $K_{Cr} = 2100 + 5880 \cdot \bar{h}^*$ ($\bar{h}^* = \bar{h}/d_b$, where \bar{h} is the average film thickness) by Cossali et al. (1997), or $K_{Cr} = 1304 + 5032\bar{h}^*$ for $0.1 < \bar{h}^* \leq 1$ by Kalantari and Tropea (2006d). In these criteria, splashing occurs if: $K = We \cdot Oh^{-0.4} > K_{Cr}$, where Oh is Ohnesorge number defined as: $Oh = \sqrt{We}/Re$. This limiting criterion can be also taken from an $Oh-Re$ diagram, see e.g. Mundo et al. (1997). Results obtained by Rioboo et al. (2003) indicates that in the case of a thin liquid film, the splashing threshold depends only on the impact Weber or K-number and is independent of the dimensionless film thickness. Also it is shown by Cossali et al. (1997) that in the case of a single drop impact onto a stationary liquid film, the number of secondary droplets decreases as the depth of liquid layer is increased. Furthermore it seems that the velocity fluctuations inside the accumulated wall film have an influence on the splashing phenomenon.

On the other hand, splashing phenomena in a spray impact can be interacted by the impacting droplets or influenced by other simultaneously spreading or splashing droplets.

A fundamental comparison of the splashing phenomenon for single drops and for drops in a spray can therefore be very valuable for future modelling of spray impact. The present work provides such a comparison experimentally, followed by a derived theoretical model.

5.2. Experimental set-up

The experimental arrangement used in this work was similar to that section in Fig. 3-7. Experimentally the splashing droplets in the spray have been characterised using a high-speed camera with 32 kfps. The spray was created using different full-cone nozzles from Spraying System Co., operated at pressures between 3 and 7 bar and flow rate between 27 and 40 lit/hr. Both flow rate and pressure were variable and measured. The targets were also varied, using the end face of steel cylinders with diameter of 5 or 15 mm. The nozzles were placed between 15 and 50 mm above the target and varied in displacement from the target central axis on the target diameter.

The average film thickness was then calculated by averaging several instantaneous film thicknesses obtained by high speed camera. In the experiments reported in this study, the non-dimensional film thickness varied in the range $0.25 \leq \bar{h}^* \leq 1$ for corresponding average impingement Weber numbers in the range $10 < We_{nb} < 160$, remained in the thin liquid film condition, see Table 3-1.

5.3. Results and discussion

In the following sections some characteristics of splashing droplet in isolation and in a spray will be presented. In section 5.3.1, maximum non-dimensional crown height will be estimated theoretically based on the energy conservation. Exemplary measurements of the different splashing phenomena in spray will be presented in order to illustrate the difference from splash in isolation, i.e. impact of a single droplet onto a stationary liquid film.

5.3.1. Splashing droplet in isolation

A sketch of a single droplet splashing on a liquid layer is illustrated in Fig. 5-1. During the splash, an uprising crown-like thin liquid sheet develops at the kinematics discontinuity position (point “B”: a point between the spreading droplet and unperturbed wall film with very high velocity and film thickness gradient). This crown-like sheet is bounded with a free end rim due to the surface tension effect, which generates finger-like jets disintegrating into the secondary droplets.

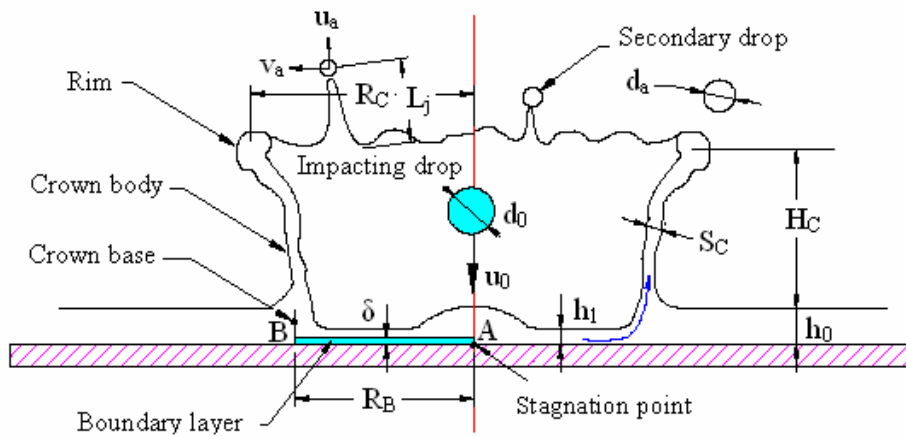


Fig. 5-1: Sketch for structure of a splashing liquid droplet.

In this section an energy conservation approach is considered for estimating the maximum crown height during the crown development. The energy conservation links the total energy of the impacting droplet and splashing crown. Total kinetic and surface energy of the impacting droplet onto liquid film is

$$E_0 = \underbrace{\frac{1}{12} \pi \rho d_0^3 u_0^2}_{Kinetic} + \underbrace{\sigma \pi d_0^2}_{Surface} \quad (5.1)$$

During the droplet spreading, kinetic energy dissipation takes place at the boundary layer of the spreading droplet between the stagnation point and the kinematics discontinuity point. Energy dissipation in the boundary layer of a spreading droplet is estimated similar to a methodology derived by Pasandideh-Fard et al. (1996), generalized for a splashing droplet as

$$E_{diss} = \int_0^{t_c} \int_{\Omega} \Phi d\Omega dt \approx \Phi \Omega t_c \quad (5.2)$$

where Ω is the volume of boundary layer of the spreading droplet which energy dissipation takes place in it, Φ is the viscous dissipation function that can be expressed in a simple form of $\alpha \cdot \mu (u/\delta)^2$; in which α is a constant value, and δ is the thickness of the boundary layer defined as: $\beta \cdot d_0 / \sqrt{\text{Re}}$; β is a constant coefficient. Total energy dissipation can be then expressed in the form

$$E_{diss} = \pi(\alpha/\beta)\rho u_0^2 d_0 R_B^2 \frac{t_c^*}{\sqrt{\text{Re}}} \quad (5.3)$$

where R_B is the crown base radius and t_c^* is dimensionless time measured from the impingement to the maximum crown height. Based on the measurements obtained by Cossali et al. (1997), it can be considered that at the instant of the maximum crown height, i.e. $t_c^* \cong H_C^*/0.15$, Eq. (5.3) yields in the form of

$$E_{diss} \cong \frac{\pi}{10} \rho u_0^2 d_0 R_B^2 \frac{H_C^*}{\sqrt{\text{Re}}} \quad (5.4)$$

Here H_C^* is non-dimensional maximum crown height measured from the wall film surface to the rim centerline (Fig. 5-1). In Eq. (5.4), the value of $0.15\alpha \cdot \beta^{-1}$ is found to be approximately 10 based on the measurement data used in this study.

Gravitational potential energy of the spreading lamella, crown body and crown rim is expressed in the approximated form

$$E_g \cong \underbrace{\frac{1}{2} \pi \rho g (h_0 - h_1)^2 R_B^2}_{\text{Lamella}} + \underbrace{\frac{3}{2} \pi \rho g (R_B + R_C) S_c H_C^2}_{\text{Crown}} + \underbrace{2\pi^2 \rho g R_C r_R^2 H_C}_{\text{Rim}} \quad (5.5)$$

where R_C is crown upper radius, h_0 and h_1 are undisturbed film thickness and thickness of the spreading droplet, respectively.

Potential surface energy of the lamella, crown body and crown rim is

$$E_{\sigma} \cong \underbrace{2\pi\sigma(h_0 - h_1)R_B}_{\text{Lamella}} + 2\sigma \underbrace{\left[2\pi \left(\frac{R_B + R_C}{2} \right) H_C \right]}_{\text{Crown}} + \underbrace{4\pi^2\sigma R_C r_R}_{\text{Rim}} \quad (5.6)$$

With considering $R_C = R_B + H_C \cdot \tan \theta_C$ and $\tan \theta_C = 1 - 4h_0^*$ from Fedorchenko and Wang (2004), the second term of (5.6), i.e. potential surface energy of the crown body can be expressed as

$$E_{\sigma\text{-crown}} = 2\sigma \left\{ 2\pi H_C \left[R_B + \frac{1}{2} H_C (1 - 4h_0^*) \right] \right\} \quad ; \text{ for } h_0^* < 0.25 \quad (5.7)$$

$$E_{\sigma\text{-crown}} = 4\pi\sigma R_B H_C \quad ; \text{ for } h_0^* \geq 0.25 \quad (5.8)$$

Here several parameters inside the obtained equations should be determined; first a relation between the crown base radius and the crown height at the instant of the maximum crown evolution is required, see Fig. 5-2.

To obtain this relationship, consider a general form of the time history for the crown base radius in the form of (see e.g. Yarin and Weiss, 1995).

$$R_B^* \sim (t^* - \tau_0)^{0.5} \quad (5.9)$$

where τ_0 is a constant value in the range $\tau_0 \in [0, \xi]$; ξ is a small constant value corresponding to the initial condition of the splash.

A relation between R_B^* and H_C^* at the instant of the maximum crown height can be obtained by substituting $\tau_0 = 0$, $t_c^* \cong H_C^* / 0.15$ at the instant of the maximum crown height, and a average constant coefficient equal to 2.2 for the crown base radius from Cossali et al. (1999) in the (5.9), yielding

$$R_B^* \cong 5.68 H_C^{*0.5} \quad (5.10)$$

This relationship will be used in simplification of the several obtained expressions, e.g., the gravitational potential energy, or potential surface energy.

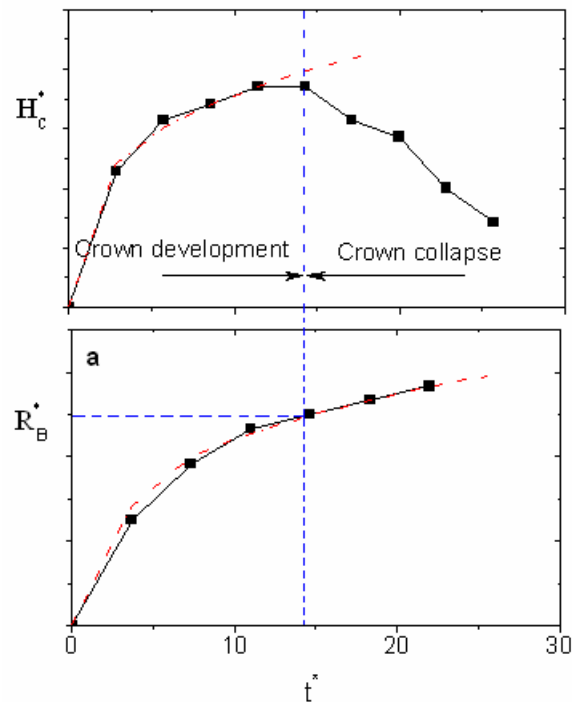


Fig. 5-2: Sketch for structure of a splashing liquid droplet.

Another necessary approach is estimating the crown thickness at the instant of the maximum crown height. Experimental results obtained by Cossali et al., (2004) indicate that the wall film thickness and impact velocity has no significant influence on the crown body thickness. Most important feature of the crown thickness observed by Cossali et al. (2004) is that the crown thickness increases significantly with dimensionless time. The same behaviour was observed by Fedorchenko and Wang (2004) and successfully analytically predicted by them, see Fig. 5-3. They found an analytical expression for the crown thickness in the form of

$$h = \lambda / 2.619 \quad (5.11)$$

where λ is the instantaneous wavelength on the crown surface close to the crown rim, see Fig. 5-3.

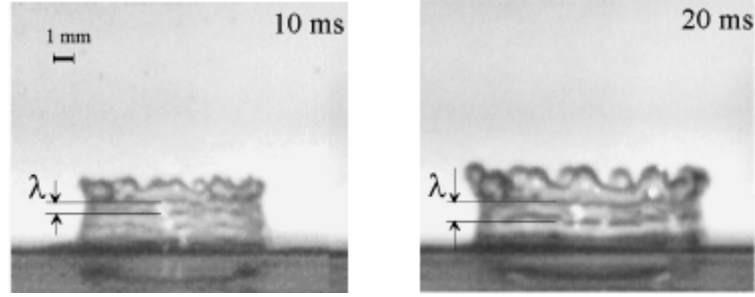


Fig. 5-3: Determination of the instantaneous crown thickness at the instant of crown evaluation, Ref: Fedorchenko and Wang (2004a).

The main limitation of this expression (5.11) in this study was the lack of original data to measure the wavelength on the crown body and therefore to use this expression.

Another relation for the crown thickness is recently introduced by Horvat et al. (2006) and Roisman et al., (2006) as a function of impact Reynolds number at the instant of d_0/u_0 based on the spreading lamella on the rigid wall in the form of

$$h_L = 0.9d_0 \text{Re}^{-1/3} \quad \text{for } \text{Re} < 1000 \quad (5.12)$$

$$h_L = 6.3d_0 \text{Re}^{-1/2} \quad \text{for } \text{Re} > 2000 \quad (5.13)$$

To estimate the crown thickness at the instant of the maximum crown height, experimental data from Coghe et al. (1999) is used in this study which presented in Fig. 5-4.

It is shown in this figure that the crown thickness at the instant of maximum crown height is distributed around the value $S_C^* \approx 0.22$ independent of the impact Weber number and the wall film thickness. This value will be used in this approach.

An approximate value for the radius of the crown rim (r_R) is considered based on the experimental observation of Range and Feuillebois (1998), see Fig. 5-5. The results presented in this figure suggests an approximate value for the radius of the rim in the form of

$$\frac{r_R^*}{R_C^*} \cong \frac{1}{20} \quad (5.14)$$

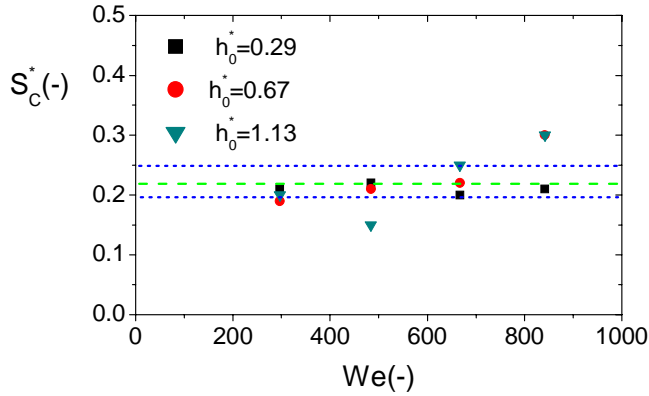


Fig. 5-4: Crown thickness at the instant of the maximum crown height as a function of impact Weber number for various wall film thicknesses.

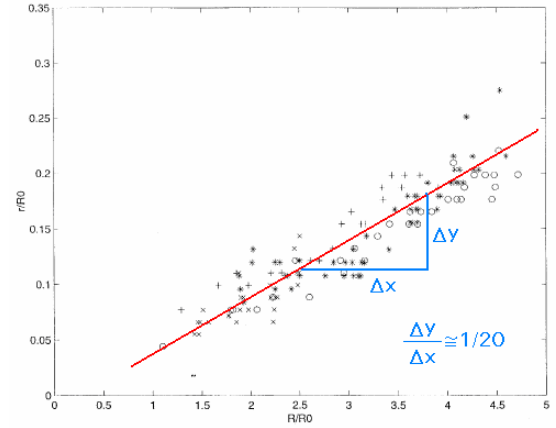


Fig. 5-5: Variation the non-dimensional radius of the crown rim as a function of non-dimensional crown upper radius, Ref. Range and Feuillebois (1998).

Energy balance ($E_0 = E_{diss} + E_g + E_\sigma$) at the maximum crown height ($H_{c_{max}}^*$) for $h_0^* \geq 0.25$ yields

$$\sum_{n=1}^6 A_n \cdot (H_{c_{max}}^*)^n = A_0 \quad (5.15)$$

$$A_0 = \frac{We}{12} + 1 ; A_1 = \sqrt{30} D_f^* ; A_2 = \frac{15}{4} \left(\frac{We}{Fr} \right) D_f^{*2} + \frac{3\pi}{2} ; A_3 = 11 ; A_4 = \frac{3}{4} \left(\frac{We}{\sqrt{Re}} \right) ;$$

$$A_5 = 0.55 \left(\frac{We}{Fr} \right) ; A_6 = \frac{3\pi}{80} \left(\frac{We}{Fr} \right)$$

Which We , Re , and Fr are dimensionless impact parameters defined as: $We = \rho u^2 d_0 / \sigma$;

$Re = \rho u d_0 / \mu$; $Fr = u^2 / g d_0$, also $D_f = h_0(1 - h_1/h_0)$.

On the other hand, mass balance during the splashing crown is

$$\underbrace{\pi \rho g (R_B + R_C) S_c H_C}_{Crown} + \underbrace{2 \pi^2 \rho g R_C r_R^2}_{Rim} = \frac{\pi}{6} d_0^3 + \eta_m \underbrace{\left[\pi \rho g R_B^2 h_0 \right]}_{Lamella} \quad (5.16)$$

where η_m is a constant value indicating the entering of the wall film fluid into the crown body. In the case of $h^* \geq 0.25$, the mass balance (5.16) can be simplified to

$$\eta_m \cong \min \{0.34 H_C^{*0.5} h_0^{*-1}, 1\} \quad (5.17)$$

This result shows that some part of the wall film is fed into the crown body during crown development; this part increases with impact Weber number, e.g. in the case of $h_0^*=1$ and $H_{C_{\max}}^*=2$, about 48% of liquid inside the cavity is feed into the crown body. The $\eta_m = 1$ corresponds to the condition of film dry-out.

Theoretical results in the case of single isolated drops indicate that the non-dimensional crown height increases nonlinearly with increasing the impact velocity, see Fig. 5-6. On the other hand, the non-dimensional crown height decreases slightly with the non-dimensional film thickness as illustrated in Fig. 5-7, corresponding to the wall film thickness varied in the range $0.25 < h_0^* < 1$.

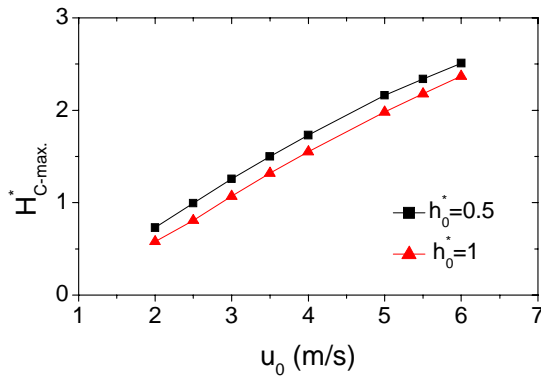


Fig. 5-6: Maximum non-dimensional crown height as a function of impact velocity for two different non-dimensional film thicknesses, $d_0=3$ mm.

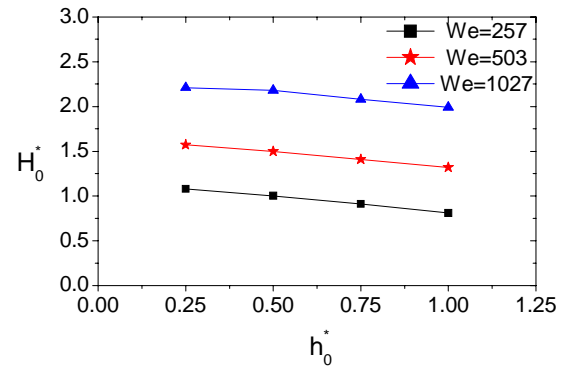


Fig. 5-7: Influence of non-dimensional film thickness on the maximum non-dimensional crown height.

Results of this theoretical approach for predicting the maximum crown height Eq. (5.15) is presented in Fig. 5-8 compared to experimental measurements for different impact conditions and wall films obtained by Cossali et al. (1997) for a single drop impacting onto a stationary liquid film.

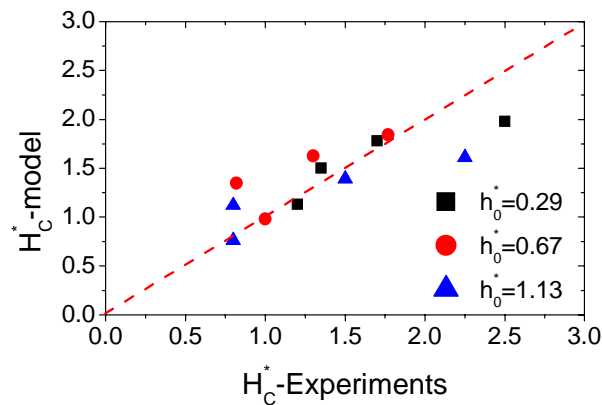


Fig. 5-8: Prediction of the maximum non-dimensional crown height as a function of the experimental measurements obtained by Cossali et al. (1997).

In the next step, result of splashing phenomena in isolation will be compared with splashing phenomena in spray.

5.3.2. Splashing droplet in a spray

Our observations and that of other investigations, e.g. Sivakumar and Tropea (2002) indicate clearly that the splash created by a drop in a spray differs significantly from that of an isolated single drop impact or from the impact of a train of drops on a stationary liquid film, examined by Cossali et al. (1997) and Yarin and Weiss (1995). These differences can be easily seen in Figs.3.1a and b, indicating that splash of a droplet in spray impact is much more irregular and non-symmetric in comparison to the symmetric propagation of a crown in the case of an isolated single droplet impact onto an undisturbed liquid layer.

In Fig. 5-9 maximum non-dimensional crown height is presented as a function of Weber number before the impact in spray impact condition. Results presented in this figure indicate that the non-dimensional crown height increase linearly with the Weber number before the impact. A linear correlation can be considered as

$$H_C^* = 3.9 \times 10^{-3} We_{nb} - 3.54 \times 10^{-2} \quad (r=0.81) \quad (5.18)$$

Note that the obtained correlation Eq. (5.18) and the theoretical derivation for the maximum crown height Eq. (5.15) give the crown height up to the crown rim (see Fig. 5-1) and therefore do not consider the height of the finger-like jets ejected from the

crown lamella. Therefore the detection volume must be placed above the given heights by taking into account the height of elongation jets from the crown lamella. Experimental results obtained by Coghe *et al.* (1999) indicate that the non-dimensional growth rate of the elongated jets from the crown lamella is independent of the impact velocity and wall film thickness, which is introduced in the form

$$\frac{dL_j^*}{dt^*} = 0.034 \quad (5.19)$$

Simple integration of this expression at the instant of the maximum crown height, and considering again $t_c^* \cong H_C^* / 0.15$ yields

$$L_{j-\max}^* \cong 0.23H_C^* \quad (5.20)$$

This expression predicts the maximum jet elongation from the crown rim, but not the jet height. Assuming that the finger-like jets move normal to the wall in the case of $\bar{h}_0^* \geq 0.25$, Eq. (5.20) suggests that the measurement volume of the phase Doppler instrument must be placed at least 23% higher than the computed maximum crown height either by Eq. (5.15) or by Eq. (5.18), i.e., above the " $H_{C-\max} + L_{j-\max}$ " otherwise the secondary droplets generated by splashed droplets will not be detected. In the measurements conducted in this study, maximum height of the splashing crowns fall in the range $270 \mu\text{m} \leq H_C \leq 492 \mu\text{m}$ with average value of $384 \mu\text{m}$ and Standard deviation of $92.2 \mu\text{m}$. Tacking into account the maximum jet elongation from the crown rim based on the Eq. (5.20) gives the minimum measurement volume height of the phase Doppler instrument 0.6 mm ($1.23 \times 0.492 \text{ mm}$) from the film surface. Note that either Eq. (5.15) or Eq. (5.18) estimates the maximum crown height from the film interface. Considering the maximum accumulated wall film thickness of $100 \mu\text{m}$ in this study gives the minimum measurement volume height of the phase Doppler instrument $\approx 0.7 \text{ mm}$ from the wall surface. Based on this result, placement of the measurement volume at 1 mm above the rigid wall will capture all of the secondary droplets generated from splashing droplets in this study.

Maximum non-dimensional crown height estimated from Eq. (5.15) as a function of the experimental results is presented in Fig. 5-10.

Theoretical estimations presented in Fig. 5-10 for splash in spray impact condition lie for most cases under the line “ $y=x$ ” whereas results presented in Fig. 5-8 for the isolated splash exhibit good agreement with the measurement data.

Based on the conducted measurements in this study, non-dimensional crown base radius and height of a splashing droplet in a spray as a function of dimensionless time is expressed in the following forms

$$R_B^* \sim (t^* - \tau_R)^{n_R} \quad (5.21)$$

$$0.1 \leq \tau_R \leq 2.5 \quad \text{and} \quad 0.2 \leq n_R \leq 0.32$$

$$H_C^* \sim (t^* - \tau_H)^{n_H} \quad (5.22)$$

$$0.5 \leq \tau_H \leq 3.5 \quad \text{and} \quad 0.25 \leq n_H \leq 0.5$$

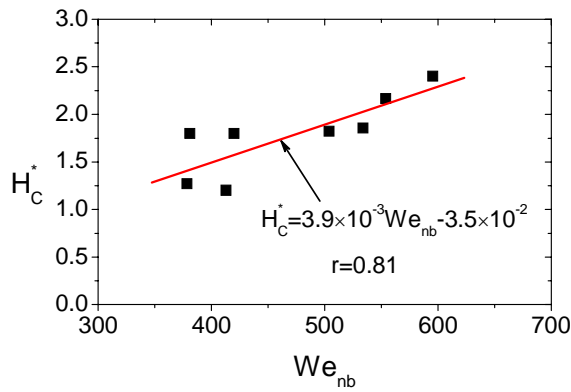


Fig. 5-9: Maximum non-dimensional crown height as a function of impact Weber number before the impact in spray.

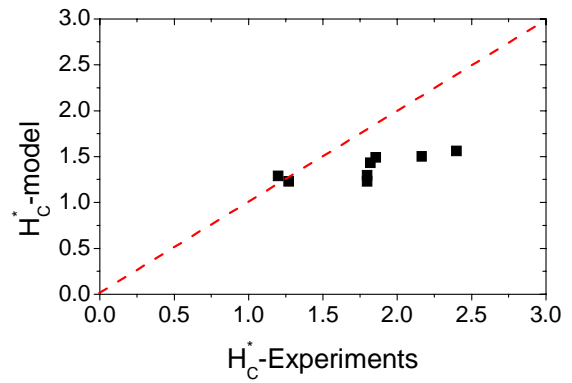


Fig. 5-10: Maximum non-dimensional crown height estimated from Eq. (4.8) as a function of the experimental results.

These obtained growth rates for crown base radius and height for a splashing droplet in a spray are significantly different than that of a single or train of single droplets impacting onto an undisturbed liquid layer, proportional to $t^{0.5}$ obtained theoretically by Yarin and Weiss (1995) or experimentally by Cossali et al. (1997). An exemplary experimental result of crown base radius and height for a splashing droplet in a spray is presented in Fig. 5-11a and b for the impact Weber number $We_{nb}=554$ and non-dimensional film thickness $h^*=0.4$.

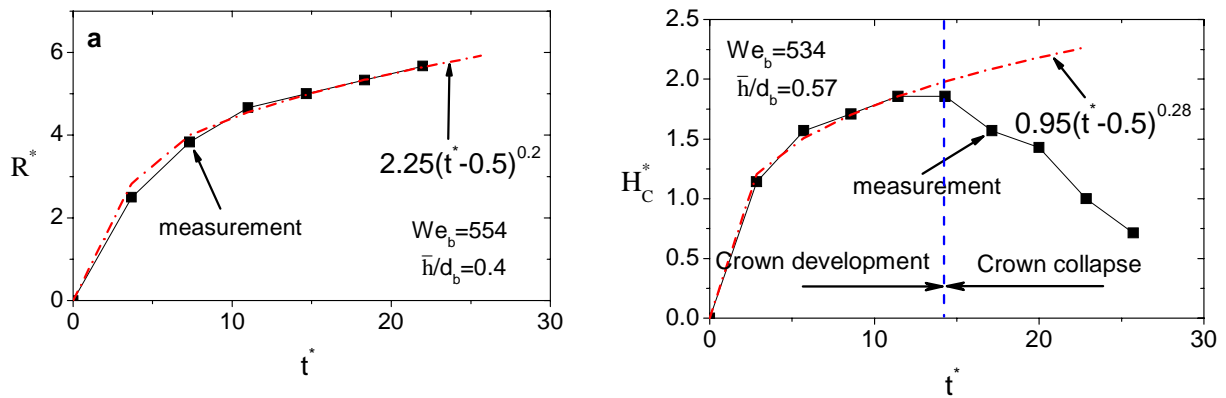


Fig. 5-11: Exemplary experimental result of crown base radius and height for a splashing droplet in a spray.

5.4. Conclusion

The theoretical equation for the maximum crown height is developed based on the energy conservation method. The theoretical prediction is then compared with the available measurement results for single drop impact and spray impact conditions. Theoretical predictions properly estimate the maximum crown height in the case of a splash in isolation, i.e. single drop impact, whereas slightly underestimate in the case of a splash in spray impact conditions. Perhaps in the case of a spray impact, velocity fluctuations inside the wall film cases such differences. Results obtained in this study indicate that the maximum non-dimensional crown height increases linearly with the Weber number before the impact in spray impact phenomena. Also results obtained in this study indicate that the growth rates for crown base radius and crown height for a splashing droplet in a spray are significantly different than that of a single or train of single droplets impacting onto an undisturbed liquid layer.

Chapter 6

6. Oblique spray impingement onto rigid walls: Description of secondary spray

In this chapter, an experimental study of oblique spray impingement onto a flat and rigid surface is presented. A phase Doppler instrument has been used to measure drop size and two components of velocity directly above the target. Characterization of spray-wall interaction, including velocity and trajectory of secondary droplets also mass and number ratio of secondary spray has been performed. An interesting feature of these experiments is the rather large oblique impact conditions due to the different injection angles exiting from the pressure nozzle. In this section some new features of oblique spray- wall interaction will be presented.

6.1. Introduction

Spray impingement onto rigid walls occurs in many industrial and technical applications, such as direct injection in Diesel engines, gas turbines, agricultural sprays, spray cooling, spray painting and spray coating. Physically two important interacting hydrodynamic phenomena must be correctly captured in describing spray impact: the generation of secondary droplets and the liquid film accumulating on the wall. Origins of secondary droplets are: from a splash with disintegrating crowns, from liquid jetting from the liquid film, or from rebounding droplets. The overall structure of the

accumulated wall film consists of deposited droplets and partial deposition part of splashing droplets. In some technical cases the deposited film on the wall should be eliminated as far as possible, e.g. in first start of Diesel engines, whereas in some other cases the maximum deposition is required, e.g. in spray coating, spray painting or agricultural sprayers. Much of the previous literature on the topic of spray impact, usually being restricted to the normal impact of a single drop onto a solid-dry or wetted wall or sometimes onto a thin liquid film, where generally the impact conditions can be carefully controlled, see e.g. (Bai and Gosman, 1995; Bai et al., 2002; Mundo et al., 1998; Stanton and Rutland, 1998), or normal injection of spray impact phenomena, see e.g. Kalantari and Tropea (2006b) or Roisman and Tropea (2005). In most cases including some of the former issues, the results of single droplet impact are extrapolated to the case of spray-wall interaction by simple superposition of many individual droplets. Such approaches however cannot reflect the interactions (Fig. 5-1); interactions in a spray between two droplets (two ingoing drops, ingoing and ejecting drop or two secondary droplets), between an uprising jet and a drop and between a splashing droplet and other droplet (ingoing or ejecting droplet). On the other hand, each theoretical or numerical study regarding to spray-wall interaction must consider many physical effects influencing the behaviour of deposited film or secondary spray: the tangential momentum of oblique impacting droplets that exist in the case of real spray impact conditions; effect of film fluctuations on the outcome of impacting droplets; effect of multiple droplet interactions and also the creation of the central jets and droplets due to break-up of the liquid film under impacting drops and also interaction between uprising jets or crowns with ingoing drops or other splashing droplets.

The main propose of the present section is experimental study of oblique spray impingement onto a flat and rigid wall yielding to describe some new feature of spray-wall interaction. Results obtained in this work can be implemented in characterization or modelling of oblique spray- wall interaction phenomena. The experiments have been performed in a condition near to the case of a real Diesel injection system with a flat piston head. In fact the main motivation of the presented section is to characterize the secondary spray formed due to the oblique spray impingement condition. For measuring

the two velocity components and size of each individual droplet, a dual mode Phase Doppler technique has been used.

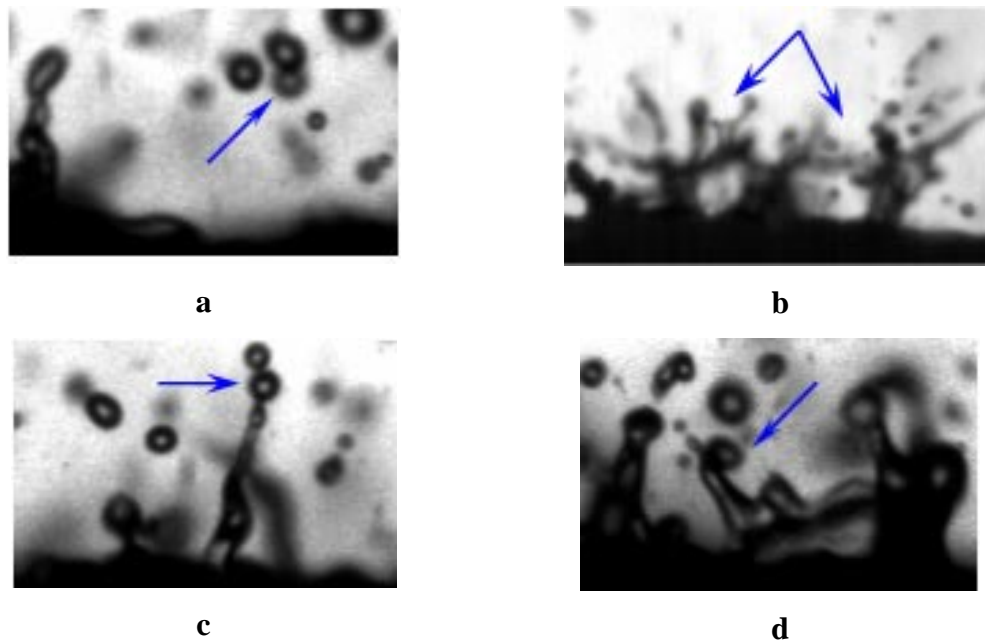


Fig. 6-1: Exemplary different source of interactions in spray between: a) two droplets, b) two splashing droplets, c) an uprising jet with a droplet and d) a splashing droplet and other droplet.

6.2. Experimental Set-up

The overall experimental arrangement used in this work is pictured in section 2 (Fig. 2-4). The water spray was created using a full jet (full-cone) nozzle with cone angle of 30° from Spraying Sys. Co., operated at pressures between 3 and 7 bar. Both flow rate and pressure were variable and measured. Four different injection angles (0, 6, 12, 18 and 28 deg.) have been used in this experiment. The aluminium target with 15 mm in diameter ($D=15\text{mm}$) was used in the conducted experiments. These oblique injection angles were measured from the spray centreline axis and the normal vector of the rigid surface (x), see Fig. 6-4a. The nozzle was placed at ($X=-20$ or -30 mm) above the target in a 10 mm off-axis from the target centreline. To characterise the spray a dual-mode phase Doppler instrument from Dantec Dynamics was used, comprising a transmitting optics with a 400mm focal length, a receiving optics with a 310mm focal length and a beam expander with an expansion ratio of 1.95, an “A” type mask in a 36° scattering angle. By using a dual-mode configuration both normal and tangential

velocity components of each individual droplet and its diameter were measured 1 mm above the target (i.e., $X = -1$ mm). The ingoing and outgoing droplets are distinguished using the sign of the velocity component normal to the target, i.e. positive u denotes an impacting droplet and a negative u denotes a secondary droplet (Fig. 6-4b). Average film thickness accumulated on the rigid wall has been measured using a high speed camera with 2000 fps.

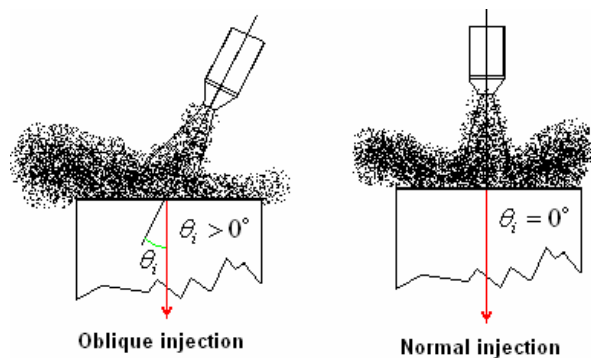


Fig. 6-2: Sketch for: a) an oblique spray and b) a normal spray impinging onto a flat-rigid surface.

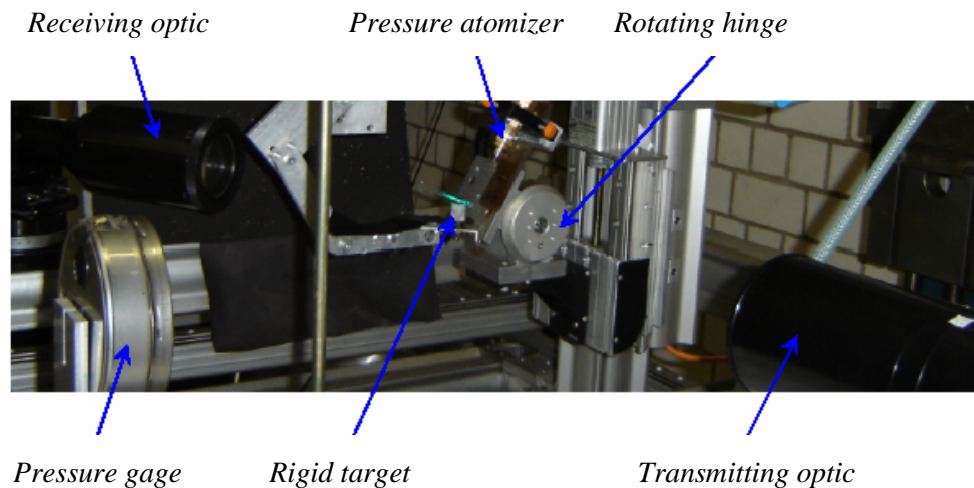


Fig. 6-3: Photograph of the experimental set-up for oblique spray impingement.

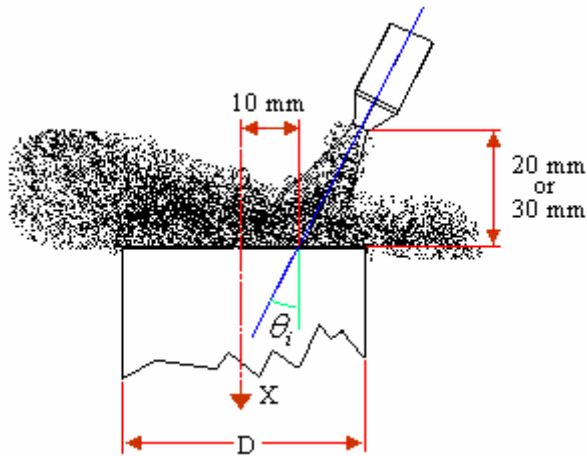


Fig. 6-4a: Coordinate and dimensions for oblique spray impingement used in this study.

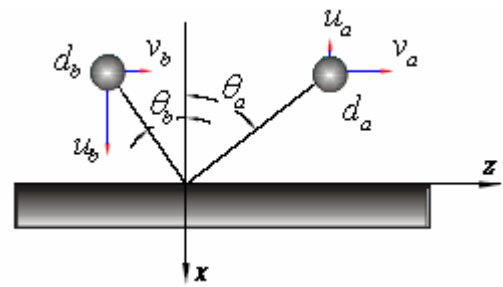


Fig. 6-4b: Coordinate system for droplets impacting the wall and secondary ejected droplets.

6.3. Result and discussion

In this study, measurement data has been obtained for a wide range of impingement conditions and impact parameters; while it is not feasible to present all of the measurement data, therefore in the following sections exemplary results will be presented in order to illustrate the behavior of the secondary spray in oblique impingement conditions.

6.3.1. Distribution of droplet size

Result of this study indicates that the average secondary to impact droplet size ratio ($\lambda_{d10} = d_{10a} / d_{10b}$) increases with increasing the injection angle (Fig. 6-5). Where d_{10a} and d_{10b} are the arithmetic mean droplet diameters of ejected droplets and impinging droplets respectively.

The average drop size ratio (secondary to impacting drop size) is plotted as a function of impact Weber number (We_{nb}) based on the normal component of velocity before the impact, in Fig. 6-6 for different injection angles together with the correlation proposed in chapter 3, as

$$\lambda_{d10} = d_{10a} / d_{10b} = -0.003We_{nb} + 1.2 \quad (6.1)$$

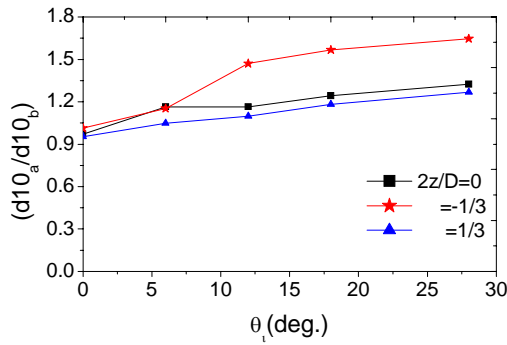


Fig. 6-5: average secondary to impact droplet size ratio ($\lambda_{d10} = d_{10a} / d_{10b}$) as a function of injection angle (θ_i).

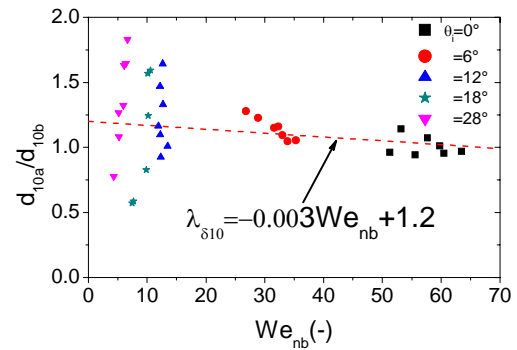


Fig. 6-6: average secondary to impact droplet size ratio ($\lambda_{d10} = d_{10a} / d_{10b}$) as a function of impact Weber number based on the normal component of impact velocity (We_{nb}).

It is shown that the average drop size ratio falls within the fairly narrow range around the given correlation line in the case of a normal injection or even with the 6° injection angle over all conducted measurements, as indicated in Fig. 6-6. This ratio, however, scatters around the correlation line for other impact conditions with the injection angles larger than 6° .

6.3.2. Distribution of velocity

The ratio of normal component of velocity after-to-before impact (u_a/u_b) is plotted in Fig. 6-7 for different injection angles as a function of measurement position above the target and for a single exemplary position of the nozzle height. These results indicate clearly that for impacts with the injection angle less than 18° , the ratio of normal component of velocity never exceeds about 0.4 for all conducted experiments. However for these angles, no significant dependency between the ratio of normal component of velocity and injection angle was observed but however this ratio falls within the fairly narrow range $0.3 < |u_a/u_b| < 0.4$ over all conducted measurements, despite the fact that the impingement velocity reached up to 8 m/s. On the other hand in the case of an impact with 28° injection angle, the ratio of normal component of velocity takes higher values than that of others.

This ratio in the later case even reaches $|u_a/u_b|=0.57$. The ratio of normal component of velocity (u_a/u_b) versus the injection angle is plotted in Fig. 6-8, indicating that the measurement points are distributed randomly around the line $|u_a/u_b|=0.4$. The tangential component of impact and ejection velocities behaves quite differently. These two correlated with one another for most cases, especially for the case of the normal injection, $\theta_i = 0^\circ$ (Fig. 6-9). For impacts with the injection angle of 6° , 12° and 18° , i.e. $6^\circ \leq \theta_i \leq 18^\circ$, ejected magnitude (v_a) exceed the impingement magnitude (v_b). Simultaneously at the same range of the injection angle ($6^\circ \leq \theta_i \leq 18^\circ$), the ratio of the normal component of the velocity (u_a/u_b) decreases for the most cases, clearly indicating that the normal momentum is partially diverted into the tangential momentum in this range of the injection angles. Any model describing the spray impingement must reflect such observations.

To compare the results presented in Fig. 6-9 with the normal impingement condition, the obtained correlation in chapter 3 for tangential velocity component is also plotted in this figure. It is shown in this figure that the results of normal injection, $\theta_i = 0^\circ$, lie under the obtained correlation. This can be explained by the larger target roughness used in this study (aluminum target) in compare with the negligible target surface roughness used in chapter 3 (polished stainless steel targets). It is found that the surface roughness dissipates the tangential momentum of the impacting droplets, see e.g. Mundo et. al. (1995).

It is maybe more interesting that the ratio of the tangential component of the velocity for after to before impact (v_a/v_b) has its maximum value in the range of $12^\circ \leq \theta_i \leq 18^\circ$ and even exceed the line corresponding to $v_a/v_b = 1$, see Fig. 6-10, whereas the ratio of normal component of velocity (u_a/u_b) decreases in this range for the most cases (Fig. 6-8). This behaviour indicates that the kinetic energy maybe converted easier from normal to the tangential component in this range of the injection angles, i.e., $12^\circ \leq \theta_i \leq 18^\circ$.

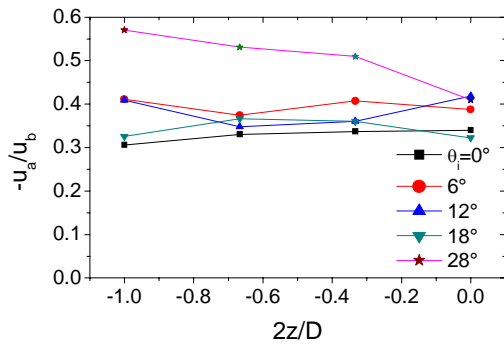


Fig. 6-7: The ratio of normal component of velocity (u_a/u_b) as a function of measurement position above the target.

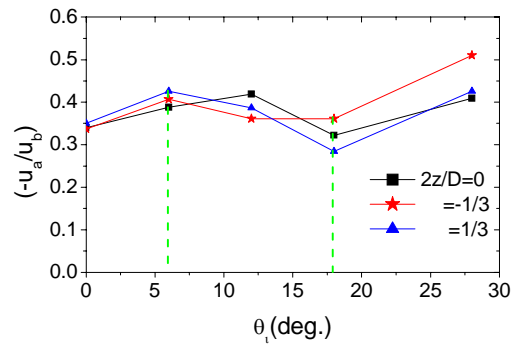


Fig. 6-8: The ratio of normal component of velocity (u_a/u_b) as a function of injection angle (θ_i).

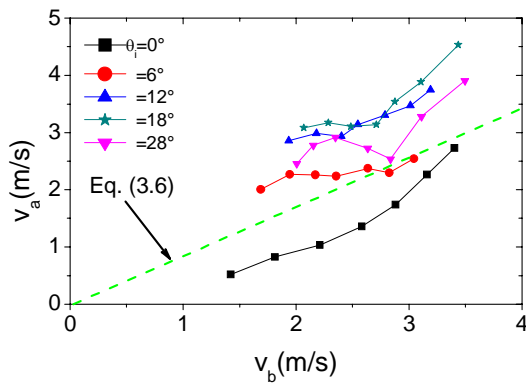


Fig. 6-9: Tangential ejection velocity of secondary droplets (v_a) as a function of impact tangential velocity (v_b) for different injection angles.

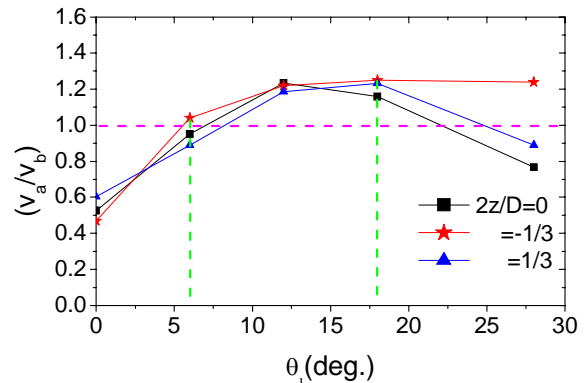


Fig. 6-10: The ratio of tangential component of velocity (v_a/v_b) as a function of injection angle (θ_i).

6.3.3. Trajectory of the secondary droplets (ejection angle of the secondary droplets)

Average values of all conducted measurements for impacts with different injection angles (θ_i) are plotted in Fig. 6-11 together with the proposed correlation for the normal injection, i.e., $\theta_i = 0$, from chapter 3 defined as

$$\theta_a [^\circ] = 0.623\theta_b [^\circ] + 41^\circ \quad (6.2)$$

Results of this study indicate that even in the case of an oblique injection, the ejection angle of the droplets (θ_a) depends strongly on the impingement angle (θ_b), see Fig. 6-11, but the injection angle of the spray (θ_i) positively increases the ejection angle of the droplets (Fig. 6-12). This is true for most of the cases except the injection angle of 28° . In the later case, the ejection angle of the secondary droplets again starts to decrease, as shown in Fig. 6-12. A linear correlation for indicating the influence of the injection angle (θ_i) can be proposed as (Fig. 6-12)

$$\theta_a [^\circ] = 1.415\theta_i [^\circ] + 53.74^\circ \quad (6.3)$$

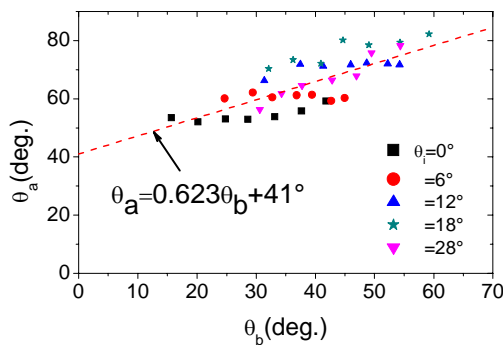


Fig. 6-11: Ejection angle of secondary droplets (θ_a) as a function of impingement angle (θ_b).

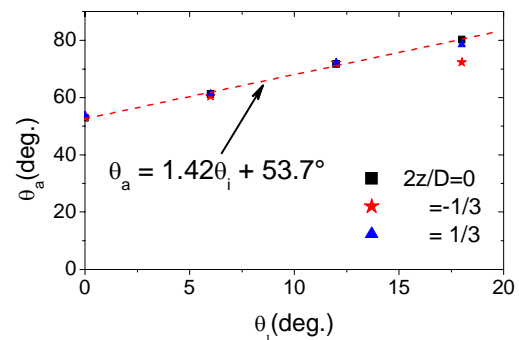


Fig. 6-12: Ejection angle of secondary droplets (θ_a) as a function of injection angle (θ_i).

6.3.4. Distribution of after impact Weber number

Distribution of the Weber number before the impact as a function of injection angle is plotted in Fig. 6-13 computed using the velocity magnitude. It is shown in this figure that the magnitude of impact Weber number significantly decreases with increasing the injection angle, due to the decrease in magnitude of the normal component of the impact velocity. The rate of such decreasing is larger for smaller injection angles, i.e., the

magnitude of the impact Weber number decreases faster for the injection angles in the range of $0^\circ \leq \theta_i \leq 12^\circ$ than that of $12^\circ \leq \theta_i \leq 28^\circ$.

The ratio of after to impact Weber number $\lambda_{We} = We_a / We_b$ is plotted in Fig. 6-14 as a function of injection angle, indicating clearly that this ratio increases with the injection angle. This relationship shows that the kinetic energy dissipation during the spray impact is larger for a normal injection or injections with smaller angles in compare with that of larger angles.

6.3.5. Distribution of secondary to incident mass and number ratios

Except the injection angle, many other complex parameters affect the total secondary to incident mass ratio ($\lambda_m = m_a / m_b$) such as droplet Weber and Reynolds numbers, relative wall roughness ($\bar{\varepsilon} / d10_b$) and relative wall film thickness ($\bar{h} / d10_b$), Kalantai and Tropea (2006). It is shown in this reference that in the case of an oblique impact ($\lambda_{Web} = We_{ib} / We_{nb} \geq 0.1$) onto a flat-rigid target, the mass and number density of the ejecting droplets decreases with increasing the impact Weber number based on the normal component of impact velocity (We_{nb}), but also the ratio $\lambda_{Web} = We_{ib} / We_{nb}$ positively influences these values.

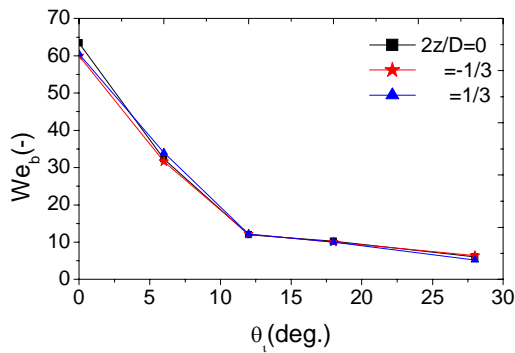


Fig. 6-13: Variation of impact Weber number with injection angle (θ_i).

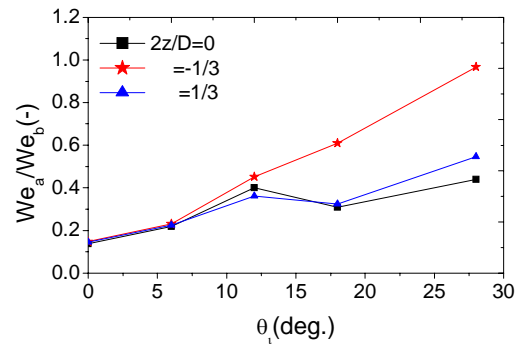


Fig. 6-14: The ratio of ejection to impact Weber number (We_a / We_b) as a function of injection angle (θ_i).

Result of this study indicates that in the case of an oblique injection onto a flat-rigid wall, total secondary to incident mass ratio ($\lambda_m = m_a/m_b$) decrease with increasing the injection angle, as shown in Fig. 6-15. This is due to the smaller impact Weber numbers for larger injection angles which yields in decreasing the number of secondary droplets, see also Fig. 6-13. Distribution of the mass ratio ($\lambda_m = m_a/m_b$) as a function of impact Weber number is illustrated in Fig. 6-16 for different injection angles, indicating the possibility of the larger mass ratios, i.e., $\lambda_m > 1$ for the normal injection. The later effect ($\lambda_m > 1$) in the normal injection only observed for large impact Weber numbers ($We_{nb} > 60$) and impact Weber number ratios larger than 0.1 ($\lambda_{Web} = We_{tb}/We_{nb} \geq 0.1$).

This means that the contribution of the wall film in the structure of the secondary spray decreases with increasing the injection angle, i.e. the number of splashing droplets or presence of multiple finger-like jets ejected from the accumulated liquid film are rare in the case of an oblique injection. Observation of such phenomena is described in more details in Cossali et al. (1997), Kalantari and Tropea (2005) and Roisman and Tropea (2005). The quantity $\lambda_N = N_a/N_b$ shows similar behavior. In the experiments reported above, the average film thickness varied in the range $\bar{h} \leq 100\mu\text{m}$.

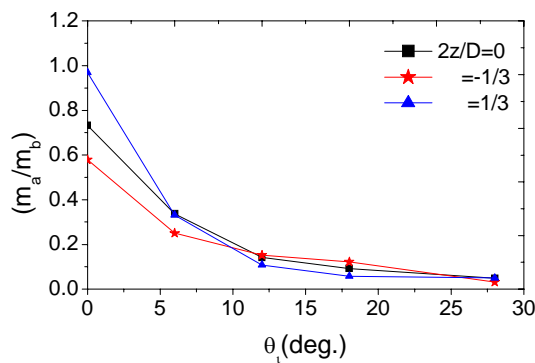


Fig. 6-15: Total secondary to incident mass ratio ($\lambda_m = m_a/m_b$) as a function of injection angle (θ_i).

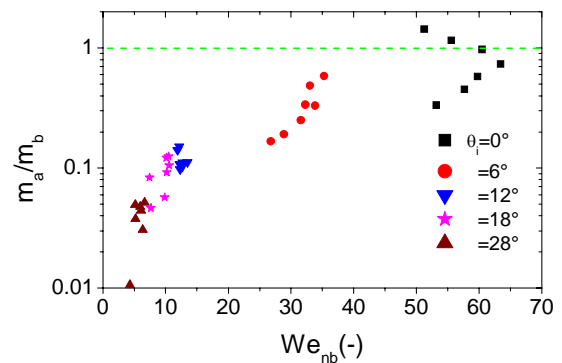


Fig. 6-16: Total secondary to incident mass ratio ($\lambda_m = m_a/m_b$) as a function of impact We number for different injection angles (θ_i).

6.4. Conclusions

From these experiments some general conclusions can be drawn about the mean statistics of ejected drop properties in dependence of impinging drop properties.

- The average drop size ratio λ_{d10} (ejection to impingement) increases with increasing the injection angle (θ_i). The average drop size ratio decreases significantly with Weber number (We_{nb}) based on the normal component of velocity before the impact in the case of normal injection or injections with small oblique angles ($\theta_i \leq 6^\circ$).
- For the chosen angles $0^\circ \leq \theta_i \leq 28^\circ$, no significant dependency between the ratio of normal component of velocity (u_a/u_b) and injection angle was observed but however this ratio falls within the fairly narrow range $0.3 < |u_a/u_b| < 0.4$ for injection angles in the range of $\theta_i \leq 18^\circ$.
- Results of this study indicate that even in the case of an oblique injection, the ejection angle of the droplets depends strongly on the impingement angle, but the injection angle positively increases the ejection angle of the droplets. This is true for most of the cases, i.e. $\theta_i \leq 18^\circ$.
- The ratio of after to impact Weber number $\lambda_{We} = We_a/We_b$ increases with the injection angle.
- In the case of an oblique injection, total secondary to incident mass ratio ($\lambda_m = m_a/m_b$) decrease with increasing the injection angle.
- Result of this study indicates the possibility of the larger mass ratios ($\lambda_m > 1$) for a normal injection. This effect was not observed for other oblique injections.

Chapter 7

7. Spray impact onto deep liquid layers: deformation of air-liquid interface, secondary spray and air bubble entrainment

In this chapter, an experimental study of liquid spray impact onto a deep liquid layer is presented. A high-speed CCD camera has been used to measure the deformation of the air-liquid film interface and the distribution of the air bubbles inside the deep liquid film. Two different configurations of a phase Doppler instrument have been used to measure drop size and two components of velocity directly above the film as well as the size and two components of velocity of the air bubbles inside the deep pool.

7.1. Introduction

Hydrodynamics of gas bubbles in a liquid flow is of importance in many technical and industrial applications, such as; cavitation damage due to collapse of gas bubbles near a rigid wall, drag reduction of submerged bodies by micro-bubble injection at the boundary layer, aeration downstream of a free discharge Howell-Bunger valve, and nuclear reactors; Esmaeeli and Tryggvason (2005), Kalantari (2002), Kuo and Wallis (1988), Leifer et al. (1999), Mahalingam et al. (1976), Moctezuma et al. (2005) and O'Connor (1995). One source of bubbles is the impact of a spray on a deep liquid layer.

In general, spray impingement on deep liquid layers is characterized by the three different structures: 1) deformation of the air-liquid film interface 2) generated secondary spray, and 3) the entrainment of the air bubbles inside the liquid film. When an inertial spray impacts onto a deep liquid film, many micron-size air bubbles are ejected and appeared inside the film. The average size of such bubbles corresponds to the average impacting droplet size in the spray. The bubbles moving downward and upward have different normal velocity components. Similar phenomenon, i.e. entrainment of many very small air bubbles, was already demonstrated by Esmailizadeh and Mesler, see e.g. Ogüz and Prosperetti (1990) and Pumphery and Elmore (1990), known as the Mesler bubble entrainment mechanism. They attributed this type of entrainment for small droplets with small impact velocities, but the impact velocities in the present case are relatively large, in the range of [6, 15] *m/s*.

Velocity fluctuations inside a liquid pool resulting from the interaction of a bubble with a vertical wall have been studied by Moctezuma et al. (2005). The movement and fluctuation of the bubbles inside the film can significantly change the heat transfer between the liquid film and the ambient gas.

The dynamics of a gas bubble in a continuous media depend on several dimensionless numbers; Reynolds number (*Re*), Eötvös number (*Eo*) and Morton number (*Mo*) defined as; $Re = \rho_l u_r d_b / \mu_l$, $Eo = (\rho_l - \rho_g) g d_b^2 / \sigma$ and $Mo = (1 - \rho_g / \rho_l) g \mu_l^4 / \sigma^3$, respectively. Here ρ_l is the density of the bulk liquid, ρ_g is density of the gas bubble, μ_l is the viscosity, σ is the surface tension, d_b is the bubble diameter, and u_r is the relative bubble velocity.

The present chapter is an experimental study of the spray impact onto a deep liquid film under various well-defined spray conditions. Characterization of different aspects of spray impact onto deep liquid films, especially characterization of the micron-size bubbles is presented.

7.2. Experimental set-up

The experimental set-up used in this work is pictured in Fig. 7-1. The spray was created using two different full-cone nozzles from Spraying System Co. and two different hollow-cone nozzles from Delevan Co., operated at pressures between 3 and 7

bar. Both flow rate and pressure during the experiments were variable and measured. A transparent box with dimensions $100 \times 100 \times 100 \text{ mm}^3$ has been used as a deep pool. The nozzles were placed at different positions above the undisturbed air-liquid film interface (see Fig. 7-2). The X coordinate of the nozzle has been varied in the range $X_{nozzle} = -20 \text{ mm}$ to -50 mm .

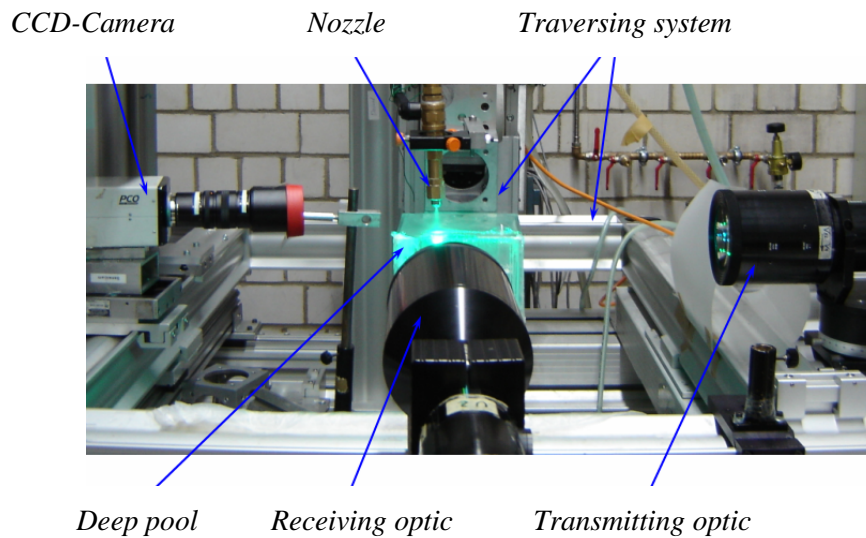


Fig. 7-1: Photograph of experimental set-up used in this study.

To characterise the spray, a dual-mode phase Doppler instrument from Dantec Dynamics was used, comprising a transmitting optics with a 310 mm focal length, a receiving optics with a 310 mm focal length, and an “A” type mask at 34° or 90° scattering angle for measuring impacting spray or air bubbles, respectively. By using a dual-mode configuration both normal and tangential velocity components of each individual droplet or bubble and its diameter were measured.

The ingoing and outgoing droplets or ejecting and rising bubbles are distinguished using the sign of the normal velocity component, i.e. positive u denotes an impacting droplet or ejecting bubble and a negative u denotes a secondary droplet or rising bubble. The overall size distributions were corrected for the size dependent detection volume cross-section using the standard system software.

Alternatively, the deformation of the air-liquid film interface has been observed

using a high-speed video system. The average deformation of the air-liquid film interface is obtained by averaging over several instantaneous images after first removing the reference interface image. Additionally, the same high-speed camera has been used to observe the distribution of the large and small air bubbles inside the deep pool, as well as the concentration of the air bubbles within the whole volume of the container.

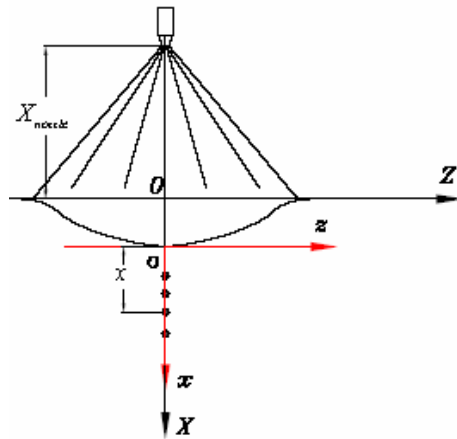


Fig. 7-2: Coordinate system for the spray and deep pool.

7.3. Results and discussion

The chapter deals with three different aspects of spray impact onto deep liquid layers:

- deformation of the air-liquid film interface due to the hydrodynamic pressure gradient exerted from impacting drops,
- the generation of a secondary spray, and
- the air bubble entrainment into the liquid film.

In the following sections, each aspect of the spray impact onto a deep liquid layer will be individually presented in more detail.

7.3.1. Deformation of air-liquid film interface under spray impact

Deformation of the air-liquid film interface in spray impact phenomenon is important for estimation of the average hydrodynamic pressure exerted from impacting drops which is one of the important integral parameters of the spray.

In the case of an inertial dominant spray impact onto a deep liquid pool, the shape of the air-liquid film interface is determined primarily by the hydrodynamic pressure exerted on the interface, defined by

$$P = P_g + P_{dyn} \quad (7.1)$$

where P_g is the pressure exerted from the ambient gas (air flow) onto the air-liquid interface and P_{dyn} is the dynamic pressure exerted from impacting droplets.

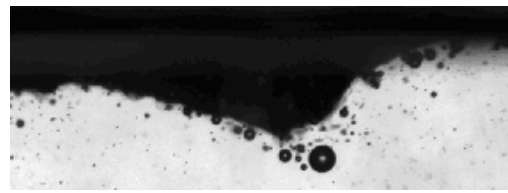
The dynamic pressure produced by the impinging droplets is the main source responsible for the surface deformation. An exemplary image of such deformation is presented in Fig. 7-3a for a given nozzle pressure and nozzle height and for different nozzle pressures in Fig. 7-3b. In this picture, results of deformation generated by a hollow-cone nozzle is presented. It is shown that the diameter of deformed interface increases with the nozzle pressure due to the increase of the spray cone angle. Moreover, increasing the nozzle pressure leads to a smoothing of the deformed interface in this picture, see Fig. 7-3b.

The dynamic pressure is the component of the momentum tensor flux density of the spray normal to the surface. In the impingement region of spray impact onto a deep pool, the dynamic pressure is generated by the momentum change of the impacting droplets. Considering the simplest one-dimensional case, the average dynamic force exerted on a surface by an impacting spray can be given by

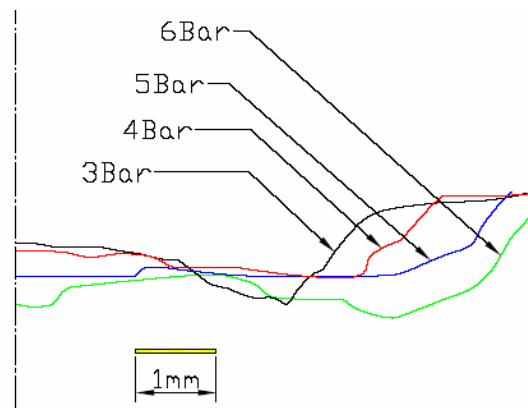
$$F_{dyn} = (m_b \cdot u_b - m_a \cdot u_a) / \Delta t \quad (7.2)$$

Defining the volume flux of the impacting drop by $q = V/t$, Eq. (6.2) can be rewritten as

$$F_{dyn} = \rho (q_b \cdot u_b - q_a \cdot u_a) \quad (7.3)$$



a



b

Fig. 7-3: a) Exemplary deformation of the air-liquid film interface due to spray impact, and b) film interface for different nozzle pressure.

In the case of a spray impact onto a deep liquid pool, some droplets rebound, most others deposit in the film, whereas some of them partially splash or generate an cylindrical ejected film after a cavity collapse, therefore a constant factor β depending on the number of rebounding or depositing droplets should be considered for dynamic pressure exerted on the wall by an impacting spray, defined as

$$P_{hyd} = \beta \cdot \rho_l \bar{u}_b \dot{q}_b \quad ; \quad 1 < \beta < 2 \quad (7.4)$$

Based on the results presented in the next section (Fig. 7-6a), it can be assumed that the normal velocity component of the secondary droplets is negligible in comparison with the normal component of the impact velocity. This means that most part of the momentum of an inertial impacting spray is transferred into the deep pool resulting in the deformation of the air-liquid film interface, velocity field and velocity fluctuations inside the film and ejection of the air flow into the liquid layer. Therefore in the case of

a normal spray impact onto deep liquid pools a coefficient value of $\beta=1$ based on the Eq. (4.12) can be considered.

An exemplary image showing the maximum deformation of the air-liquid film interface under an inertial impacting spray is illustrated in Fig. 7-4. The maximum depth, L_D , of the liquid deformation corresponds to the position where the hydrodynamic pressure is balanced by the hydrostatic pressure $\rho g L_D$.

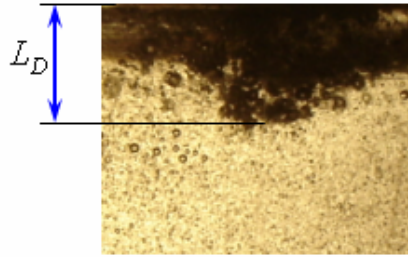


Fig. 7-4: Maximum depth of the air-liquid film interface deformation under spray impact.

Experimental results indicate that the maximum deformation of the air-liquid film interface (L_D) increases significantly with the hydrodynamic pressure of the impacting spray. This result is presented in Fig. 7-5, indicating that the maximum deformation of the film surface correlated linearly with the hydrodynamic pressure of the impacting spray, confirming the above statement. In this figure, P_{hyd} is computed applying the Eq. (6.6) to the Phase Doppler measurement results.

$$L_D = 0.001P_{hyd} - 27.14 \quad (7.5)$$

Linearity of the given expression (7.5) for estimating the maximum deformation of the air-liquid film interface under an inertial impacting spray seems to be consistent for another liquid, since the given expression for the dynamic pressure inside the (7.5) is general.

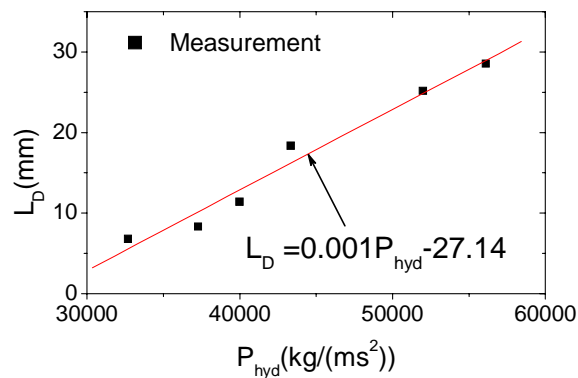


Fig. 7-5: Maximum air-liquid film interface deformation as a function of hydrodynamic pressure exerted from impacting spray.

7.3.2. Formation of the secondary spray due to spray impact onto deep liquid layers

The distribution of droplets in the impacting spray (the diameter and two velocity components) has been characterized using the phase Doppler instrument. The detection volume has been located above the water surface. The primary and secondary droplets are distinguished by the sign of the normal-to-the-surface velocity component. The same experimental method is used as in the study of spray impact onto a rigid wall; Tropea and Roisman (2000) and Panão and Moreira (2005).

Normal and tangential velocity components before and after impact are illustrated in Fig. 7-6a, and b for a low impact velocity condition. Note that in the case of a high inertial impact condition, i.e. high impact velocities, measurement of the secondary spray exactly above the interface was difficult. Results of this study indicate that the normal velocity component of the ejected droplets is very poorly correlated with the normal component of impingement velocity (Fig. 7-6a). On the other hand the tangential component of the ejection and impinging velocities relatively correlated with one another (Fig. 7-6b). In this case the ratio of tangential component of velocity after to before impact (v_a / v_b) is about half of this ratio for spray impact onto rigid walls.

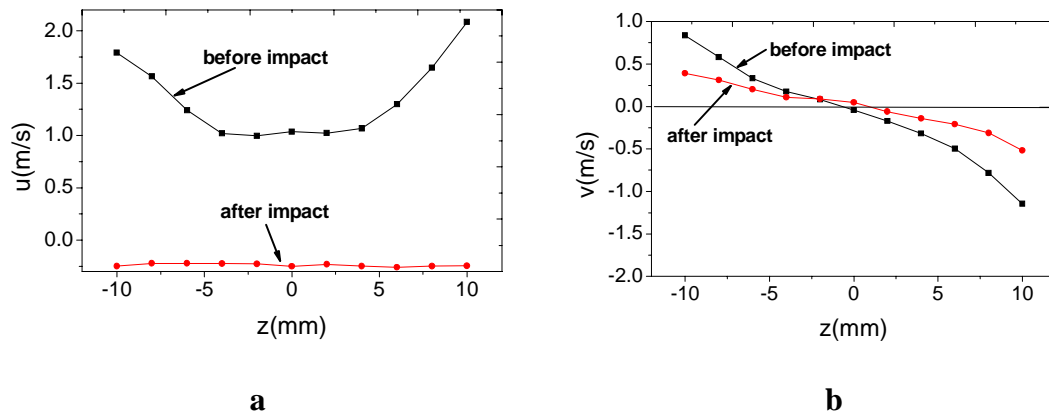


Fig. 7-6: Comparison of droplet velocity before and after impact, a) normal component, b) tangential component.

7.3.3. Air bubble entrainments due to spray impact onto deep liquid layers

Another aspect of air bubble entrainment in liquid film has been distinguished during the measurements; entrainment of many very small micron size air bubbles in the deep part of liquid films distributed in a cone shape (Fig. 7-7b). Note that these bubbles cannot be seen by illumination of the film with a normal light, as shown in Fig. 7-7a. A close-up view of such bubbles is presented in Fig. 7-8 for an exemplary nozzle height and a given depth of the liquid film for different atomizing pressure. These exemplary results indicate that the number of bubbles (bubble concentration) increases significantly with the atomizing pressure, i.e. impact Weber number.

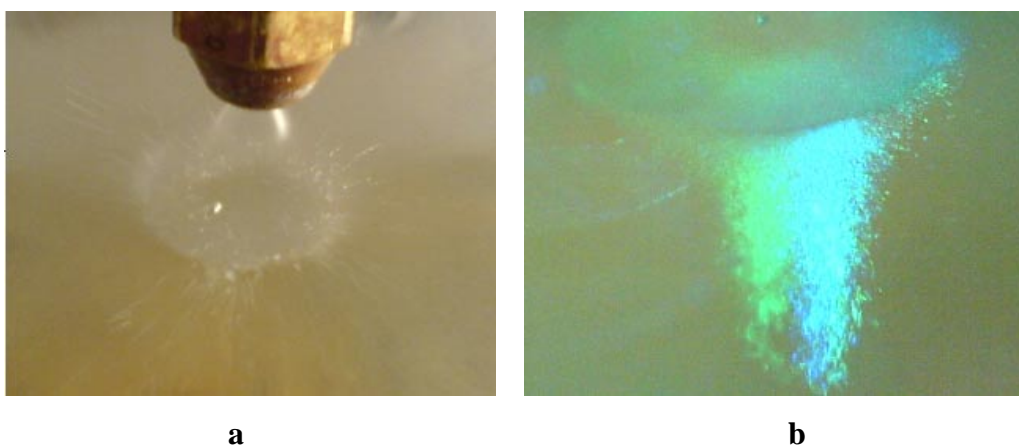


Fig. 7-7: Spray impact onto deep liquid film, a) illuminated by normal light, and b) illuminated by laser light.

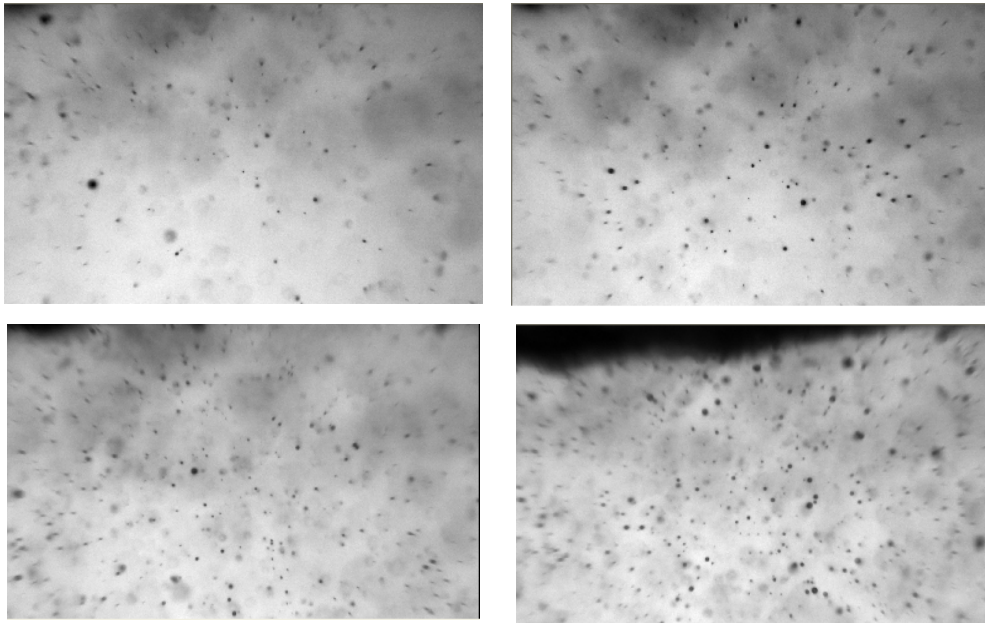


Fig. 7-8: Close-up view of the variation the number of bubbles inside the deep liquid layer under spray impact for different nozzle pressure a) 3 bar, b) 4 bar, c) 5 bar, and d) 6 bar.

Results obtained in this figure clearly indicate that mechanism of the air bubble entrainment by a spray impact, i.e. impact of multiple micron-size droplets with high velocity, differ significantly with the mechanism of bubble formation due to the cavity collapse in a single drop impact onto a deep liquid layer, since in the case of spray impact, the size of the air bubbles and impacting droplets fall in the same range (the same order of magnitude), whereas in the case of a single drop impact, the size of the air bubble is much smaller than the size of impacting droplet.

The mechanism of drop impact and the subsequent bubble entrainment is explained in the study Glasheen and McMahon (1996). In this experimental work the impact and penetration of a rigid disc has been visualized. Such impact leads to the creation of a cavity, its collapse and creation of a bubble.

With this assumption, the similarity of the bubble size with impacting droplets can be explained. The average size of these bubbles mostly falls in the range $[25, 45] \mu m$ under the nozzle exit centreline ($z=0$) independent of the film depth, despite the fact that the mean size of the impacting droplets varies in the range $30 \leq d_{10b} \leq 40 \mu m$.

These micron size bubbles move with very small velocities inside the film, of the order of $O(10)$ cm/s for ejected bubbles and $O(1)$ cm/s for upward rising bubbles.

The number concentration of the air bubbles at each measurement point inside the film depends on the mass flow rate of the air entering into the liquid medium, which depends on the number concentration of the impacting droplets. Results show that the number of air bubbles inside the film increases significantly with the atomizing pressure (Fig. 7-8). Larger bubbles are formed close to the air-film interface, see Fig. 7-3a.

Probability density distributions of the bubble size (*pdf*) for different impact Weber numbers are presented in Fig. 7-9a, b, c, and d. In these figures bubble count at each bin (bubble size class) is normalized by the total bubble count. It is interesting that the normalized *pdf* of the bubble counts presented in Fig. 7-9 is independent of the impact Weber number, i.e. these *pdfs* have the same mean value and same range. On the other hand, these *pdf* distributions are very similar to the *pdf* distribution of the impacting droplets.

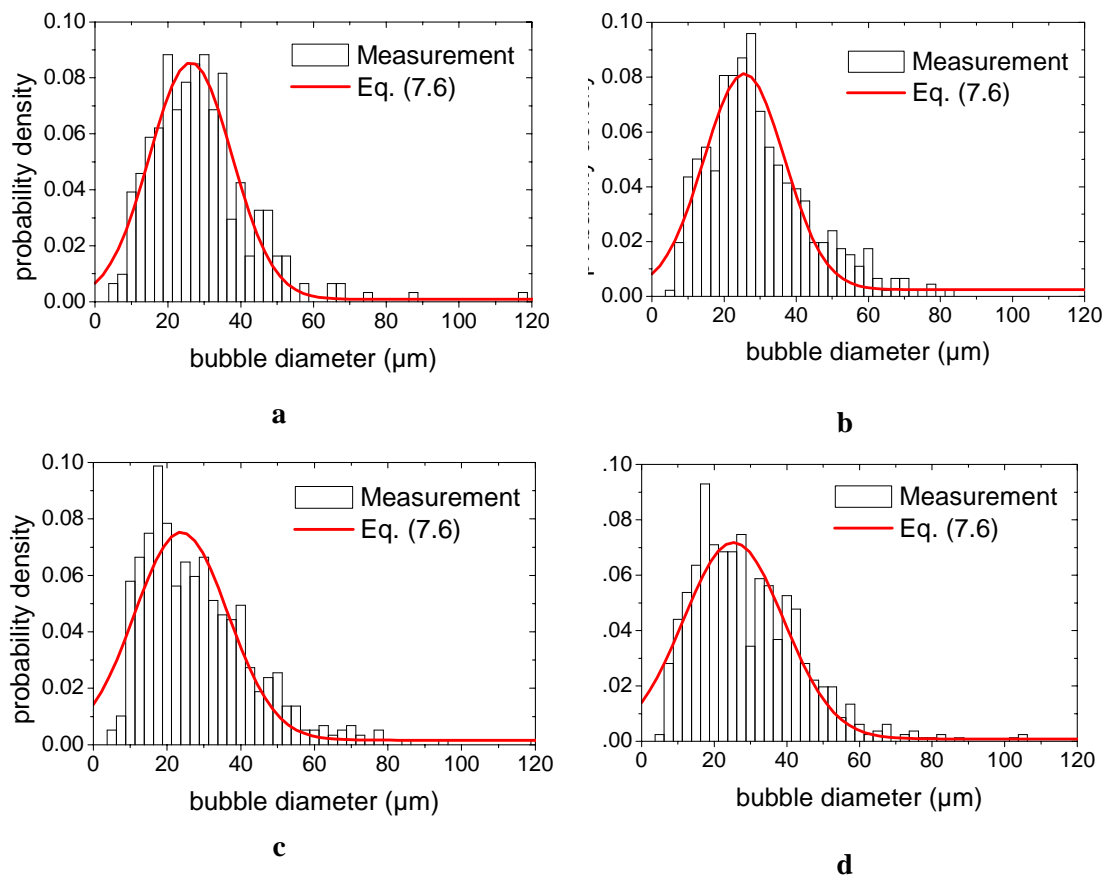


Fig. 7-9: Probability density of air bubbles diameter for different impact condition; $X_{nozzle} = -40$ mm, $x = 20$ mm, a) $We = 36.7$, b) $We = 44.5$, c) $We = 52.8$, and d) $We = 60$.

The probability density distribution of the bubble size normalized by the total bubble count ($N_{b-total}$) can be expressed by a Gaussian distribution function defined as

$$N_b / N_{b-total} = A_0 + \frac{A_1}{\sigma_b \sqrt{\pi/2}} \exp \left[-2 \frac{(d_b - \bar{d}_b)^2}{\sigma_b^2} \right] \quad (7.6)$$

where N_b is the bubble count per bin, $N_{b-total}$ is the total bubble count during the acquisition time, \bar{d}_b is the average bubble size, σ_b is the standard deviation of the bubble size and A_0 and A_1 are constant values.

The constant coefficients A_0 and A_1 fall within the range $8.7 \times 10^{-4} \leq A_0 \leq 2.4 \times 10^{-3}$ and $2.21 \leq A_1 \leq 2.45$, respectively for conducted measurements in this study. Total bubble count during the acquisition time defined as

$$N_{b-total} = f_b \cdot t_{aq.} \quad (7.7)$$

where f_b is frequency of the air bubbles at each measurement point and $t_{aq.}$ is the total acquisition time.

Note that the observed frequency of the air bubbles at a given measurement point (7.10) depends also on the measurement volume size. In the bubble measurements with 90° scattering angle, size of the measurement volume depends only on the measurement volume diameter. The reference area of the nominal measurement volume in x-direction was $A_{0-x} = 6429 \mu\text{m}^2$ in the conducted bubble measurements in this study using a 90° scattering angle. This value can be considered for normalizing the observed frequency of the bubbles passing the measurement point for future researches, e.g., the form of f_b/A_0 can be considered to compare the different results.

Results indicate that the frequency of moving bubbles at each measurement point increase with the atomizing pressure, i.e. impact Weber number, see Fig. 7-10. A simple correlation for the frequency of bubbles passing the measurement point as a function of impact Weber number and depth of film is obtained as

$$f_b = a_1 \ln(We_b) + a_2 x + a_0 \quad (7.8)$$

where a_1 , a_2 , and a_3 found to be: 6.534, -0.0366, and -21.5, respectively.

A physical explanation for such behaviour (7.8), i.e, influence of the average impact Weber number on the frequency of bubble entrainment, can be explained by the regular bubble entrainment region in the $We-Fr$ diagram obtained by Pumphery and Elmore (1990), see Fig. 7-11. It is shown in this figure that the regular bubble entrainment can only be observed for $We > 50$ in the case of a single drop impact. Region of the regular bubble entrainment then increases with increasing the impact Weber number in this figure, e.g. bubble entrainment region at $We = 150$ is wider than that of $We = 100$. The same behaviour can be obtained from (7.8) or Fig. 7-10, indicating that the frequency of bubble observation increases with the impact Weber number.

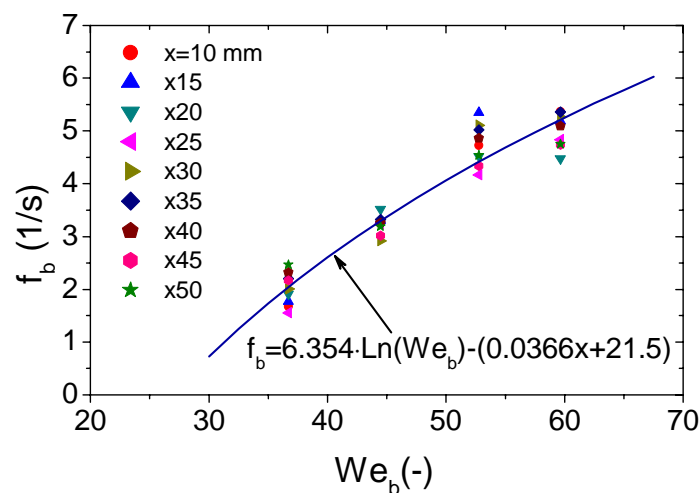


Fig. 7-10: Frequency of bubble count as a function of impact Weber number for different depth of fluid.

This correlation is obtained for the normal spray impact condition; $\lambda_{We_b} = We_{tb} / We_{nb} < 0.1$, flux density of impacting spray in the range $0.6 \leq \dot{q} \leq 3.5 \text{ m/s}$, mean impacting drop size in the range $30 \leq d_{10b} \leq 40 \mu\text{m}$, and depth of fluid in the range $10 \leq x \leq 50 \text{ mm}$ under the centreline of the nozzle exit.

The observation of greatly reduced bubble count inside the liquid film (in the range of Hz) in comparison with the higher frequency of the impacting droplets (in the range of kHz) suggests that each impacting droplet doesn't generate a bubble, and there should be a combination of droplet size and droplet velocity together with the physical

properties of the fluid, i.e. impact Weber or Reynolds number, which yields generation of an air bubble entrainment under the impacting spray. Such diagram can be obtained in Pumphery and Elmore (1990) and Ogüz and Prosperetti (1990), see also Fig. 7-11.

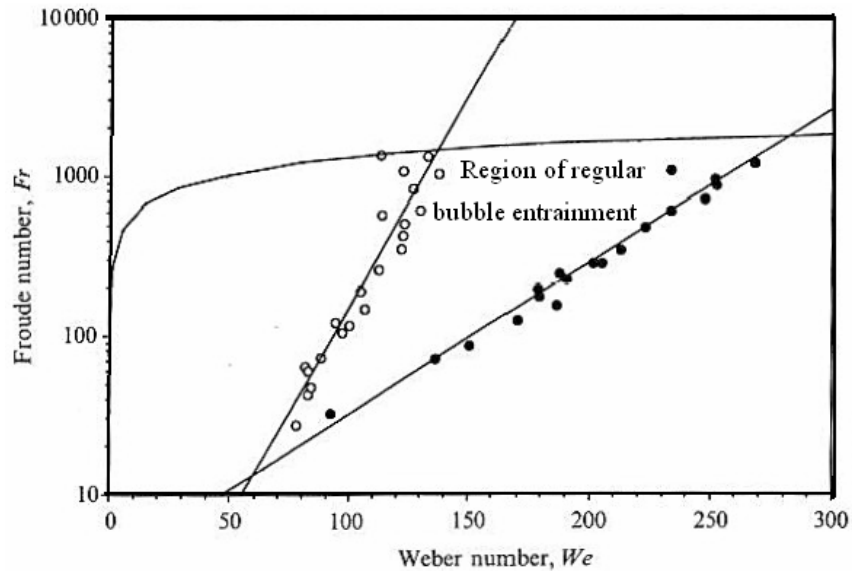


Fig. 7-11: Region of regular single bubble entrainment in the We - Fr diagram, Ref: Pumphery and Elmore (1990),

Other results illustrated in Fig. 7-12 indicate that the bubble count decreases significantly with the film depth at any off-axis measurement point ($z=10$ mm in this figure). Such an observation can be also be made from the photograph of the air bubbles inside the film, as presented for an exemplary case in Fig. 7-7b.

The average size of the ejecting bubbles, i.e. bubbles moving downward, as a function of the film depth, is presented in Fig. 7-13 for different impact Weber numbers. Results presented in this figure indicate that the average bubble size is independent of the film depth and the impact Weber number. However in this figure, the average bubble diameter scatter around the line $d_b=32$ μm , and mostly falls in the range 25 $\mu\text{m} \leq d_b \leq 45$ μm , as illustrated in Fig. 7-13.

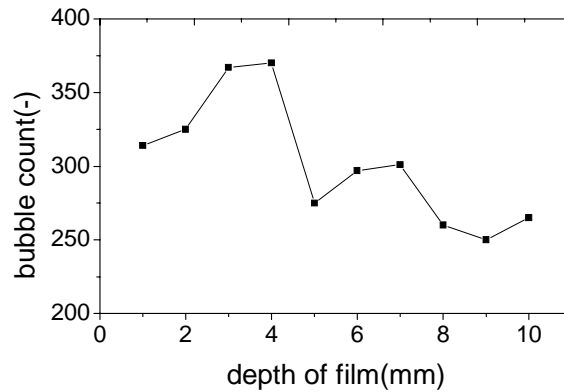


Fig. 7-12: Variation the bubble count as a function of the film depth at 10 mm off-axis from the nozzle exit centerline.

Results obtained in this work indicate that the bubble size distribution is very close to the impacting drop diameter distribution; therefore they have approximately the same average value, i.e. $d_b \approx d_{10b}$. In the Fig. 7-13, the average size of impacting droplets falls in the range $30 \mu\text{m} \leq d_b \leq 40 \mu\text{m}$.

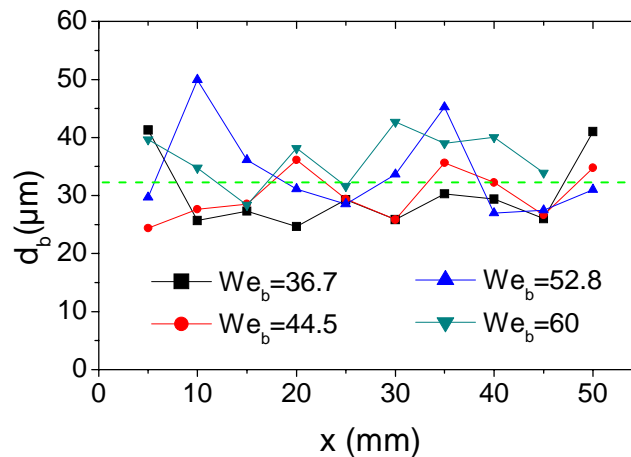


Fig. 7-13: Variation the average bubble size with film depth for different impact Weber numbers.

Results obtained in this study indicate that the rising and ejecting bubbles have approximately the same mean size. An exemplary of such measurement is presented in Fig. 7-14 for the normal spray impact condition with the impact Weber number $We_b=34.8$, $x=50 \text{ mm}$, and $z=0$.

The bubble motion inside the deep liquid layer under influence of the impacting

spray is determined based on the Lagrangian approach by a combination of different forces acting on the bubble:

- Buoyancy force (F_B)
- Virtual mass fore (F_{VM})
- Pressure gradient force (F_P)
- Drag force (F_D)
- Shear induced lift force (F_L)

The constant rise velocity of a single bubble in a stationary liquid can be estimated by the balance of the drag force $F_D = 0.5C_D A_b \rho_l u_r^2$, and the buoyancy force $F_B = (\rho_l - \rho_b)V_b g$ applied to the bubble. In these equations ρ_b and ρ_l are the air bubble and liquid density, respectively, V_b is volume of spherical bubbles defined as $V_b = \pi d_b^3 / 6$. C_D is the drag coefficient of a single gas bubble moving inside the liquid medium, given by: $C_D = 16/Re_b$ for $Re_b < 0.49$ and $C_D = 20.68 Re_b^{-0.643}$ for $0.49 < Re_b < 33$, Kuo and Wallis (1988). The results of these estimations are shown in Table 7-1.

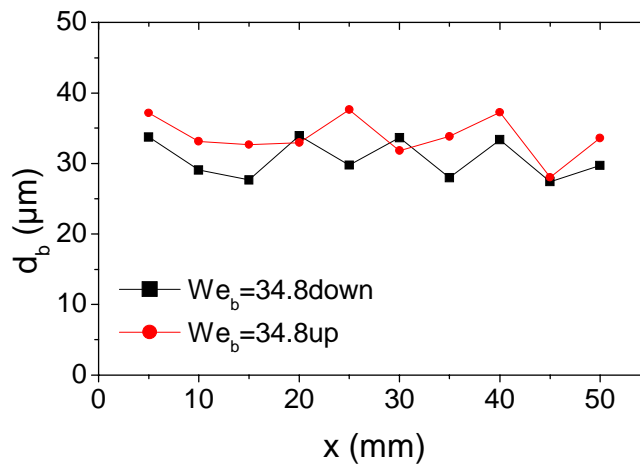


Fig. 7-14: Variation the average ejecting (bubbles moving downward) and rising bubbles (moving upward) size with film depth.

Table 7-1: Air bubble rise velocity as a function of bubble size in a stationary water pool.

Bubble size (μm)	20	50	100	200	500
Bubble rise velocity (cm/s)	0.03	0.2	0.55	1.52	5.78

Results presented in Fig. 7-15a and b for the velocity of ejecting and rising bubbles deviate extremely from the rise velocity of the bubbles in a stationary deep water pool, as presented in Table 7-1. The main sources of the discrepancy are in the motion of the bulk liquid generated by the spray impact and by the interaction of the rising bubbles. It is also known that the rising velocity of a single bubble depends on its diameter. For example, in the case of a very small air bubble, i.e. $Re_b < 0.49$, the bubble rising velocity is proportional to d_b^2 , or for larger bubbles the rising velocity is proportional to $d_b^{1.459}$, see also Kuo and Wallis (1988) and Leifer et al. (1999). But the results of phase Doppler measurements conducted in this study indicate that the velocity distribution of the bubbles does not depend on the diameter. This means that they behave not like an array of single bubbles but as a cloud of bubbles.

An estimation for the rise velocity of the cloud of small bubbles in a water film is given in Oliemans (2005) in the form

$$u_b = 1.53 \left[\frac{\sigma \cdot g (\rho_l - \rho_b)}{\rho_l^2} \right]^{1/4} \quad (7.9)$$

This formula predicts the bubble rise velocity to be approximately 25 cm/s. It is interesting that this velocity is equal to the difference between the measured velocity of the entrained bubbles (which is probably comparable with the liquid velocity) and the velocity of the rising bubbles.

Meanwhile a complex term for variation of the drag coefficient in the case of multiple bubbles movement must be considered, since the expressions for drag coefficients used

in Table 7-1 have been obtained for a single bubble rising in a stationary liquid and variation of the drag coefficient for multiple bubble movements is not considered in these expressions, e.g. variation of the drag coefficient due to interaction of the wakes formed behind the moving bubbles must be taken into account.

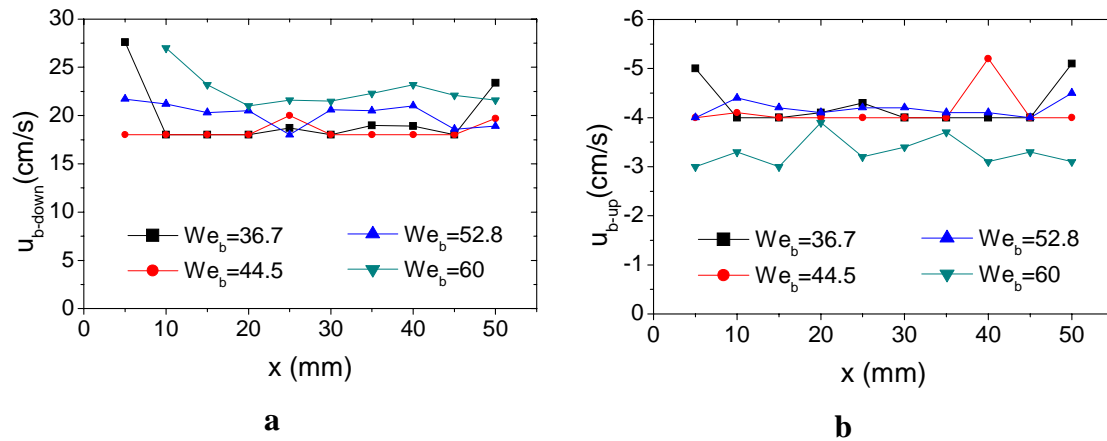


Fig. 7-15: Variation the average a) ejecting bubble velocity, and b) rising bubble velocity, with film depth for different impact Weber numbers.

Results obtained in this study indicate that in contrast to the bubble size distribution, the velocity distribution of the bubbles does not exhibit a wide distribution range. This result indicates that the bubble motion inside the deep film under spray impact condition is mostly influenced by the hydrodynamic pressure inside the film and not by the bubble size.

An exemplary image showing the high concentration region of the air bubbles inside the deep pool (Fig. 7-4b) indicates that the air bubbles concentrate around the axis of symmetry (x-axis) instead of dispersing throughout the entire liquid container. This observation is consistent with the tangential velocity component presented in Fig. 7-16. The result presented in this figure indicates that after a certain film depth inside the liquid pool, i.e. $x=25\text{ mm}$ in this figure, the tangential velocity component of both ejecting and rising bubbles vanishes, whereas their normal velocity component doesn't change significantly, see Fig. 7-15a and b. Therefore after a certain film depth, most of the bubbles lose their tangential velocity component and concentrate around the vertical axis. A reliable answer to this behaviour remains still open for future research.

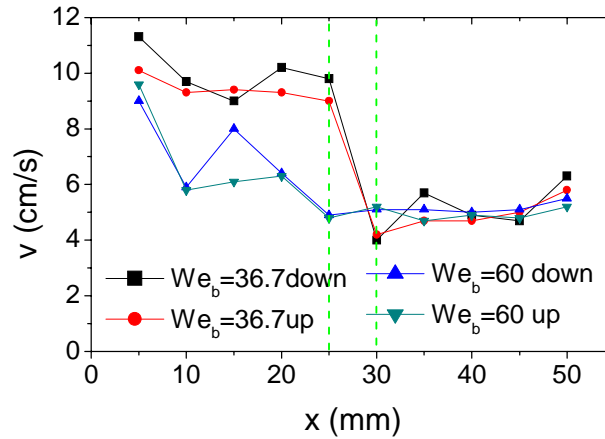


Fig. 7-16: Variation the average ejecting and rising bubble velocity with film depth for two different impact Weber numbers.

However one possible hypothesis can be explained by the radial flow of the liquid induced by spray impact, as well as by the induced shear lift force acting on the bubbles in the radial direction (z-direction), i.e. perpendicular to the main flow direction, due to the velocity gradient on two sides of the air bubbles (Fig. 7-17), expressed as.

$$F_L = C_L A_b \rho_l \vec{u}_r \times (\vec{\nabla} \times \vec{u}_l) \quad (7.10)$$

where C_L is the shear lift coefficient, assumed to be $C_L \approx 0.25$ in this study.

The direction of this vector is toward the higher velocity field, i.e. lower pressure side, as illustrated in Fig. 7-17. This force concentrates more bubbles around the vertical axis instead of dispersing them throughout the flow, as shown in Fig. 7-7b.

7.4. Conclusions

This chapter presents an experimental study for different aspects of liquid spray impact onto a deep liquid layer under the well controlled experimental conditions. The maximum deformation of the air-liquid film interface correlates well with the computed value of the hydrodynamic pressure exerted onto the film interface by an impacting spray.

Results obtained in this study indicate that the average bubble size does not change significantly with the film depth and seems to be correlated with the average diameter of the impacting droplets.

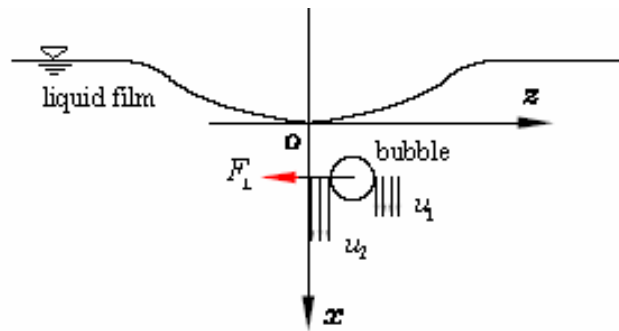


Fig. 7-17: Shear lift force acting on an air bubble moving inside continuous liquid film under spray impact.

Other results indicate that the impact Weber number has most influence on the frequency of the bubble formation, i.e. bubble concentration, but has no significant influence on the average bubble size or bubble size distributions.

The normal velocity component of the rising bubbles under influence of the impacting spray differs significantly from the computed rise velocity of the air bubbles inside a stationary liquid film. Based on the results obtained in this study, the normal velocity component of the rising or ejecting bubbles doesn't change significantly with the film depth, whereas the tangential velocity component changes significantly after a certain film depth. A shear induced lift force has been introduced for this effect.

The phase Doppler measurements indicate that the rising velocity of the bubbles does not depend on the bubble diameter. We explain this behaviour by the interaction of the bubbles in the cloud.

As illustrated above, the mean measured ejecting and rising bubble size varied in the range $20 \mu m < d_b < 50 \mu m$, corresponding to an impingement Weber number in the range $30 < We_{nb} < 80$ based on the normal velocity component, and mean impact droplet size in the range $30 \mu m < d_{10b} < 40 \mu m$.

Chapter 8

8. Conclusion and Outlooks

In this chapter, summary of main achievements and findings in this research work are presented and some suggestions are proposed for future works and further researches, based on the results obtained in this study.

8.1. Conclusion and main achievements

Main results and achievements of this study are presented in the previous chapters, i.e., chapter 2-7. In the following points, main achievements and conclusions are listed.

- The performed literature review and survey, regarding characterization of the secondary spray, accumulated wall film and splashing droplets in isolation and in a spray. This part of work is distributed throughout different chapters based on the subject of each chapter.
- The empirical model for characterization of the secondary spray. The foregoing survey of literature and phenomenological characterization of spray impact leads us to two fundamental conclusions: Modeling spray impact must consider also the presence and influence of the accumulated wall film; Models based solely on the impact of single droplets will miss many essential elements of spray impact. These conclusions are motivation to formulate models derived from spray impact data obtained under controlled boundary conditions; hence also the motivation to perform such experiments. The novel aspect of the model is that the correlations are based

- on the mean statistics over many events in spray and not on the outcome of single drop impact experiments. Other interesting feature of the experiments is the rather large range of oblique impact angles captured, due to the different drop trajectories exiting from the spray.
- Characterization of the wall film and the proposed theoretical model for prediction the average thickness and velocity of the accumulated wall liquid film formed by impinging spray. In this part of work, the experimental results are complemented by theoretical expressions regarding the hydrodynamics of liquid films under sprays and preliminary models for the average wall film thickness and secondary spray are formulated.
- Characterization of splashing droplets in isolation and in a spray. In this part of work, a fundamental comparison of the splashing phenomenon for single drops and for drops in a spray is presented. Such comparison can be very valuable for future modeling of spray impact. The present work provides such a comparison experimentally, followed by a derived theoretical model.
- Characterization of spray impact onto deep liquid layer. This part of present work is an experimental study of the liquid spray impact onto a deep liquid film under various well-defined spray conditions. Characterization of different aspects of spray impact onto deep liquid films, especially characterization of the micron-size bubbles is presented.

8.2. Outlook and useful suggestions for future works

In the present work, some different aspects of splashing droplets under spray impact conditions is presented and compared with those characteristics in isolation, i.e. single liquid drop impact onto thin liquid films obtained by Cossali et al. (1997). It is shown in this work that characteristics of splashing droplet in a spray impact condition are significantly different from those of splashing droplets in isolation. It has been qualitatively found in this study that the velocity field and velocity fluctuations inside the wall film are the main reason for such differences, but more extensive and precise works are still necessary to characterize these differences, quantitatively. This is the main reason for a further research to measure precisely the

velocity field and velocity fluctuations inside the accumulated wall film. Further developments in modelling of spray/wall interaction phenomena require such information.

Some of the observation and open questions in this area are listed below:

- Obtained growth rates for crown base radius and crown height for a splashing droplet in a spray are significantly different than that of a single or train of single droplets impacting onto an undisturbed liquid layer, proportional to $t^{0.5}$.
- Maximum non-dimensional crown height in the case of splash in spray is significantly higher than that of splashing droplet in isolation.
- Splashing droplets in spray impact conditions are non-symmetric and more irregular in compare to very symmetric splash in isolation; this can be due to oblique impact of droplets in spray, wavy form of the air-liquid interface, impact of another droplet close to the splashing droplet.
- Number and size distribution of generated secondary droplets by splash in a real spray impact condition. This is a very hard but important question, since even in the case of splashing droplet in isolation number and size distribution of generated secondary droplets by splash vary in time and is not a constant value during the time history of splashing droplet. More complexity is due to non-symmetrical development of splash in spray impact condition, which generates non-symmetric size and number distribution of secondary droplets.
- Contribution of the finger-like ejected wall film jets in generation of secondary droplets in spray impact conditions. Our observations show that the frequency of such ejected jets from the accumulated wall film increase with increasing the flux density of impacting droplets in the case of a highly inertial impact conditions and can therefore be very important in generation of the secondary droplets in Diesel injection systems. The frequency of such jets and number, size and velocity distribution of generated secondary droplets by these jets can be a new challenge in spray/wall interaction phenomena.

- Influence of the velocity field and velocity fluctuations inside the wall film on characteristics of generated secondary spray. Influence of the film thickness in spray/wall interaction extensively has been studied in this work and two different models for prediction of average accumulated wall film thickness have been derived in this study. However one of these models is able to predict the average velocity of the spreading wall film, but velocity fluctuations inside the wall film and its influence on the characteristics of the generated secondary spray is still an open question in this research area.

Appendix I

I. Summary of previous models for single drop and spray impact

In the following section a summary of the some previous models for spray impact and single drop impact is presented.

I.1. Velocity of the ejected (secondary) droplets

Based on the work of Wang and Watkins (1993), for $We < 30$ only a rebounded droplet is observed. They also found that for $30 < We < 80$, the primary drop will break-up in two or three smaller drops rebounding from the wall. Based on their model, splash takes place for $We > 80$. This model for the normal and tangential velocity components of a rebounded droplet and its diameter for $We < 80$ gives

$$u_a = \kappa \cdot u_b, \quad v_a = -\kappa \cdot v_b \quad (\text{I.1a, b})$$

where $\kappa = \sqrt{1 - 0.95 \cdot \sin^2 \theta_b}$.

$$d_a = d_b \quad (\text{I.2})$$

$$N_a = 1 \quad (\text{I.3})$$

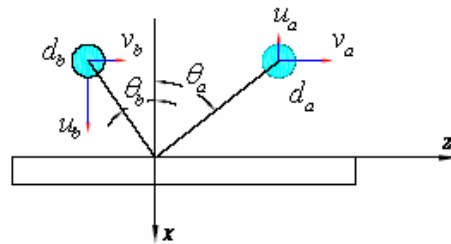


Fig. I-1: Nomenclature for impinging and ejecting droplets from wall.

The empirical model of Bai and Gosman (1995) based on the results of single drop impact gives other expressions for the velocity of a rebounded droplet in the form of

$$u_a = 0.714 \cdot u_b, \quad v_a = \xi \cdot v_b \quad (\text{I.4a, b})$$

where $\xi = 0.993 - 1.7\theta_b + 1.56\theta_b^2 - 0.49\theta_b^3$; (θ_b in rad) (I.5)

Bai and Gosman (1997) considered that the impact energy imparted to the disintegration process of a splashing event is due mainly to the normal incident velocity, while the tangential velocity transfers a portion of its tangential momentum to each secondary droplet.

$$v_a = C_f \cdot v_b \quad (\text{I.6})$$

where v_a is the tangential velocity component of the splashing droplets, v_b is the tangential velocity component of the incident droplet and C_f is a friction coefficient. Based on the experimental evidence, C_f falls in the range of [0.6,0.8].

According to the model of Marengo and Tropea (1999), normal and tangential velocity components of the secondary droplets generated due to single water droplets impacting onto a liquid film for the condition of $\theta_b < 10^\circ$, $0.5 < \delta < 2$ and $K < 4000$ are (δ in this model represents the dimensionless film thickness $\delta = h_0/d_b$):

$$u_a^* = (0.056 + 0.057\delta) + 0.038 \cdot 10^{-3} (K - K_{Cr}) \quad (\text{I.7})$$

$$v_a^* = (0.311 - 0.077\delta) - (0.009 + 0.024\delta) \cdot 10^{-3} (K - K_{Cr}) \quad (\text{I.8})$$

where $u_a^* = u_a/u_b$, $v_a^* = v_a/u_b$ and $K = We \cdot Oh^{-0.4}$.

The model of Mundo et al. (1994) gives the following expressions for the normal and tangential velocity components and diameter of the secondary droplets generated due to single droplets impacting onto a rigid wall. In this study a rotating disk was used as a rigid wall in order to generate a tangential velocity component for a normal impacting droplet.

$$u_a = \left[1.337 - 1.318 \left(\frac{d_a}{d_b} \right) + 2.339 \left(\frac{d_a}{d_b} \right)^2 \right] \cdot u_b \quad (\text{I.9})$$

$$v_a = \left[-0.249 - 2.959 \left(\frac{d_a}{d_b} \right) + 7.794 \left(\frac{d_a}{d_b} \right)^2 \right] \cdot v_b \quad (\text{I.10})$$

$$d_a = \min [8.72 \exp(-0.0281K), 1.0] \cdot d_b \quad (\text{I.11})$$

I.2. Ejection angle of the secondary splashing droplets

The properties of secondary splashed droplets appear to depend strongly on the ejection time. For early ejected droplets, the ejection velocity and angle are larger. Meanwhile, size of the ejected secondary droplets from a splashing crown increases from a minimum value to the maximum during the ejection phenomena. Some available models for the ejection angle (for water droplets) are:

- Impact onto a smooth and rigid wall with a mean surface roughness of $0.83\mu\text{m}$, Mutchler (1970):

$$\theta_a \in [5^\circ, 50^\circ]$$

- Impact onto a deep liquid pool, Allen (1988):

$$\theta_a \in [30^\circ, 70^\circ]$$

- Impact on a rough soil surface, Ghadiri (1978):

$$\theta_a \in [5^\circ, 50^\circ]$$

Stanton and Rutland (1996) found the ejection angle of the secondary droplets depending on the incident angle of the primary droplets in the form of

$$\theta_a = 0.266\theta_b + 65.4^\circ \quad (\text{I.12})$$

The rebound angle based on an empirical curve fit to the data of Mundo et al. (1995) is

$$\theta_a \cong 0.316\theta_b + 62.24^\circ \quad (\text{I.13})$$

I.3. Total splashing-to-incident mass and number ratio

$$(\lambda_m = m_a/m_b, \lambda_N = N_a/N_b)$$

Total splashing-to-incident mass ratio is a complex function of several parameters such as:

- droplet We number,
- droplet Re or La number,
- wall roughness and
- wall film thickness.

Based on experimental observation for single drop impact, λ_m takes a random value in the range $[0.2, 0.8]$ for a dry wall and $[0.2, 1.1]$ for a wetted wall, Bai and Gosmn (1995). According to previous work, no general correlation is available for the total splashing-to-incident mass and number ratio.

The total mass of the splashing droplets can be estimated by using an empirical correlation obtained by Senda et al. (1994) and Yarin and Weiss (1995)

$$\frac{m_{sp}}{m_b} = \begin{cases} 0.0, & \dots \dots \dots We < 80 \\ 0.5, & \dots \dots \dots 80 < We < 600 \\ 0.75, & \dots \dots \dots We > 600 \end{cases} \quad (I.14)$$

Based on the model of Marengo and Tropea (1999), the mass of secondary droplets generated from single water drops impacting onto a moving liquid film can be written as

$$\frac{m_{sec}}{m_b} = (0.363 + 0.242\delta) \cdot 10^{-3} (K - K_{Cr})^{(2.928 - 1.521\delta)} \quad (I.15)$$

Correlations obtained by Roisman et al. (1999) indicate that the secondary-to-incident mass flux and number flux ratios correlate with the average impact Weber number ($20 < We < 300$) in the form of

$$\frac{\dot{m}_a}{\dot{m}_b} = 0.302 \left[1 - \frac{1}{1 + \exp(0.0274 \overline{We} - 4.442)} \right] \quad (I.16)$$

$$\frac{\dot{N}_a}{\dot{N}_b} = \frac{2767}{\overline{We}^{6.7}} \exp \left[0.938 (\ln \overline{We})^2 \right] \quad (I.17)$$

Another empirical model obtained by Tropea and Roisman (2000) indicates that the number flux ratio η_N , the axial momentum flux ratio η_p , and the kinetic energy flux ratio η_e can be expressed by

$$\eta_N = 2.69 \eta_m^{1.4} \quad (I.18)$$

$$\eta_p = 0.29 \eta_m^{1.19} \quad (I.19)$$

$$\eta_e = 0.36 \eta_m^{1.11} \quad (I.20)$$

Also the model of Stanton and Rutland (1996) shows that the ratio of total splashed-to-impact mass generated from impact of train of drops onto a liquid film can be written as

$$\frac{m_{sp}}{m_b} = -27.2 + 3.15 \varpi - 0.116 \varpi^2 + 1.4 \cdot 10^{-3} \varpi^3 \quad (I.21)$$

$$\text{where } \varpi = U_b \cdot \left(\frac{\rho}{\sigma} \right)^{\frac{1}{4}} \cdot v^{\frac{-1}{8}} \cdot f^{-\frac{3}{8}} \quad (I.22)$$

In the expression (I.22), f represents the dimensionless impact frequency defined as: $f = u_b / d_b$ and ν is the kinematic viscosity. Obtained curve-fit, i.e., Eq. (I.21) from experimental data is shown in Fig. I-2.

According to this model splash occurs for $\varpi > 18$.

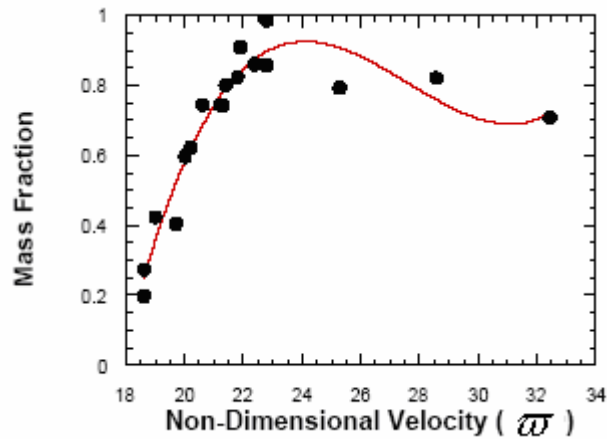


Fig. I-2: Mass fraction of secondary droplets versus non-dimensional impact velocity (Stanton and Rutland 1996).

Also based on the model of Mundo et al. (1994), the deposited mass fraction (m_{dep}/m_b) generated due to single droplets impacting onto a rigid wall (rotating disk in this experiments) is

$$\frac{m_{dep}}{m_b} = 1 - \frac{N_a}{N_b} \cdot \left(\frac{d_a}{d_b} \right)^3 \quad (I.23)$$

Schmehl et al. (1999) found the following correlation for deposition rate of spray impact onto thin liquid film from the experimental data performed by Samenfink (1997).

$$1 - \eta_{film} = (1 - \eta_{dry-wall}) \cdot e^{-h^*} \quad (I.24)$$

where $h^* = h/d_b$; h is thickness of the thin liquid film.

Experiments from Schmehl et al. (1999) show that thicker films lead to a larger deposition rate by damping the splashing process, see Fig. I-3. In this figure “ s ” represents the splashing parameter defined by

$$s = \frac{Re}{24La^{0.419}} \quad (I.25)$$

In Fig. I-4, the $Re-La$ plane is illustrated for droplets impacting onto a cold-dry wall indicating that a droplet with larger Laplace number ($La = \rho \sigma d_i / \mu^2$) needs larger Re number to splash.

Also based on the experimental data for typical thin films in combustor flows, Schmehl et al. (1999) found that there is no significant influence of the film thickness under $150\mu\text{m}$ on the splashing/deposition threshold.

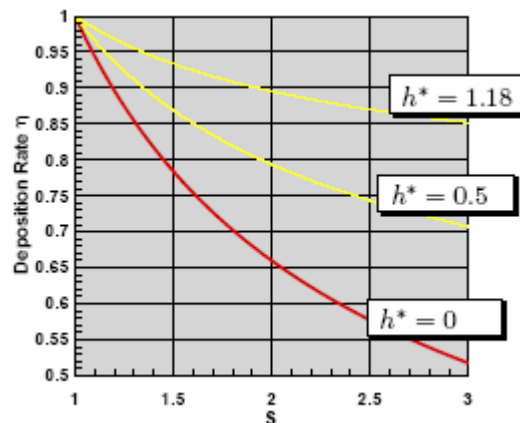


Fig. I-3: Deposition rate of spray impact onto thin liquid film (Schmehl et al. 1999).

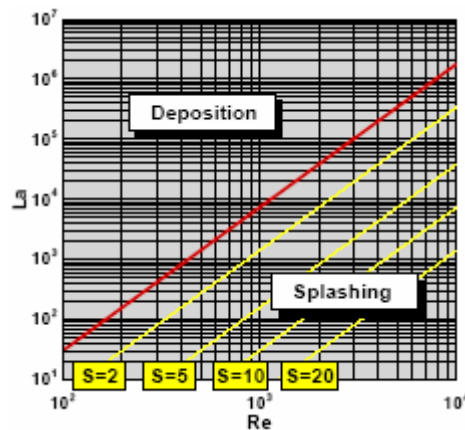


Fig. I-4: Deposition/Splashing border for single droplet impacting onto a cold-dry wall (Schmehl et al. 1999).

Based on work done by Bai and Gosman (1995) the quantity of secondary droplets per splash can be written as

$$N_a = 5 \cdot \left(\frac{We}{We_{Cr}} - 1 \right) \quad (I.26)$$

where We_{Cr} is the critical Weber number for the onset of splash assumed to be $We_{Cr}=80$.

Mundo et al. (1995) found another empirical expression for the number of secondary droplets per splash (N_a) based on spray impact onto a dry wall.

$$N_a = \min(1.676 \cdot 10^{-5} \cdot K^{2.539}, 1000) \cdot N_b \quad (I.27)$$

where $K = Oh \cdot Re^{1.25}$. In their experiments splash occurs if $K_{Cr} > 57.7$.

Wang and Watkins (1993) used a constant value $N_a=64$ for $We>80$.

Number of secondary droplets due to a single water droplet impacting onto a moving liquid film was driven by Marengo and Tropea (1999) as

$$N_a = \max \left(0, 1 + 0.363 \cdot 2^\beta \cdot \left(1 + 10^{-3} \cdot \frac{K - K_{Cr}}{1 - e^{K - K_{Cr}}} \right) \right) \cdot K \cdot 10^{-3} \cdot N_b \quad (I.28)$$

where β defines by

$$\beta = (0.242 + 2.928 \cdot \delta) \cdot (K - K_{Cr}) \quad (I.29)$$

Bibliography

1. Ahmadi-Befrui B, Uchil N, Gosman AD, Issa RI (1996) Modelling and simulation of thin liquid films formed by spray wall interaction. SAE Paper 960627.
2. Albrecht HE, Damaschke N, Borys M, Tropea C (2003) Laser Doppler and Phase Doppler Measurement Techniques. Springer-Verlag, Heidelberg.
3. Araneo L, Tropea C (2000) Improving phase Doppler measurements in a Diesel spray. SAE Paper 2000-01-2047.
4. Ashgriz N, Givi P (1987) Binary collision dynamics of fuel droplets. Int J Heat and Fluid Flow **8**: 205-210.
5. Ashgriz N, Poo JY (1990) Coalescence and separation in binary collisions of liquid drops. J Fluid Mech **221**: 183-204.
6. Bachalo WD (1994) Experimental methods in multiphase flows. Int J Multiphase Flow **20**: 26195.
7. Bachalo WD, Rudoff RC, Brena de la Rosa A (1988) Mass flux measurements of a high number density spray system using the Phase Doppler particle analyzer. AIAA 26th Aerospace Science Meeting.
8. Bai C, Gosman AD (1995) Development of methodology for spray impingement simulation, Society Automot Eng 950283: 69-87.
9. Bai C, Gosman AD (1996) Mathematical modelling of wall films formed by impinging sprays. SAE Paper 960626.
10. Bai C, Rusche H, Gosman AD (2002) Modeling of gasoline spray impingement. Atomiz & Sprays **12**: 1-27.
11. Bulzan DL, Levy Y, Aggarwal SK, Chitre S (1992) Measurements and predictions of a liquid spray from an air-assist nozzle. Atomiz & Sprays **2**: 44562.
12. Bush JMW, Hasha AE (2004) On the collision of laminar jets: fluid chains and fishbones. J Fluid Mech **511**: 285.

13. Bussmann M, Chandra S, Mostaghimi J (2000) Modelling the splash of a droplet impacting a solid surface. *Phys Fluids* **12**: 3121-3132.
14. Chandra S, Avedisian, CT (1990) The collision of a droplet with a solid surface. *Phys Fluids* **A2**: P1525.
15. Chandra S, Avedisian CT (1992) Observations of droplet impingement on a ceramic porous surface. *Int J Heat and Mass Transfer* **35**: 2377-2388.
16. Ching B, Golay MW, Johnson TJ (1984) Droplet Impacts upon Liquid Surfaces. *Science* **226**: 535-537.
17. Coghe A, Brunello G, Cossali GE, Marengo M (1999) Single drop splash on thin film: Measurements of crown characteristics. ILASS-Europe 99, Toulouse, July. 5-7th.
18. Cossali GE, Brunello G, Coghe A, Marengo M (1999) Impact of a single drop on a liquid film: experimental analysis and comparison with empirical models. Italian Congress of Thermofluid Dynamics UIT, Ferrara, 30 June-2 July.
19. Cossali GE, Coghe A, Marengo M (1997) The impact of a single drop on a wetted surface. *Exp Fluids* **22**: 463-472.
20. Cossali GE, Marengo M, Coghe A, Zhdanov S (2004) The role of time in single drop splash on thin film. *Exp Fluids* **36**: 888-900.
21. Cossali GE, Marengo M, Santini M (2005) Single-drop empirical models for spray impact on solid walls: A review. *Atomiz & Sprays* **15**: 699-736.
22. Cossali GE, Marengo M, Santini M, Watanabe J (2002) Secondary droplet atomization from single drop impact on heated surfaces. ILASS-Europe 2002, Sep.9-11, Zaragoza.
23. Culick FEC (1960) Comments on a ruptured soap film. *J Appl Phys* **31**: 1128.
24. Damaschke N, Kalantari D, Roisman IV, Tropea C (2005) Characterization of spray transport and spray/wall interactions using the IPI technique. 20th ILASS Conference, 5-7Sep, Orleans, France.
25. Damaschke N, Kalantari D, Roisman IV, Tropea C (2005) Characterization of spatial drop distribution in a spray using the IPI technique. 8th Int Conference,

- Optical Methods of Flow Investigation, 28 June-1 July 2005, Moscow, 8-11.
26. Dantec Dynamics Co (2002) Phase Doppler particle analyzer. User operations Manual.
 27. Dodge LG, Schwalb JA (1989) Fuel spray evolution: comparison of experiment and CFD simulation of non-evaporating spray. *J Eng Gas Turbines Power* **111**: 15-23.
 28. Durst F (1982) Combined measurements of particle velocities, size distributions and concentration. *ASME J Fluids Eng* **104**: 28496.
 29. Durst F, Melling A, Whitelaw JH (1981) Principles and Practice of laser-Doppler Anemometry. Academic Press, London (2nd edition).
 30. Esmaeeli A, Tryggvason G (2005) A direct numerical simulation study of the buoyant rise of bubbles at $O(100)$ Reynolds number. *Phys Fluids* **17**: 1-19.
 31. Fandrey C, Naqwi A, Shakal J, Zhang H (2000) A phase Doppler system for high concentration sprays. 10th Int Symp on Applications of Laser Techniques to Fluid Mechanics. Lisbon, Portugal.
 32. Farmer WM (1972) Measurement of particle size, number density and velocity using a laser interferometer. *J Appl Optics* **11**: 260312.
 33. Fedorchenko AI, Wang AB (2004a) On some common feature of drop impact on liquid surfaces. *Phys Fluids* **16**: 1349-1365.
 34. Fedorchenko AI, Wang AB (2004b) The formation and dynamics of a blob on free and wall sheets induced by a drop impact on surfaces. *Phys Fluids* **16**: 3911-3920.
 35. Glasheen JW, McMahon TA (1996) Vertical water entry of disks at low Froude numbers. *Phys Fluids* **8**: 8.
 36. Grover RO, Assanis DN (2002) A critical analysis of splash criteria for SIDI spray impingement. 15th ILASS Ann Conference on Liquid Atomiz & Spray Systems.
 37. Hardalupas Y, Taylor A (1994) Phase validation criteria of size measurements for the phase Doppler technique. *Exp Fluids* **17**: 2538.

38. Josserand C, Lemoyne L, Troeger R, Zaleski S (2005) Droplet impact on a dry surface: triggering the splash with a small obstacle. *J Fluid Mech* **524**: 47-56.
39. Kalantari D (2002) Design, construction and development of a fixed cone sleeve valve. M.Sc thesis, Tarbiat Modaress University, Tehran, Iran.
40. Kalantari D, Roisman, I.V., and Tropea, C., 2006. Spray impact onto deep liquid layers: deformation of air-liquid film interface, secondary spray and air bubble entrainment. ICLASS06, Aug.27-Sep.01, Kyoto, Japan.
41. Kalantari D, Tropea C (2005) Experimental study of spray impact onto rigid walls. 20th ILASS-Europe, Orleans, Sept. 5-7th.
42. Kalantari D, Tropea C (2006a) Considerations in Phase Doppler measurements of spray-wall interaction. 13th Int Symp Applications of Laser techniques to Fluid Mechanics. Jun. 26-29, Lisbon, Portugal.
43. Kalantari D, Tropea C (2006b) Comparison splash of a droplet in isolation and in a spray. Workshop-spray06, Mai. 29-30, Lampoldshausen, Germany.
44. Kalantari D, Tropea C (2006c) Oblique spray impingement onto rigid walls: Description of secondary spray. 14th Int. Mech. Eng. Conference, May.16-18, Isfahan, Iran.
45. Kalantari D, Tropea C (2006d) Spray impact onto flat and rigid walls: Empirical characterization and modelling. *I J Multiphase Flow* "in press".
46. Kalantari D, Tropea C (2006e) Spray impact onto rigid walls: Formation of the liquid film. ICLASS06, Aug.27-Sep.01, Kyoto, Japan.
47. Ko K, Arai M (2002) Diesel spray impinging on a flat wall, part I: Characteristics of adhered fuel film in an impingement diesel spray. *Atomiz & Sprays* **12**: 737-751.
48. Kuo T, Wallis GB (1988) Flow of bubbles through nozzles. *I J Multiphase Flow* **14**: 547.
49. Lazaro BJ (1991) Evaluation of Phase Doppler particle sizing in the measurement of optically thick, high number density sprays. UTRC91-11 United Technologies Research Center, East Hartford, CT.

50. Le Coz JF, Catalano C, Baritaud T (1994) Application of laser induced florescence for measuring the thickness of liquid films on transparent wall. 7th Int Symp on Applications of laser Techniques to Fluid Mechanics, Lisbon, Portugal.
51. Lee MM, Hanratty TJ (1988) The inhibition of droplet deposition by the presence of a liquid wall film. *I J Multiphase Flow* **14**:129-140.
52. Lee SH, Ko GH, Ryou HS, Hong KB (2001) Development and application of a new spray impingement model considering film formation in a Diesel engine. *KSME International Journal* **15**: 951-961.
53. Leifer I, Patro RK, Bowyer P (1999) A study on the temperature dependency of the rise velocity of bubbles. *J Atmospheric and Oceanic Technology* **17**: 1392-1402.
54. Levin Z, Hobbs PV (1971) Splashing of water drops on solid and wetted surfaces: hydrodynamics and charge separation. *Phil Trans R Soc, London* **269**: 555-585.
55. Macklin WC, Metaxas GJ (1976) Splashing of drops on liquid layers. *J Appl Phys* **47**: 3963-3970.
56. Mahalingam R, Limaye RS, Brink JA (1976) Velocity measurements in two-phase bubble-flow regime with Laser-Doppler anemometry. *AIChE Journal* **22**: 1152-1155.
57. Manzello SL, Yang JC (2002) An experimental study of a water droplets impinging on a liquid surface. *Exp Fluids* **32**: 580-589.
58. Mao CP (1996) Measurements of sprays using phase Doppler instruments: a study to establish formal operating. *Procedures 9th Ann Conference on Liquid Atomization and Spray Systems (San Francisco, CA)*, 226.
59. Marengo M, Tropea C (1999) Aufprall von Tropfen auf Flüssigkeitsfilme. Intermediate report for Project Tr. 194/10, Deutsche Forshungsgemeinschaft, FG-SLA, TU-Darmstadt.
60. Mehdi-Nejad V, Mostaghimi J, Chandra S (2003) Air bubble entrapment under an impacting droplet. *Phys Fluids* **15**: 173-183.

61. Moctezuma MF, Lima-Ochoterena R, Zeint R (2005) Velocity fluctuations resulting from the interaction of a bubble with a vertical wall. *Phys Fluids* **17**: 098106.
62. Mundo C, Tropea C, Sommerfeld M (1997) Numerical and experimental investigation of spray characteristics in the vicinity of a rigid wall. Elsevier 228-237.
63. Mundo C, Sommerfeld M, Tropea C (1995) Droplet-wall collisions: experimental studies of the deformation and breakup processes. *Int J Multiphase Flow* **21**: 151-173.
64. Mundo C, Sommerfeld M, Tropea C (1998) On the modeling of liquid sprays impinging on surfaces. *Atomiz & Sprays* **8**:625-652.
65. Naber JD, Reitz RD (1988) Modelling engine spray/wall impingement. SAE Paper 880107.
66. O'Connor JP, You SM, Haji-Sheikh A (1995) Laser Doppler anemometry measurements of bubble rise velocity and departure frequency. *Exp Heat Transfer* **8**: 145-160.
67. Ogüz HN, Prosperetti A (1990) Bubble entrainment by the impact of drops on liquid surfaces. *I J Fluid Mech* **219**: 143-179.
68. Oliemans RVA (2005) Gas-Liquid Transport in Ducts, in "Multiphase Flow Handbook", ed. Crowe, Taylor Francis, Boca Raton, London, New York, p. 2-6.
69. Panão MRO, Moreira ALN (2005) Flow characteristics of spray impingement in PFI injection systems. *Exp. Fluids* **39**: 364-374.
70. Pasandideh-Fard M, Bhole S, Chandra S, Mostaghimi J (1998) Deposition of tin droplets on a steel plate: simulations and experiments. *Int J Heat and Mass Transfer* **41**: 2929-2945.
71. Pasandideh-Fard M, Bussmann M, Chandra S, Mostaghimi J (2002) Simulating droplet impact on a substrate of arbitrary shape. *Atomiz & Sprays* **11**: 397-414.
72. Pasandideh-Fard M, Chandra S, Mostaghimi J (2002) A three-dimensional

model of droplet impact and solidification. *Int J Heat and Mass Transfer* **45**: 2229-2242.

73. Pasandideh-Fard M, Mostaghimi J (1996) On the spreading and solidification of molten particles in a plasma spray process: effect of thermal contact resistance. *Plasma Chemistry and Plasma Processing* **16**: 83-98.

74. Pasandideh-Fard M, Qiao M, Chandra YM, Mostaghimi M (1996) Capillary effects during droplet impact on a solid surface. *Phys Fluids* **8**: 650-659.

75. Pitcher G, Wigley G, Saffman M (1990) Velocity and Drop Size measurement in Fuel Sprays in a Direct Injection Diesel Engine. *Particle & Particle Systems Characterization* **7**: 160-168.

76. Pumphery HC, Elmore PA (1990) The entrainment of bubbles by drop impacts. *J Fluid Mech* **220**: 539-567.

77. Qiu HH, Hsu CT (1999) Method of phase Doppler anemometry free from the measurement volume effect. *Appl Optics* **38**: 2737-42.

78. Qiu HH, Hsu CT (2004) The impact of high order refraction on optical microbubble sizing in multiphase flows. *Exp Fluids* **36**: 100-107.

79. Qiu HH, Sommerfeld M (1992) A reliable method for determining the measurement volume size and particle mass fluxes using phase Doppler anemometry. *Exp Fluids* **13**: 393-404.

80. Range K, Feuillebois F (1998) Influence of surface roughness on liquid drop impact. *J Colloid and Interface Science* **203**: 16-30.

81. Rioboo R, Bauthier C, Conti J, Voue M, De Coninck J (2003) Experimental investigation of splash and crown formation during single drop impact on wetted surfaces. *Exp Fluids* **35**: 648-652.

82. Rioboo R, Marengo M, Cossali GE, Tropea C (2000) Comparison of drop impact: dry and wetted cases. *proceeding of ILASS-Europe 2000, Darmstadt*.

83. Rioboo R, Marengo M, Tropea C (2001) Outcomes from a drop impact on solid surface. *Atomiz & Sprays* **11**: 155-164.

84. Roisman IV, Araneo L, Marengo M, Tropea C (1999) Evaluation of drop

impingement models: experimental and numerical analysis of a spray impact. Proc 15th Ann Conference on Liquid Atomiz & Spray Systems, ILASS-Europe, Toulouse.

85. Roisman IV, Horvat K, Tropea C (2006) Spray impact: rim transverse instability initiating fingering and splash, and description of a secondary spray. *Phys Fluids* **18**: 102104.

86. Roisman IV, Prunet-Foch B, Tropea C, Vignes-Adler M (2002) Multiple drop impact onto a dry solid substrate. *J Colloid Interface Science* 256: 396-410.

87. Roisman IV, Tropea C (2001) Flux measurements in sprays using phase Doppler techniques. *Atomiz & Sprays* **11**:673-705.

88. Roisman IV, Tropea C (2004) Structure of an impinging spray. 4th Int Symp Meas Techn for Multiphase Flows, Sept.10-12, Hangzhoo, China.

89. Roisman IV, Tropea C (2005) Fluctuating flow and jetting in a liquid layer created by an impacting spray. *I J Multiphase Flow* **31**:179-200.

90. Sankar SV, Bachalo WD (1991) Response characteristics of the phase Doppler particle analyser for sizing spherical particles larger than the wavelength. *Appl Optics* **30**: 148796.

91. Scardovelli R, Zaleski S (1999) Direct numerical simulations of free surface and interfacial flow. *Ann Rev Fluid Mech* **31**: 567.

92. Schaub SA, Alexander DR, Barton JP (1994) Theoretical analysis of the effects of particle trajectory and structural resonances on the performance of a phase Doppler particle analyzer. *Appl Optics* **33**: 47383.

93. Schmehl R, Roskamp H, Willman M, Wittig S (1999) CFD Analysis of spray propagation and evaporation including wall film formation and spray/film. *I J Heat and Fluid Flow* **20**: 520-529.

94. Senda J, Kobayashi M, Iwashita S, Fujimoto H (1994) Modelling of gasoline spray impingement on a flat wall. *SAE Paper* **941894**: 1-14.

95. Sikalo S, Tropea C, Ganic EN (2005) Impact of droplets onto inclined surfaces. *J Colloid and Interface Science* **286**: 661-669.

96. Sivakumar S, Tropea C (2002) Splashing impact of a spray onto a liquid film. *Phys Fluids Lett* **14**: L85-88.
97. Snedecor GW, Cochran WG (1989) *Statistical methods* (8th ed.). The Iowa State University press, USA.
98. Sommerfeld M, Qiu HH (1995) Particle concentration measurements by phase Doppler anemometry in complex dispersed two-phase flows. *Exp Fluids* **18**:187-198.
99. Sommerfeld M, Qiu HH (1998) Experimental studies of spray evaporation in turbulent flow. *Int J Heat Fluid Flow* **19**: 1022.
100. Stanton DV, Rutland CJ (1998) Multi-dimensional modeling of thin liquid films and spray-wall interactions resulting from impinging sprays. *Int J Heat Mass Trans* **41**: 3037-3054.
101. Stanton DW, Rutland C (1996) Modeling fuel film formation and wall interaction in Diesel Engines. SAE paper 960628.
102. Strakey PA, Talley DG, Bachalo WD (1998) Phase Doppler measurements in dense sprays. ILASS-Americas (Sacramento, CA), 2915.
103. Strakey PA, Talley DG, Sankar SV, Bachalo WD (2000) Phase Doppler interferometry with probe to droplet size ratios less than unity II: Application of the technique. *Appl Optics* **39**: 388793.
104. Strakey PA, Talley DG, Sankar SV, Bachalo WD (1998) The use of small probe volumes with phase Doppler interferometry. ILASS-Americas (Sacramento, CA), 28690.
105. Tinaut FV, Melgar A, Castro A, Sa´nchez ML, Gime´nez M (1997) A method to determine liquid concentration in non-stationary axisymmetric sprays. *Exp Fluids* **23**: 299-305.
106. Tropea C, Marengo M (1998) The impact of drops on walls and films. ICMF 98, Lyon, France.
107. Tropea C, Marengo M (1999) The Impact of Drops on Walls and Films. *Multiphase Science & Technology* **11**: 1.

108. Tropea C, Roisman IV (2000) Modeling of spray impact on solid surfaces. *Atomiz & Sprays* **10**: 387.
109. Valizadeh M, Moghaddam M (1995) *Experimental design* (2th ed.). Parvin Inc. press, Iran, ISBN: 964-90515-1-1.
110. Van Den Moortel T, Santini R, Tadriss L, Pantaloni J (1997) Experimental study of the particle flow in a circulating fluidized bed using a phase Doppler particle analyser: a new post-processing data algorithm. *Int J Multiphase Flow* **23**: 1189-1209.
111. Wang AB, Chen CC, Hwang WC (2002) On some new aspects of splashing impact of drop-liquid surface interactions. in: *Drop-surface interactions*, edited by Rein M. Springer Alert Pub.-Co.
112. Wang M, Watkins AP (1993) Numerical modelling of Diesel spray impaction phenomena. *Int J Heat Fluid Flow* **14**: 301-311.
113. Webb C, Jones J (2003) Particle sizing in *Handbook of Laser Technology and Applications Vol III*, D 2.8. Taylor & Francis.
114. Widmann JF, Presser C, Leigh SD (2001) Improving Phase Doppler volume flux measurements in low data rate applications. *Meas Sci & Tech* **12**: 1180-1190
115. Xu TH, Tropea C (1994) Improving the performance of two-component Phase Doppler anemometers. *Meas Sci & Tech* **5**:969-975.
116. Yarin AL (2006) Spreading of liquids on solid surfaces: Static and dynamic contact lines. *Ann Review Fluid Mech* **38**: 159-192.
117. Yarin AL, Weiss DA (1995) Impact of drops on solid surfaces: self-similar capillary waves, and splashing as a new type of kinematics discontinuity. *J Fluid Mech* **238**: 141-173.
118. Zhu JY, Rudoff RC, Bachalo WD (1993) Number density and mass flux measurements using the Phase Doppler particle analyser in reacting and non-reacting swirling flows. *AIAA 31st Aerospace Science Meeting* 93: 0361.

Lebenslauf

1-Personalien:

Familienname: **Kalantari**

Vorname: **Davood**

Geburtsdatum und –Ort: **Juni 16, 1974, Ardebil, Iran**

Familienstand: **Verheiratet, Keine Kinder.**

2-Anschrift:

Anwesende Adresse (Deutschland): Schöneweibergasse 6, 64347 Griesheim, Germany,

Tel: +49 (0)61555-848698

Ehemalige Adresse (Iran): Pirbodaghi Alley. No.21, Sianaki Ave, Doolatabad, Tehran,

Iran. Tel: +98-021-33762670

E-Mail: d.kalantari@sla.tu-darmstadt.de ; dkalantari2000@yahoo.com

3-Ausbildungen:

Magister (M.Sc): Mechanical Eng. Tarbiat Modares University (Tehran-Iran). In: June 2001.(G.P.A = 16.54 out of 20.00)

4-Sonstige Ausbildungen:

- 1- Hydraulic Systems of Road Construction Machines (4 Courses With Certificates).
- 2- Industrial Pumps (1 Course with Certificate).
- 3- Piping Design (1 Course with Autoplant and Autopipe software Education).

5-Industrielle Erfahrungen:

- Feb.1999 -2003: Technical Manager. Nahrab Gostar Co. (Manufacturer of Fittings and Pressure and Flow Control Valves for water supply. Tehran, Iran.
- March 1997 - Feb.1999: Technical Designer. Nahrab Gostar Co., Tehran, Iran.
- Feb.1998 -2003: Advisor for Design Center, SANCO Co. (Manufacturer of Fittings and Valves for water supply. Tehran, Iran.

6-Forschungen und Veröffentlichungen:

1-Journal Papers:

- 9- **D. Kalantari**, C. Tropea, (2005). Considerations for high resolution Laser Doppler measurements in very small circular tubes. *J. Meas. Sci. and Tech.* **16**: 2344-2350.
- 10- **D. Kalantari**, C. Tropea, (2007). Spray impact onto rigid walls: Empirical characterization and modelling. *I.J. Multiphase Flow*, in press.
- 11- **D. Kalantari**, C. Tropea, (2006). Phase Doppler measurements of spray/wall interaction. *Exp. Fluids*, accepted.
- 12- **D. Kalantari**, A. Fedorchenko, P.-F. Sung, A.-B. Wang, and C. Tropea, (2006). Dynamics of high viscous liquid droplet spreading on rigid-flat surfaces. *EuroPhys. Lett.*, submitted.
- 13- **D. Kalantari**, C. Tropea, (2006). Liquid droplet impact onto flat and rigid surfaces: Initial lamella ejecting velocity. *EuroPhys. Lett.*, submitted.

2-Conference Papers:

- 14- **D. Kalantari**, C. Tropea, (2005). Experimental study of spray impact onto rigid walls. 20th ILASS Conference. 5-7Sep.Orleans, France.
- 15- N. Damaschke, **D. Kalantari**, I.V. Roisman and C. Tropea, (2005). Characterization of spray transport and spray/wall interactions using the IPI technique. 20th ILASS Conference. 5-7 Sep. Orleans, France.
- 16- **D. Kalantari**, C. Tropea, (2005). Considerations for high resolution laser Doppler measurements in very small nozzles. 8th Int. Conf. Optical Methods of Flow Investigation. 28 June-1July 2005, Moscow, 88-91.
- 17- N. Damaschke, **D. Kalantari**, I.V. Roisman and C. Tropea, (2005). Characterization of spatial drop distribution in a spray using the IPI technique. 8th Int. Con. Optical Methods of Flow Investigation. 28 June-1July 2005, Moscow, 8-11.
- 18- **D. Kalantari**, C. Tropea, (2006). Spray impact onto rigid walls: Formation of the liquid film. ICLASS06, Aug.27-Sep.01, 2006, Kyoto, Japan.
- 19- **D. Kalantari**, I.V. Roisman and C. Tropea, (2006). Spray impact onto deep liquid layers: deformation of air-liquid film interface, secondary spray and air bubble entrainment. ICLASS06, Aug.27-Sep.01, 2006, Kyoto, Japan.
- 20- **D. Kalantari**, C. Tropea, (2006). Oblique spray impingement onto rigid walls: Description of secondary spray. 14th Int. Mech. Eng. Conference, May.16-18, Isfahan, Iran.

- 21- **D. Kalantari**, C. Tropea, (2006). Considerations in Phase-Doppler measurements of spray-wall interaction. 13th Int. Symp. Applications of Laser techniques to Fluid Mechanics. Jun. 26-29, Lisbon, Portugal.
- 22- **D. Kalantari**, C. Tropea, (2006). Comparison splash of a droplet in isolation and in a spray. Workshop spray2006, Mai. 29-30, Lampoldshausen, Germany.
- 23- **D. Kalantari**, B. Ghobadian, T. Tavakolli, (2002). Design and Development of a fixed cone sleeve valve (6th International Mechanical Engineering Conference. Tehran, Iran. 2359-2367.

7-Industrielle Forschungen:

- 1- Design and Development of Diaphragm-type Automatic Control Valves (Globe type, DN100-500, PN10, 16). Cast and Ductile Iron and Fabricated.
- 2- Design and Development of Automatic Air Valves, Cast iron and Ductile iron (DN ½" to 8", PN 10, 16 and 25).
- 3- Design and Development of High pressure Gate Valves (DN100, 150, PN25), Ductile Iron.